Fabrication of nanostructures on tips
a proposed design for SNOM/TERS probes

Dissertation
der Mathematisch-Naturwissenschaftlichen Fakultät
der Eberhard Karls Universität Tübingen
zur Erlangung des Grades eines
Doktors der Naturwissenschaften
(Dr. rer. nat.)

vorgelegt von
Omar Tanirah
aus Gizeh, Ägypten

Tübingen
2020

Gedruckt mit Genehmigung der Mathematisch-Naturwissenschaftlichen Fakultät der Eberhard Karls Universität Tübingen.

Tag der mündlichen Qualifikation:	26.11.2020
Stellvertretender Dekan:	Prof. Dr. József Fortágh
1. Berichterstatter:	Prof. Dr. Monika Fleischer
2. Berichterstatter:	Prof. Dr. Dieter P. Kern

Contents

Zusammenfassung **5**

Motivation **7**

1 Theory **9**
1.1 Metals optical properties . . . 10
1.2 Localized surface plasmon resonance . . . 13
1.3 Scanning near field optical microscopy . . . 16
1.4 Tip enhanced Raman spectroscopy . . . 17
1.5 Probes . . . 18
1.5.1 Aperture probes . . . 18
1.5.2 Apertureless probes . . . 19
1.6 Probe designs . . . 21
1.7 Nanocone . . . 22

2 Physics of the Fabrication Techniques **27**
2.1 Glass chemical etching . . . 27
2.1.1 Optical fiber tapering . . . 28
2.2 Thin film deposition . . . 30
2.2.1 Resistive thermal evaporation . . . 32
2.2.2 Electron beam assisted evaporation . . . 32
2.2.3 Deposition of Gold thin film . . . 32
2.3 Focused ion beam . . . 33
2.4 Focused electron beam induced deposition . . . 36
2.5 Ion beam milling . . . 38

3 Methods and setup **41**
3.1 Optical fiber chemical etching . . . 42
3.2 Plateau formation using FIB . . . 44

3.3 Thin film deposition 46
3.4 Structuring the hard mask for dry etching 48
3.4.1 Deposition of a Pt pillar as hardmask 48
3.4.2 Milling a cylindrical structure using FIB 49
3.5 Dry etching using Ar-ion milling machine 52

4 Fabrication of gold nanocones on cantilevers 55
4.1 Optimization of the fabrication process 56
4.1.1 Plateau optimization 56
4.1.2 FIB milling of a cylindrical hard mask 59
4.1.3 Platinum pillar deposition 62
4.2 Results and Discussion 65
4.2.1 Nanocone fabricated using Pt-Mask 66
4.2.2 Nanocone fabricated using a disc milled by FIB 74
4.3 Simulations of the nanocones scattering 78
4.4 Conclusion 79

5 Nanocone fabrication on top of optical fiber 83
5.1 Fabrication process 84
5.2 Results and Discussion 87
5.2.1 Nanocone on top of multimode optical fiber 88
5.2.2 Nanocone on top of single mode optical fiber 94
5.3 Simulation of the scattering of the nanocones 102
5.4 Conclusion 103

6 Summary 107

Appendix 108

A Appendix 109
A.1 Cantilever specifications 109
A.2 Process of FIB milling the AFM-C tip 110
A.3 Preparation of the fiber for the FIB milling 110
A.4 Sputter Yield Calculations 111

References 113

Acknowledgment 123

Zusammenfassung

Die optische Raster-Nahfeld-Mikroskopie (engl. Scanning nearfield optical microscopy (SNOM)) eröffnet neue grenzüberschreitende Möglichkeiten in der optischen Mikroskopie und Spektroskopie über die Auflösungsgrenze hinaus. Die Entwicklung von Geräten aus dem Bereich der Nanotechnologie mit neuartiger Funktionsweise, Verwendung von neuen Materialien zum Aufbau dieser multifunktionalen Geräte und die Notwendigkeit eines besseren Verständnisses chemischer Wechselwirkungen innerhalb komplexer biologischer Systeme wie DNA, Bakterien, Zellen erfordern neue Methoden und Werkzeuge um die physikalischen und chemischen Eigenschaften der Materialien auf dem molekularen Niveau zu begreifen. SNOM bildet sich als ein Pionierinstrument für optische Bildgebung in der sub-Wellenlängen-Dimension heraus [1, 2]. Bei der SNOM-Messung wird eine, mit einer scharfen Spitze ausgestattete, Prüfsonde während dem Rasterscanvorgang oberhalb der Oberfläche der Probe im Nahfeldbereich der Probe mit Licht angestrahlt. Daher ist die Messung grundsätzlich durch das Interaktionsvolumen des Nahfeldes der Sonde mit einer Größe des Spitzenradius und der Probenoberfläche begrenzt [3]. SNOM ist im Jahr 1984 als optisches Pendant zur Rastersondenmikroskopie entstanden. Die Idee wurde bereits im Jahr 1928 von E.H. Synge [4] hervorgebracht. Nach Jahrzehnten wurde diese als ein visionärer Weg zur Umgehung der klassischen Auflösungsgrenze der optischen Mikroskopie erkannt [5]. Im Gegensatz zu anderen Rastersondenmikroskopieverfahren ist es möglich die Komplementären informationen der SNOM ohne Vorbehandlung der Proben und auf eine zerstörungsfreie Weise zu erhalten. Des Weiteren können die SNOM-Messungen an einem breiten Spektrum von Proben und in ihrer natürlichen Umgebunge durchgeführt werden.

SNOM wurde erfolgreich durch Spektroskopiemessungen, wie Spitzen-verstärkte Fluoreszenz Spektroskopie und/oder Spitzen-verstärkte Raman Spektroskopie (Tip enhanced Raman Spectroscopy (TERS)) begleitet [6], da die sichtbaren optischen Wellenlängen die Energieäquivalenz im Bereich der elektronischen und der Schwingungsübergänge der Moleküle haben. Daher wurden simultane Messungen zur Charakterisierung der Morphologie und der chemischen Eigenschaften der Probe durchgeführt. Bei TERS-Messungen wird die Raman-Streuung der

Proben in nanoskaligen Dimensionen erfasst. Diese enthüllen wertvolle Informationen über chemische Wechselwirkungen und deshalb wird die Raman-Streuung als Fingerabdruck der Verbindungen und Elemente eines Werkstoffes, bis hin zu den einzelnen Molekülen, betrachtet [7–9].

Die SNOM-Sonde kann zusätzlich zur x- und y-Richtung das Nahfeld der Proben in z-Richtung scannen [10, 11]. Daher wurde die SNOM-Feldkartierung im 3D-Raum für verschiedene Proben wie Cu-Nanopartikeln [12] und Bornitrid-Nanoröhren [13] aufgenommen.

Die Auflösung der SNOM- und TERS-Instrumente wird durch die Sonden definiert. Folglich ist die Herstellung hochwertiger und reproduzierbarer Sonden der Kern der Entwicklung der SNOM und TERS. Es gibt vielfältige Sondentypen, deren plasmonische Nanostrukturen als Antenne dienen. Diese sind für die Aufnahme einer hohen Auflösung und einer Nahfeldverstärkung besonders prädestiniert.

Motiviert durch die Theorie und experimentelle Ergebnisse der Feldverstärkung und durch die hohe Auflösung der plasmonischen Nanokegelsonden, ist unser Ziel, die Herstellung von Nanokegelsonden auf nicht planaren Substraten im Hinblick auf hohe Reproduzierbarkeit und verbesserte Regulierung der Kegelgeometrie, zu modifizieren. Diese Arbeit befasst sich mit den Herstellungsmethoden von hochwertigen SNOM/TERS-Sonden, die einen hohen Durchsatz und eine hohe Reproduzierbarkeit ermöglichen. Wir haben die Arten von Substraten durch die Anwendung von Herstellungstechniken der Nanokegel auf verschiedenen Klassen sich verjüngende Glasfasern erweitert. Damit können die Nanokegelsonden flexibel in verschiedenen SNOM/TERS-Setups implementiert werden.

Diese Arbeit gliedert sich in fünf Kapitel, die die Theorie der Optik und die Physik der Fertigungstechniken, die Herstellungsmethode und die experimentellen Ergebnisse präsentieren. Kapitel 1 bietet einen Überblick über die Elektrodynamik der Plasmonik, die SNOM/TERS-Prinzipien und den Stand der Technik von Sonden, und schließlich die optischen Eigenschaften, Herstellung und Anwendung des plasmonischen Nanokegels. Kapitel 2 stellt die Theorie der Herstellungsverfahren vor, die zur Entwicklung des Nanokegels eingesetzt werden. Kapitel 3 zeigt die Schritte der Herstellungsmethode des Nanokegels auf Cantilever und Glasfaser. Kapitel 4 pr äsentiert die Optimierungs- und Versuchsergebnisse der aus einem einzigen Gold-Nanokegel gefertigten Sonden auf einem AFM-Cantilever. Kapitel 5 stellt die Herstellung von Gold-Nanokegel auf Glasfaserspitzen und Optimierung der Sondenqualität vor.

Motivation

Scanning near-field optical microscopy (SNOM) opens new frontiers in optical microscopy and spectroscopy measurements beyond the diffraction limit. The evolution of the nanotechnology field of devices with new functionality, integration of new materials to form multifunctional devices, and the understanding of chemical interactions within complex biological systems such as DNA, bacteria, cells demand new tools to understand the physics and chemistry of the materials on the molecular level. SNOM arises as a pioneer tool for optical imaging in the sub-wavelength dimension [1, 2]. In the SNOM measurement, a probe with a sharp tip is illuminated with light all through its raster scan over the sample surface in the locale of the sample nearfield. Hence, the measurement in principle is limited by the volume of interaction of the nearfield with a size on the order of the probe tip radius and the sample surface [3]. SNOM emerged in 1984 as an optical counterpart of scanning probe microscopy. The idea had been introduced by E.H. Synge in 1928 in [4]. After decades it had been recognized as a visionary way to circumvent the optical microscopy classical diffraction limit [5]. SNOM complementary information to other scanning probe microscopy methods can be gained without pre-treatment of the samples and in a non-destructive way. Further, SNOM measurements can be performed for a broad range of samples and in native environments.

SNOM has been successfully accompanied with spectroscopy measurements, such as tip-enhanced fluorescence spectroscopy and/or tip-enhanced Raman spectroscopy (TERS) [6], since the visible optical wavelengths have energies that fall in the energy range of the electronic and vibrational transitions in molecules. Hence, simultaneous measurements were performed to characterize the samples' morphology and chemical properties. TERS measurements record the Raman scattering of the samples in nanoscale dimensions. They reveal valuable information about chemical interactions, since Raman scattering is considered as the fingerprint of the compounds and elements inside the material down to single molecules [7–9].

A recent development in the SNOM setups has been reported, in which the SNOM probe can scan the near field of the samples in the z-direction in addition

to the x and y direction [10, 11]. Hence, SNOM field mapping in the 3D space has been recorded for different samples such as Cu nanoparticles [12] and Boron nitride nanotubes [13].

The resolution of the SNOM and TERS instruments is defined by the probes. Consequently, the fabrication of high quality and reproducible probes is at the core of developing the SNOM and TERS. There are a variety of probes types, where the plasmonic nanostructures serving as an antenna are the most successful ones in recording a high resolution and field enhancement.

Outline

Motivated by the theory and experimental results on the field enhancement and the high resolution of the nanocone probe, we aim to modify the fabrication of nanocones on non-planar substrates to have a good reproducibility and control over the cone geometry. In this work, we propose the fabrication of high quality SNOM/TERS probes, where the fabrication method has a good throughput and reproducibility. This work is divided into five chapters presenting the theory of optics and the physics of the fabrication techniques, then the fabrication method and the experimental results. Chapter 1 is a survey on the electrodynamics of plasmonics, then the SNOM/TERS principles and the state of art of the probes, finally the plasmonic nanocone optical properties, fabrication and application. Chapter 2 presents the theory of the fabrication techniques employed to engineer the nanocone. Chapter 3 shows the steps of the fabrication method of the nanocone on cantilever and optical fiber. Chapter 4 presents the optimization and experimental results of the fabricated probes made of a single gold nanocone on an AFM-cantilever. Chapter 5 presents the fabrication of gold nanocones on optical fibers and optimization of the probe's quality.

Chapter 1

Theory

In this chapter we review the electromagnetic theory of surface plasmon polaritons, and localized surface plasmon resonances. Then, the principles of SNOM measurements, setups and probes. Finally, we review the nanocone plasmonic properties and applications.

The optical properties of material can be described by the classical electrodynamic theory. Maxwell's equations eq. 1.1-1.4 elaborate macroscopically the electromagnetic field and its interaction with charged particles. [14, 15]

$$\nabla \cdot \mathbf{D} = \rho \tag{1.1}$$

$$\nabla \cdot \mathbf{B} = 0 \tag{1.2}$$

$$\nabla \times \mathbf{E} = -\frac{\partial \mathbf{B}}{\partial t} \tag{1.3}$$

$$\nabla \times \mathbf{H} = \mathbf{J} + \frac{\partial \mathbf{D}}{\partial t} \tag{1.4}$$

where $\mathbf{D}$ is the electric displacement, $\mathbf{E}$ is the electric field, $\mathbf{B}$ is the magnetic induction, $\mathbf{H}$ is the magnetic field, ρ is the charge density and $\mathbf{J}$ is the current density.

The $\mathbf{D}$ and $\mathbf{H}$ are connected with the electromagnetic properties of the medium, which are represented by the polarization ($\mathbf{P}$) and magnetization ($\mathbf{M}$) as follows;

$$\mathbf{D}(\mathbf{r}, t) = \varepsilon_0 \, \mathbf{E}(\mathbf{r}, t) + \mathbf{P}(\mathbf{r}, t), \tag{1.5}$$

$$\mathbf{H}(\mathbf{r}, t) = \mu_0^{-1} \mathbf{B}(\mathbf{r}, t) - \mathbf{M}(\mathbf{r}, t), \tag{1.6}$$

$$\tag{1.7}$$

The **P** and **D** of free electrons in metals under a harmonic time dependent external electric field can be written as [15];

$$\mathbf{P} = -\frac{ne^2}{m\ (\omega^2 + i\ \gamma\omega)}\ \mathbf{E} \tag{1.8}$$

$$\mathbf{D} = \varepsilon_0 (1\ -\ \frac{\omega_p^2}{m\ \omega^2 + i\ \gamma\omega})\ \mathbf{E} \tag{1.9}$$

where the n is the electron number density, e is the electron charge, m is the free electron mass, ω is the angular frequency of **E**, γ is the characteristic collision frequency, ω_p is the plasma frequency of the free electron gas.

The evanescent wave plays a main role in nearfield optics. It is originally generated at total internal reflection in which the transmission part is converted into evanescent waves. The electric field at plane z=z$_0$ composed of the propagating and evanescent waves fulfilling the Sommerfeld's radiation condition in the half space [16] can be written as in eq. 1.10 from [17];

$$E(x,\ y,\ z_0) = \int_{-\infty}^{+\infty}\int_{-\infty}^{+\infty} A(k_x,\ k_y)\ exp\ \left(i\ (k_x x + k_y y + z_0\sqrt{k_0^2 - (k_x^2 + k_y^2)})\right)\ dk_x\ dk_y \tag{1.10}$$

propagating $k_0^2 > (k_x^2 + k_y^2)$ (1.11) evanescent $k_0^2 < (k_x^2 + k_y^2)$ (1.12)

where $A(k_x,\ k_y)$ is a complex amplitude of the field, k_0 is the vacuum wave vector. The field in eq. 1.10 is composed of the propagating as in eq. 1.11 and evanescent waves in eq. 1.12. The evanescent waves propagate in x and y as surface plane waves but decay exponentially very fast in the z-direction. Their importance arises from their nature as high spatial frequency waves which retain very fine topographic details of the samples, and their high localization near the surface [16].

1.1 Metals optical properties

Metals interactions with light retain a very interesting optical response, the so called plasmon. In optics, the plasmon is defined as the surface wave of the collective oscillation of electrons under an external electric field as in Fig. 1.1, and in solid state it is the quantum of the collective oscillation of surface-charge-density polaritons formed by the coupling of the em-field to a longitudinal charge density

wave in metal [18]. Plasmons can enhance the em-field and manipulate the light in nano dimensions, thus play a crucial role in nano-optics.

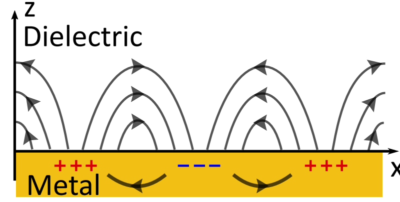

Figure 1.1: Surface charges in metal oscillate longitudinally at the dielectric/metal interface driven by an external electric field [19].

The charges' response in metals to an oscillating external electric field can be described by the dielectric constant, which is a complex function in frequency. The Drude model is an elementary approach to formulate the charge oscillations, by which the electrons are considered in a good approximation as free electrons within the material boundaries [20]. Hence, the drift motion of the electrons in metals under the influence of an external harmonic electromagnetic field from [21] can be described by eq. 1.13;

$$m_e \frac{\partial^2 \mathbf{r}}{\partial t^2} + m_e \gamma \frac{\partial \mathbf{r}}{\partial t} = e\mathbf{E}_0 e^{-i\omega t} \tag{1.13}$$

where the m_e is the effective electron mass of free electrons, e is the electron charge, γ is the electron collision frequency. E_0 and ω are the applied electric field amplitude and frequency, respectively.
Then, by solving the eq. 1.13 the dielectric complex function is found as in eq. 1.14:

$$\epsilon_{\text{Drude}} = \epsilon^{'}_{\text{Drude}} + i\epsilon^{''}_{\text{Drude}} \tag{1.14}$$

$n = \sqrt{\epsilon^{'}_{\text{Drude}}}$,

$$\epsilon^{'}_{\text{Drude}} = 1 - \frac{\omega_{\text{p}}^2}{\omega^2 + \gamma^2} \tag{1.15}$$

$$\epsilon^{''}_{\text{Drude}} = \frac{\gamma \omega_{\text{p}}^2}{\omega(\omega^2 + \gamma^2)} \tag{1.16}$$

$n \approx \kappa = \sqrt{\epsilon^{''}_{\text{Drude}}/2}$, at $\omega \ll \gamma$ (1.18) where $\epsilon^{'}_{\text{Drude}}$ is the real part, $\epsilon^{''}_{\text{Drude}}$ is the imaginary part, $\omega_{\text{p}} = (ne^2/\epsilon_0 m_e)^{1/2}$, and it is the resonance of the collective oscillations of the electrons in volume and called the Drude plasma frequency (plasma

frequency) [20, 22].

The dielectric constant real part (eq. 1.15) is connected with polarization of the charges in metal and the refractive index, while its imaginary part (eq. 1.16) is connected with the dissipation energy of the electromagnetic wave in metal and thus the absorption. The polarization of the ion cores can be represented as in eq. 1.19 by adding a fitting parameter ϵ_∞ in eq. 1.15 [15, 21]. By applying this correction, we plot the Drude dielectric constant for gold as in Fig. 1.2a, b.

$$\epsilon'_{\mathrm{Drude}} = \epsilon_\infty - \frac{\omega_{\mathrm{p}}^2}{\omega^2 + \gamma^2} \tag{1.19}$$

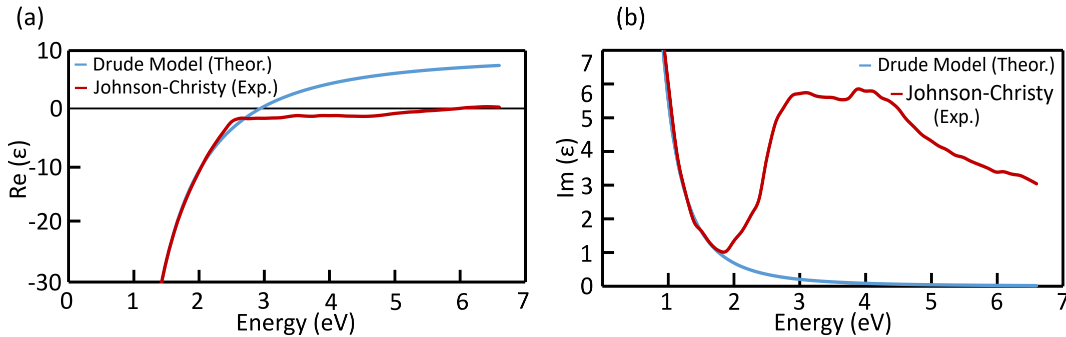

Figure 1.2: The plot of the gold dielectric constant; (a) Real part (b) Imaginary part. The calculated values use the Drude model, and the experimental values are from Johnson-Christy. The values used in the Drude curve; $\hbar\gamma$ and $\hbar\omega_{\mathrm{p}}$ are equal to 0.069 eV, and 8.95 eV, respectively, determined by Johnson and Christy in [23], where ϵ_∞ is 9.27.

The Drude model shows a good agreement with the experimental results in the infrared energy range, while it failed in the visible, since the interband transitions become more crucial. Thus, the interband transitions should be presented in the dielectric function of metal to match the Johnson and Christy experimental measurements [24], which can be achieved by describing the bound electrons as Lorentzian oscillators. Thus, a Lorentz-like parameter should be implemented in eq. 1.15 and eq. 1.16 [25]. Further, the effective mass considered will be the one for bound electrons, and γ will represent the damping constant mainly due to the radiative decay [22].

The condition to couple light with SPPs is obtained from the dispersion relation, which can be derived by solving the wave equation for a harmonic electric field at the interface between two media [14]. The dispersion relation is described

in good approximation by eq. 1.20;

$$k_x^{'} = \sqrt{\frac{\epsilon_1^{'}\epsilon_2}{\epsilon_1^{'} + \epsilon_2}}\frac{\omega}{c} \qquad (1.20) \qquad k_x^{''} = \sqrt{\frac{\epsilon_1^{'}\epsilon_2}{\epsilon_1^{'} + \epsilon_2}}\frac{\epsilon_1^{''}\epsilon_2}{2\epsilon_1^{'}(\epsilon_1^{'} + \epsilon_2)}\frac{\omega}{c} \qquad (1.21)$$

where the parallel wave number real part is $k_x^{'}$ and imaginary part is $k_x^{''}$, and c is the speed of light. The $k_x^{'}$ defines the SPP wavelength, while the $k_x^{''}$ shows the damping of the SPP.

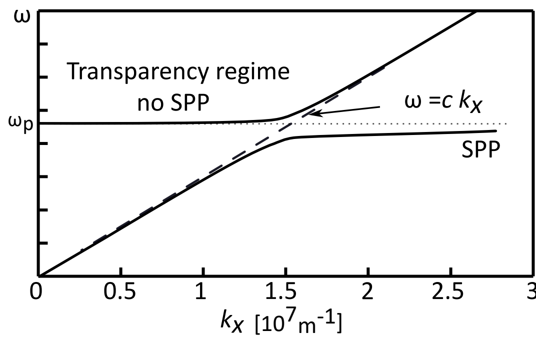

Figure 1.3: Dispersion relation of SPP (eq. 1.20) at gold/air interface, where the gold dielectric constant is calculated from eq. 1.15. The dashed line is the light line.

In Fig. 1.3, the lower energy branch ($\omega < \omega_\mathrm{p}$) of the dispersion relation presents the SPPs, which is the relevant frequency range for plasmonics. In $\omega > \omega_\mathrm{p}$, the light is forbidden to propagate inside metal [14]. Thus, the light must fulfill the momentum conservation in order to couple with surface charges, and this can be achieved by increasing the wave vector of light. One of the primary methods to excite the SPP is by the evanescent waves created by Otto and/or Kretschmann configurations [22]. A detailed discussion about surface plasmon properties can be found in [15, 20, 22].

1.2 Localized surface plasmon resonance

A localized surface plasmon resonance (LSPR) is the collective oscillation of the conduction electrons as in Fig. 1.4, which are physically confined in the metal nanoparticle (MNP) volume. In contrast to the SPP, the light coupling with LSPR does not require an additional alignment to fulfill the momentum conservation, and the coupling is granted by the MNP dimension and geometry. The

LSPR frequency depends on the MNP dimension, geometry, and on the dielectric properties of its material and the surrounding environment. Thus, the LSPR is a unique and attractive optical property of MNPs for a broadband of applications, since it can be tuned over a wide range of frequencies by choosing the materials, and nanoengineering of its structure.

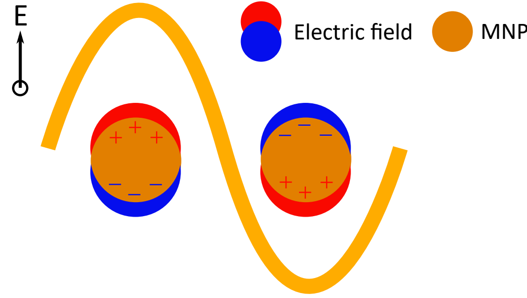

Figure 1.4: The localized electrons in a MNP oscillate with the plasmonic frequency driven by the incident light electric field.

Since the MNP diameter is much smaller than the incident wavelength, the electric field of the incident wavelength is roughly constant over the MNP. Thus, it is adequate to study the LSPR modes under the quasistatic approximation. In this case by using $\mathbf{E}$ = - $\nabla\Phi$ in Maxwell's wave equation, we obtain a Laplace equation as in eq. 1.22 and it is solved by considering the potential (ϕ) as Legendre polynomial, in order to calculate the electric field in and outside the particle [15].

$$\nabla^2\phi = 0 \tag{1.22}$$

$$\mathbf{E}_{\text{in}} = \frac{3\epsilon_m}{\epsilon + 2\epsilon_m}\mathbf{E}_0 \tag{1.23}$$

$$\mathbf{E}_{\text{out}} = \mathbf{E}_0 + \frac{3\mathbf{n}(\mathbf{n}\cdot\mathbf{p}) - \mathbf{p}}{4\pi\epsilon_0\epsilon_m}\frac{1}{r^3} \tag{1.24}$$

$$\mathbf{p} = \epsilon_0\epsilon_m\alpha\mathbf{E}_0 \tag{1.25}$$

$$\alpha = 4\pi a^3\frac{\epsilon\ -\ \epsilon_m}{\epsilon\ +\ 2\epsilon_m} \tag{1.26}$$

where $\mathbf{p}$ is the dipole moment, α is the polarizability of a sphere, $\mathbf{n}$ is the unit vector in the direction of detection, ϵ_0, ϵ_m and ϵ are the dielectric constant of vacuum, the surrounding and the particle, respectively. From the α in eq. 1.26 the dependency of the resonance on the sphere radius a and the dielectric constant of the particle and the surrounding environment arises. Further, the E_{out} in eq. 1.24 is the superposition between the incident electric field and the induced dipole field of the particle, which shows the enhancement of the field due to the

particle.

In case of large particles, the fields are calculated using Mie theory, and the solution shows different mechanisms of radiative and nonradiative retardation of the incident field in the particle [20].

Optical Nanoantenna

The MNPs can be considered as nanoantenna for the optical frequency, since at the LSPR frequency the effective cross section of the MNP increases, and thus they can effectively capture and manipulate light [25]. Due to the oscillating charges at the NP surface, the electromagnetic energy is strongly localized in a subwavelength vicinity. Hence, MNPs are pioneering in converting the evanescent waves into the far field, and reveal the high spatial frequency information of the sample surface. The optical antennas depend strongly on the incident light polarization and the detection orientation, and they are characterized quantitatively by their radiated power, efficiency, and gain (amplification) in the angular spectrum. Finally, the antenna aperture (A) as in [27] by eq. 1.27 defines the efficiency to capture the incident light by the sample, and it is equivalent to the enhanced absorption cross section (σ_A) due to the presence of the antenna [26,27].

$$A(\theta, \phi, \mathbf{n}_{\text{pol}}) = \mathrm{P}_{exc}/I = \sigma_A(\theta, \phi, \mathbf{n}_{\text{pol}}) \tag{1.27}$$

where P_{exc} is the absorbed power, and I is the incident radiation in the direction (θ,ϕ), with the polarization $\mathbf{n}_{\text{pol}}$ [27].

The absorption cross section (σ) as in eq. 1.28 can be calculated as the ratio between the cross section of the sample in the presence and absence of the antenna.

$$\sigma = \sigma_0 \frac{|\mathbf{n}_{\text{pol}} \cdot \mathbf{E}|^2}{|\mathbf{n}_{\text{pol}} \cdot \mathbf{E}_0|^2} \tag{1.28}$$

where σ_0 is the cross section in the absence of the antenna, $\mathbf{E}$ and $\mathbf{E}_0$ is the electric field in the presence and absence of the antenna, respectively.
The design of the MNP can be performed by considering it a Fabry Perot cavity, thus its length must match half an integer of the effective wavelength [28]. In case of employing field enhancement in a gap such as in a Bow Tie structure, where the impedance matching is important, MNP can be modeled as an optical circuit where the metal part acts as a coil and the insulator (dielectric) part acts as a capacitor [29, 30].
Different numerical methods are employed to calculate the optical properties of nanoparticles by solving Maxwell's equations based on finite-difference time-

domain [31], finite element method [32] and boundary element method [33] schemes.

1.3 Scanning near field optical microscopy

SNOM is an optical counterpart of the scanning probe microscopy instruments. It is based on scanning a subwavelength dimension illuminating source in a form of an aperture or a nanoparticle (NP) over the sample surface, and within the vicinity of the sample nearfield.

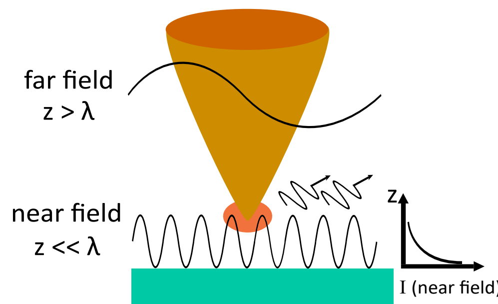

Figure 1.5: SNOM performed by scanning a nano illuminating source to detect the evanescent field at the sample surface [34].

The SNOM signals are collected by the integration over the volume of interaction between the SNOM probe tip and the sample. Hence, SNOM resolution is defined by the probe tip radius. This is in contrast with the classical optical microscopy, which is limited by the diffraction limit and thus its resolution is $\approx \lambda/2$. Further classical microscopy relies only on the freely propagating em-wave, since it is not possible to confine electromagnetic energy in the sub-wavelength dimension.

Challenges in SNOM measurements stem from the complexity of the nearfield variations in phase and magnitude over the subwavelength scale. Additionally, the complexity arises from the image and data analysis due to the interaction and the coupling of tip-sample. This applies especially to the signal enhancement in the apertureless scattering SNOM (s-SNOM) where the plasmonic resonance of the probe depends on the illumination conditions and surrounding environment. SNOM imaging is discussed in detail in [35].

1.4 Tip enhanced Raman spectroscopy

Tip enhanced Raman spectroscopy (TERS) is a nano-spectroscopy technique to detect Raman signal with a nanometer resolution. It is performed mainly by the s-SNOM plasmonic probes to enhance the Raman signal of the samples. Raman scattering is an inelastic scattering of the incident photon by the vibrational transitions of the molecules. The energy of the scattered photon compared to the incident photon as in Fig. 1.6 can be lower, so-called Stokes, or higher, so-called anti-Stokes scattering.

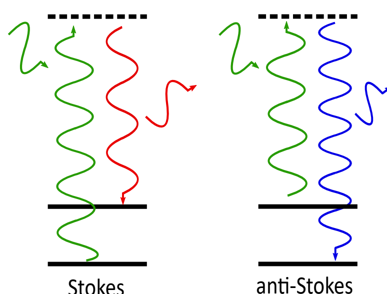

Figure 1.6: In Raman scattering, the incident photon is scattered by the vibrational transitions of molecules, where the Raman scattering signal can have a lower energy than the incident photon, so-called Stokes scattering, or a higher energy, so-called anti-Stokes scattering.

Raman signal is considered as the molecules' fingerprint, thus it attracts a great interest to define the chemical constituents of the biomolecule, and to monitor cell activities [36]. Further, it is a vital tool to characterize the quality of carbon nanotubes and semiconductor crystals [26, 37]. The main drawback of Raman scattering signals is that they are hard to detect, due to their small cross section. There are different setups to overcome the weak signal of Raman, and to perform high spatial resolution Raman as reviewed in [38, 39]. We focus here on the TERS method since it could be performed with the fabricated probes in this work. In TERS, there are different mechanisms to enhance the Raman signal, and mainly they are geometrical enhancement (lightning rod effect) where the electrons are strongly confined at the tip apex of conical probes, LSPR enhancement where a nano-antenna (section 1.2) is employed as a probe and its field at the LSP resonance enhances both the incident light on the sample and the emitted one from the sample. This mechanism plays the main role in surface and tip enhanced Raman spectroscopy. Thus, it is important to synthesise or fabricate the MNP in a way to match its LSPR with the wavelength range of

the measurement. Further, the enhancement factor in TERS depends strongly on the substrate material, where the gold substrate shows a higher enhancement compared to the dielectric substrate, and this is due to the contribution of the gap mode. Another mechanism is the chemical enhancement but its yield is much smaller than that of the previously mentioned ones.

1.5 Probes

SNOM probes can be categorized into two main categories [40], aperture [41, 42] and apertureless probes [43]. In this section, we summarize the principles of both categories, and focus on the different designs of the apertureless probes.

1.5.1 Aperture probes

The first SNOM technique was by illuminating the samples through an aperture with a subwavelength dimension, so-called aperture SNOM (a-SNOM). The a-SNOM probe types are tapered optical fibers and tetrahedral tips [44, 45].

The most common are tapered optical fiber probes, and they can be obtained either by chemically etching the fiber in hydrofluoric acid as it will be described in section 2.1 or by heating the fiber and pulling. The tapered fiber has a sub-50 nm tip radius, then it will be coated with high refractive index material thin films such as metals. Finally, the transparent aperture can be formed either by depositing the thin films at an oblique angle and keeping the fiber rotating during the deposition, or by milling a hole at the fiber forefront apex using a focused ion beam. The metal thin films act as a reflector to confine the light inside the tapered region of the fiber, while the uncoated forefront of the tip apex is the SNOM probe aperture.

The aperture diameter can not get smaller than the skin depth of the coating, since the field spatial distribution will be much larger than the physical dimension of the aperture. Further, the power of the signal will be tremendously reduced following the fourth [46] or sixth power of the aperture diameter [47], hence decrease the signal noise ratio. Accordingly, the best spatial resolution that can be achieved by a-SNOM is in the order of $\approx$ 50 nm [48]. The incident light number of modes are decreased for the light propagating towards the aperture of the tapered fiber, since the modes cut off wavelength is inversely proportional to the diameter of the fiber. The power distribution in the aperture probe for the HE_{11} mode can be modeled using the mode matching analysis. The HE_{11} mode of the light power distribution in the a-SNOM probe can be written as in eq.

1.29, HE_{11} is chosen since its last mode will decay inside the tapered region. [49]

$$P(z) = P(z_0)e^{-2\int_{z_0}^{z} \alpha_{11}(z)dz} \tag{1.29}$$

where the P(z) is the power distribution as function of z, α_{11} is the HE_{11} mode attenuation, and its function of the core diameter and the opening angle, $z_0 < z < 0$ is a coordinate point chosen along the light propagation, starts at z_0 direction inside the fiber towards the aperture at 0. The power throughput of the a-SNOM probe is proportional to the half opening angle (δ) of the tapered fiber, consequently there is a trade off between the throughput and the resolution of the aperture probes. [14] The a-SNOM can be performed in different configurations as in Fig. 1.7 to illuminate the sample and/or to detect the sample signals through the aperture.

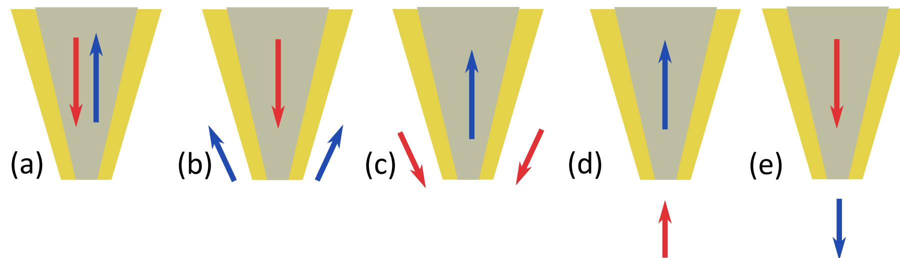

Figure 1.7: a-SNOM can be performed in different illumination and detection configurations; Reflection of the substrate; (a) Illumination and detection through the aperture, (b) Illumination through the aperture and detection from the side, (c) Side illumination and detection through aperture. Transmission through substrate; (d) Detection through the aperture, (e) Illumination through the aperture [34].

We summarized here the basic concepts of how the presence of a subwavelength aperture in the vicinity, i.e. the nearfield, of the sample allows high resolution imaging and detecting an evanescent field. The transmission through an aperture is modeled numerically in [50].

1.5.2 Apertureless probes

An alternative SNOM technique has been performed by raster scanning of a nanoparticle over the sample surface, with so-called apertureless probes. The

apertureless probes can provide higher resolution measurements. Fig. 1.8 shows different setup alignments of s-SNOM.

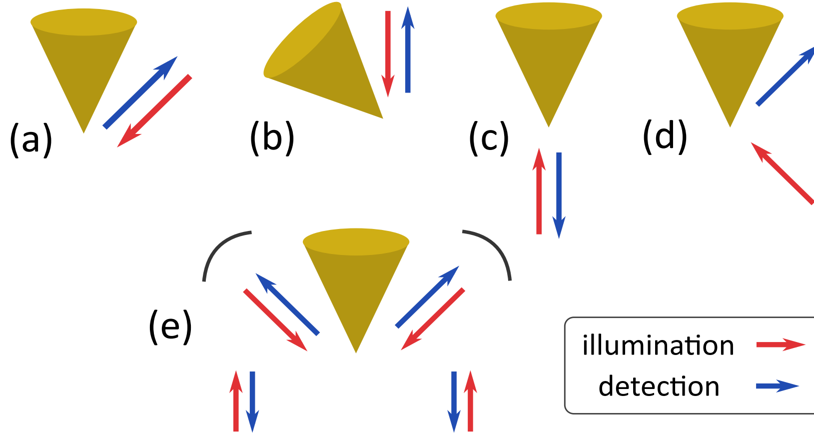

Figure 1.8: SNOM can be performed in different illumination and detection configurations [34]; (a) Side on. (b) Top down. (c) and (d) Inverted in two different alignments for illumination and detection. (e) Parabolic mirrors are used to focus the illumination laser and collect the detection signals.

Apertureless scattering SNOM (s-SNOM), in contrast with a-SNOM offers higher spatial resolution and better signal to noise ratio. The most common approaches to obtain apertureless probes are by coating a sharp dielectric tip with a metal thin film, by electrochemical etching of a metal wire, or by attaching a nano-particle at the tip of a tapered probe. In s-SNOM, the scattering of the incident field is related to the effective polarizability (α_{eff}) of the tip sample system $\mathrm{E}_s \propto \alpha_{eff}\ \mathrm{E}_i$, where the α_{eff} according to [51] is expressed as in eq. 1.30

$$\alpha_{eff} = \frac{\alpha(1+\beta)}{1-(\alpha\beta/(16\pi(\mathrm{a}+z)^3))} \tag{1.30}$$

α is the tip polarizability, β is the image dipole polarizability, a is the tip apex radius, and z is the distance between the tip apex and the sample. The α is a function of the tip dielectric constant and apex radius, where the β is a function of the substrate dielectric constant [51].

1.6 Probe designs

The s-SNOM probes have been fabricated in several sophisticated designs to achieve high resolution and signal enhancement. In the following, we present the milestones ones;

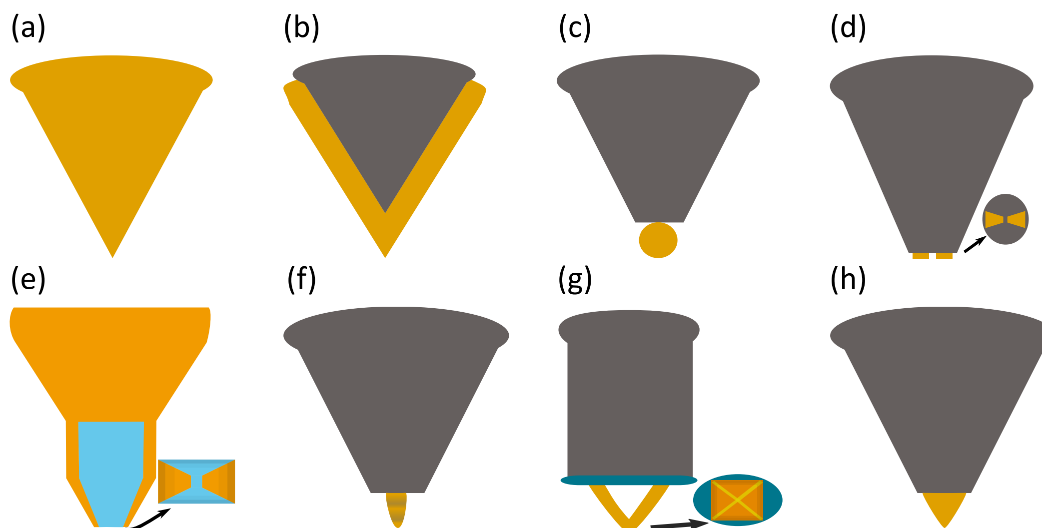

Figure 1.9: SNOM/TERS apertureless probes [40]; (a) Electrochemically etched metal tips. (b) Sharp dielectric tip coated with metal thin film. (c) Nanoparticle attached to sharp dielectric tip. Nano-gap Probe (d) Bow tie shape, (e) Probe has shape of the Campanile [54]. (f) A nano tip deposited by FEBID on a tapered optical fiber. (g) A hollow gold pyramid attached on a wire [55]. (h) A gold nanocone fabricated on an AFM cantilever.

Metal Tips: They are fabricated by electrochemically etching a gold wire in HCl content solution. Their enhancement stems mainly from the lightning rod effect [14, 52].

Metal Coated Dielectric Tips: An AFM cantilever coated with a metal film, which is deposited by thermal evaporation. The role of the film smoothness is crucial for field enhancement. Thus, the spikes of a rough film surface can be considered as nanoparticles and have a higher enhancement compared to a smooth film. This type shows much less or no absorption compared to the sharp metal tips. [38]

Nanoparticle on sharp tip: A metal nanoparticle (MNP) can be made either by attaching an MNP to a dielectric tip or by fabricating the MNP on the tip. In this case, the enhancement factor depends on the MNP absorption cross sec-

tion. Its maximum occurs at the particle LSP resonance [20]. At this frequency, the LSP will create a field higher than the incident field, which will enhance the exciting field on the samples and the emitted signal from the sample.
Nanogap probe: The probe has a nano-gap made of dielectric (insulator) between two metals, and it is formed by FIB milling a gap between two metal nanostructures such as a bow tie [53], or by elaborating nanoimprint lithography to fabricate a Campanile shape probe [54]. These probes were found to have a field enhancement independent from the type of the samples, and their fabrication process shows a good reproducibility. But, the strong field at the edges of the bow tie will be parallel to the sample surface which might make the coupling not efficient.
Tip on tip probe: The probes with a sharp pointing nanostructure are formed e.g. by depositing a pillar by focused electron beam induced deposition. A large scale method to fabricate probes has been accomplished by template stripping a hollow metal pyramid with a smooth morphology and sharp tip using a long wire from the grooves etched in a Si substrate [55]. Sculpturing a nanocone on AFM cantilever, a high purity and sharp tip radius with sub 10 nm has been achieved in [56].
The MNP with a small radius of curvature provides field enhancement due to the lightning rod effect, in addition to the one from the LSP, especially the MNP with geometrical shapes like tips and nanocones, where a strong localization of the surface charge density occurs in the vicinity of the tip apex [57]. Additionally, it was found, that spheroids show a higher enhancement than spheres, since the spheroids' scattering cross section is larger than the one of spheres [58, 59].

Rigorous textbooks on the influence of the particle shape, size and morphology on their cross section can be found in [20, 24]

1.7 Nanocone

The nanocone is a pioneer 3D nanostructure with unique geometric and optical properties, which make it a promising probe to perform measurements for the sample chemical composition and morphology with a high spatial resolution. It exhibits two main LSPR modes, the base mode (in plane) which is parallel to the cone base and the tip mode (out of plane) which is parallel to the main axis. The nanocone LSPR as shown in Fig. 1.10a can span the visible range by tuning its dimensions and aspect ratio [61]. The dominance between the nanocone modes can be switched by applying polarized lasers, selecting the excitation angle [61] or breaking the nanocone geometric symmetry during the fabrication [62]. The

nanocone tip mode is interesting for nanoscopy and nanospectroscopy [63]. It brings a highly confined field around the tip apex of sub 10 nm radius possessing an easy access pointing hotspot as in Fig. 1.10b. Hence, it permits a strong field enhancement and high spatial resolution measurements. Further, its field enhancement increases the measurements' signal to noise ratio.

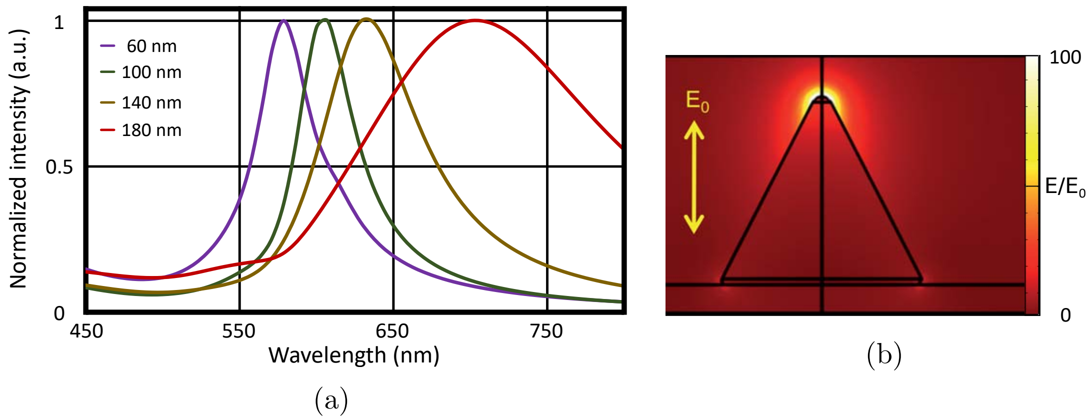

Figure 1.10: (a) The LSPR (tip mode) can be tuned over the visible wavelength by varying the nanocone dimensions from 60 nm to 180 nm by step 40 nm, while its aspect ratio is 1, calculated by 3D FDTD simulation [31]. (b) Distribution of the electric near field enhancement generated by exciting the tip mode of a gold nanocone on ITO excited by E_0 parallel to the cone's long axis after [61].

It has been fabricated in arrays as in Fig. 1.11 on top of opaque silicon substrates [64], and transparent silica substrates using e-beam lithography and Ar-milling [65]. In the e-beam lithography method, a substrate having a plasmonic material thin film on its top is coated with a photoresist such as PMMA. By applying the e-beam lithography the photoresist is patterned with circular holes. Then, on top of the resist is deposited a hard mask film made of an oxide such as Al_2O_3, afterwards a liftoff step is performed to remove the resist and the material on top of it, thus obtaining circular oxide discs standing on top of the plasmonic film. Finally, by applying Ar-milling, the protected area under the mask is shaped into a nanocone, and the unprotected area is etched away. By utilizing the e-beam lithography, nanocones arrays can be fabricated with well controlled dimensions of the nanocone, and a high reproducibility and throughput [66, 67].

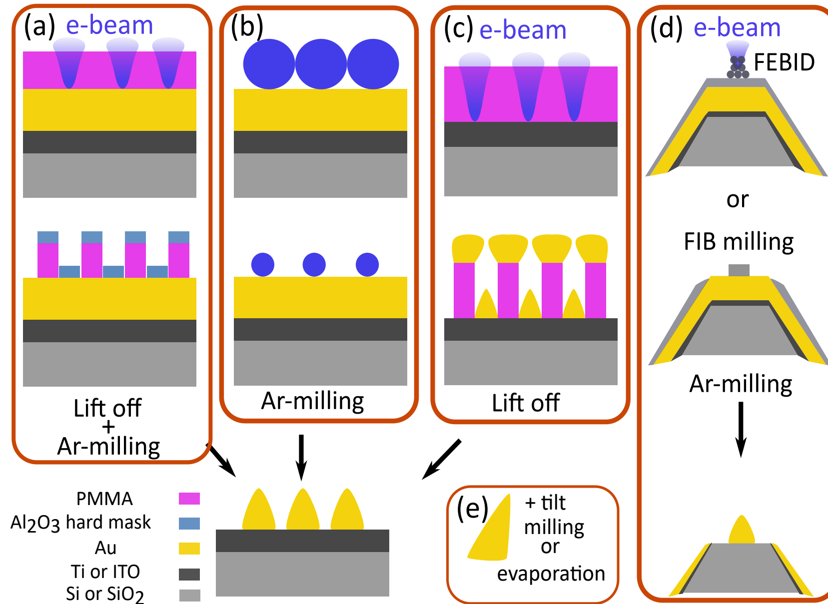

Figure 1.11: Various methods of the nanocone fabrication have been developed in AG Fleischer/Kern; (a) The e-beam lithography patterns the photoresist to have a hard mask disc, then a nanocone is formed after the Ar^+ milling [64, 65]. (b) To fabricate nanocones over a large area by using polystyrene spheres as etch mask. [68] (c) Alternative method to the dry etching, is to use a shadow mask [69]. (d) Nanocone as a SNOM probe fabricated on top of AFM cantilever by depositing the hard mask using the FEBID technique [63] or by shaping a disc mask using FIB [70]. (e) A tilted (asymmetric) nanocone produced by employing a tilted film evaporation or a tilted Ar^+ milling [62].

Nanocones have been fabricated successfully, as in Fig. 1.11 on different types of substrates by employing various methods of nanofabrication. The nanocone fabrication depends mainly on Ar^+ milling of a hard mask with disc shape, where simultaneously the mask protected area is shaped into a nanocone, and the unprotected area is etched away. The difference between these methods is the technique of patterning the mask. The nanosphere lithography wherein the hard mask for the Ar-milling is formed by using a monolayer of polystyrene spheres permits to fabricate over a wide area patterns of nanocones [68]. It has been fabricated as a single nanocone on top of a Bismuth column [64]. Further methods are the evaporation deposition through a hole mask [69], and nanoimprint [71]. One of the interesting applications for nanocones is to form a hybrid system by attaching quantum dots around its tip [72]. Nanocones appear as promising SNOM and

TERS probes, after successfully fabricating nanocones on top of AFM cantilevers using an induced-deposition lithography mask. Nanocones have been demonstrated as SNOM and TERS probes by performing high-resolution topographic measurements corresponding to their tip radius and near field enhancement for the Raman signal of carbon nanotubes via their localized surface plasmon resonance [63].

Chapter 2

Physics of the Fabrication Techniques

In this chapter, we introduce a survey on the physics and instruments of the exploited fabrication techniques in the nanocones fabrication on top of cantilevers and optical fibers to provide a tool to fabricate higher quality SNOM probes.

2.1 Glass chemical etching

We etched glass optical fibers to obtain a sharp tapered tip to be a substrate for the gold nanocone. Glass (SiO_2) can dissolve at room temperature only in Hydrofluoric acid (HF) or solutions containing HF acid. The etching mechanism as in [74] can be generally described by eq. 2.1

$$\mathrm{SiO_2 + 6HF \longrightarrow H_2SiF_6 + 2H_2O} \tag{2.1}$$

The glass etch rate depends on the composition of the etchant and the glass. The HF acid dissolves in water into four species H^+, F^-, HF_2^- and undissociated HF molecules [75]. The glass etching process is determined by the adsorption of HF, H^+, and HF_2^-, where H^+ ions have a catalytic role. The electron density of the bridging oxygen in the SiO_2 is increased by HF and HF_2^- adsorption. Hence, more H^+ ions will be adsorbed and break more siloxane bonds. The etching rate of glass in HF solutions mainly depends on the adsorption of HF and HF_2^-. The dissolution process based on the H^+, HF_2^-, and HF can be calculated as in [74] by eq. 2.2

$$V_\mathrm{E} = k_1 \cdot \Theta(\mathrm{H^+}) \cdot \left\{ k_2 \Theta(\mathrm{HF_2^-}) + k_3 \cdot \Theta(\mathrm{HF}) \right\} + k_4 \cdot \Theta(\mathrm{H^+}) \tag{2.2}$$

where V_E is the etch rate, k_i represent the reaction rate, the adsorption equilibrium constants, and the number of adsorption sites per unit surface area, Θ is the degree of coverage of active adsorption sites. Adding a strong acid controls the active molecules, thus the etch rate of the glass. For example by adding Nitric acid, Hydrochloric acid or Sulfuric acid this reduces the HF_2^- concentration but increases H^+ which has a catalytic effect in a way that it accelerates the glass dissolution process [76–78]. Another method is adding Ammonium fluoride (NH_4F) to HF which is known as buffered oxide etch or buffered HF (BHF) to control the concentration of HF_2^- and stabilize the etching rate of SiO_2 [79, 80] and consequently influence the morphology of the etched glass. By applying these etchant solutions and with the help of a suitable setup optical fibers can be tapered in a well controllable manner, as it will be described in chapter 5.

2.1.1 Optical fiber tapering

In principle, there are two main methods to produce a tapered fiber, which are chemical wet etching in the HF-solution and the mechanical heat and pull procedure. In the following, we review the tapering methods of fibers and focus on wet etching and the techniques used to improve the quality of wet etched fibers.

In the heat and pull method, as in Fig. 2.1 a stripped fiber is heated using different sources such as a CO_2 laser [81] or a flame [82]. The heat is focused at a small section of the fiber, which gets stretched by pulling its ends apart, thus, narrowing the heated section till it detached into two tapered fibers. These tapered fibers have a smooth surface, and their profile can be controlled by the heating power and the pulling speed [14].

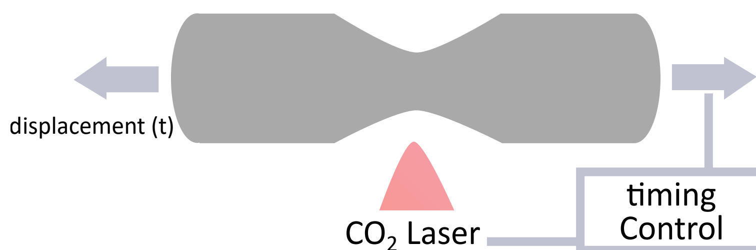

Figure 2.1: The heat pull setup consists of a CO_2 laser focused at a section, where the ends are pulled. Thus, it gets narrowed and detached into two tapered fibers [14].

Wet etching is the main method used in this work to produce sharp tapered fibers. It is performed by vertically immersing the optical fiber in an HF solution

to form a sharp tapered tip. The common technique for fiber wet etching was firstly introduced by Turner in [83], the so-called Turner method.

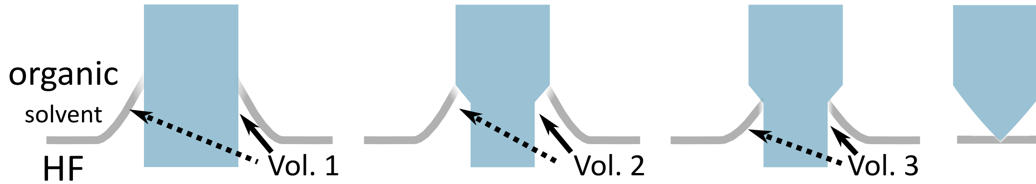

Figure 2.2: Wet etching of the optical fiber using the Turner technique. The etching beaker contains a HF acid liquid, which is covered by an immiscible organic solvent. The fiber is immersed vertically in the etching beaker. The meniscus is formed around the fiber wall due to the surface tension, and its height depends on the fiber radius. The dissolution of the fiber within the meniscus volume (Vol. 2) produces a heavier weight solution. The resulting is a lower meniscus in a more stable position as in Vol. 3.

It is performed by adding a layer of an organic solvent above the HF. The liquid forms a meniscus around the fiber wall as in Fig. 2.2 due to the interface energy difference between the free and wetted fiber surface. The meniscus vertical motion during the fiber etching forms the sharp conical tapered fiber. There are two main interpretations for the decrease of the meniscus height during etching. Firstly, the height increases with the fiber radius, and as the fiber radius diminishes in the bulk HF, the height will decrease and drops to a lower position. Secondly, the dissolution of the fiber in the meniscus volume increases the density of the solution, thus the weight of the meniscus volume becomes greater while the surface tension force remains unchanged. Then, the meniscus height will drop down to a lower position with reduced volume. This method is a self-terminated one since after completing the fiber etching the etchant will drop down, and the organic solvent layer will protect the sharp tip from the etchant. The organic solvent layer reduces the vaporization of HF which leads to a more stable etchant composition and forms a meniscus around the fiber wall due to its surface tension. The meniscus creates the etching volume to form a tapered fiber. Hence by modifying the meniscus, we can tune the tapered tip height, cone angle and smoothness.

In the application which demands a tapered optical fiber (T-OF) with a high optical transmission efficiency, the T-OF cone angle is a very important parameter. A larger cone angle corresponds to a high transmission efficiency. Different approaches were proposed to tune the cone angle of the T-OF, which can be distinguished in two categories. One category is etching the fiber without adding

an organic solvent layer and utilizing a fiber with a doped core. Accordingly, the differential etch rate of the core and cladding can be tuned by varying the etchant solution temperature and composition to tune the T-OF cone angle and height.

The second category is adding the organic solvent layer on the top of the etchant solution. Thus varying the organic solvent with different surface tension force produces different cone angle [84]. But, the relation between the surface tension force and cone angle is not clear. The more defined method is the dynamic wet etching of the optical fiber [85], where the fiber is moving vertically during the etching. The fiber movement direction defines the cone angle and height, thus drawing up the fiber produces a T-OF with a long cone and small cone angle, while moving down results in a T-OF with a short cone and wider opening angle. Further, the cone angle can be finely tuned by the speed of the fiber motion during etching.
We had elaborated most of the mentioned methods, and the more favorable one was the dynamic etching, by which we can tune the chemically tapered fibers geometry and enhance their smoothness to produce adequate high-quality SNOM probes.

2.2 Thin film deposition

We have used two evaporation techniques to deposit thin films on the samples, which are resistive thermal and electron beam assisted evaporation. In this section we introduce the theory and important experimental parameters of these two methods.
Thin film deposition is operated under high vacuum to have a uniform and homogenous thin film with high purity. Thermal coupling between the heater and source material in vacuum can be only via radiation. General definition of evaporation deposition is to deposit thin films by transfer of atoms or molecules from a heated source to be deposited on the substrate. It occurs by liberating the molecule at the material surface from the potential well created by the surroundings molecules. The evaporation rate of the evaporation process can be described generally from [86] as in eq. 2.3

$$\Phi_e = \frac{\alpha_e N_A (P_{\mathrm{e}} - P_{\mathrm{h}})}{(2\pi M \mathrm{R} T)^{\frac{1}{2}}} \tag{2.3}$$

Φ_e is the flux rate of atoms (or molecules) per area per time leaving the source, $\mathrm{P_e}$ is the equilibrium vapor pressure, $\mathrm{P_h}$ is the chamber pressure, α_e is the coefficient of evaporation (it varies between 0 to 1), N_A is the Avogadro number, M is the

atomic weight, R is the gas constant and T is the evaporant source temperature. It is important to have a homogenous thin film with the same thickness over the whole substrate. In vacuum, the thickness corresponds to the deposition rate, and the thin film quality is controlled by the geometry of the source, the substrate position and the orientation with respect to the beam of evaporated atoms from the source. This can be defined in good approximation as in [86] by eq. 2.4;

$$\frac{d\bar{M}_s}{dA_s} = \frac{\bar{M}_e \cos\phi \cos\theta}{\pi r^2} \tag{2.4}$$

where M_e is the total evaporated mass, M_s the mass that falls on the substrate area dA_s.

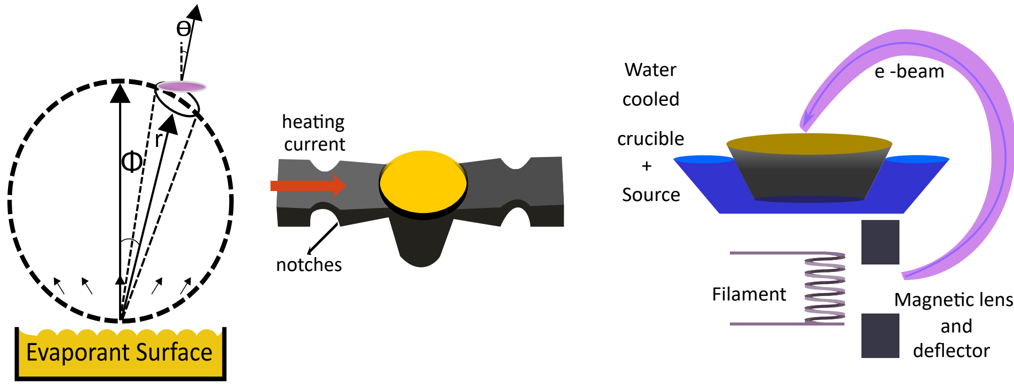

Figure 2.3: (a) Evaporation from source surface [86]. (b) Evaporation by heating current. (c) E-beam assisted evaporation.

The angular dependence of the deposition rate can be addressed as in Fig. 2.3a by two angles as in eq. 2.4, where ϕ is the evaporation angle, it is between the source normal and the vector of the source atoms (or molecules) beam, and θ is the receiving angle, it is between the substrate normal and the vector of the vapor beam in the direction to the substrate [86]. The θ plays an important role in the nanocone fabrication as it will be described in the following chapters, where the site to fabricate the nanocone on is aligned to have theta equal to 0° while we try to have theta approach 90 ° on the fiber walls.

2.2.1 Resistive thermal evaporation

In thermal evaporation, the evaporant is placed on the concave part of a boat shaped source as in Fig. 2.3. It is heated by passing a current through the boat and evaporant. The heating power is equal to I^2R, where R is the resistance of the boat. During the evaporation, the evaporant material can diffuse out of the concave part, which deforms the geometry of the evaporation surface. Therefore, notches at the boat side with a higher resistance are designed in a way that the evaporation rate at these notches is higher than the material spreading rate.

2.2.2 Electron beam assisted evaporation

The material is heated using a focused electron beam (e-beam) at a spot on the evaporation source surface. The e-beam is considered a nonthermal (non-Joule) method of evaporation. It applies to any material, and the main advantage is to evaporate reactive material such as silicon (Si) and chromium (Cr), or high melting point materials like Titanium (Ti).

The e-beam configuration as in Fig. 2.3c consists of an e-gun, a magnetic field lens, a material source, and a cooling system. The e-gun is placed in a location out of sight of the evaporant source to avoid any contamination. The e-beam is steered by the magnetic field to hit at the center of the evaporant. The e-beam should be steered over the source to keep the surface of the source uniform and to avoid forming a hole through the crucible which may lead to a short circuit.

2.2.3 Deposition of Gold thin film

The gold is the nanocone plasmonic material and it was deposited on substrates made of Si and SiO_2. But we consider that we deposit gold on SiO_x in both cases since the Si substrate will still have a native few nanometer layer of SiO_x on its top. The bonding between the substrate and the deposited material is more likely to occur when both have the same chemical bond type. In the case of Au-SiO_2, the chemical bonds are different. Au has a metallic bond, and SiO_2 has a covalent bond [87]. Hence, we used titanium (Ti) as an adhesion material. Depositing Ti on top of SiO_x breaks the bonds between silicon and oxygen, forming Ti-Si and Ti-O bonds. Consequently, Au can form a strong metallic bond with Ti [88–90]. Further, to deposit a gold thin film with high quality the vacuum pressure and the deposition rate must be considered. It was found that the vacuum pressure must be in the order of 10^{-6} Torr or better to avoid contribution of residual gas in the film morphology, while the deposition rate must be fast in order to increase

the grain size and reduce the pinning at grains boundaries [91].

2.3 Focused ion beam

Focused ion beam (FIB) is a pioneer micromachining instrument employed in direct writing of micro- and nanostructures, ion beam lithography and ion implantation [92]. We used the FIB to adapt the AFM cantilever and the tapered optical fiber to be a substrate for the nanocone, and to directly mill a disc shape to be a hard etching mask. A FIB consists of three main parts:

- A point source of gallium ions (Ga^{+}), specifically a liquid metal ion source (LMIS).
- A column of charged particle lenses that collimate and focus the generated beam and direct it on the sample surface.
- A blanker to prevent the beam from reaching the sample surface.

The source used in the FIB for Ga^{+} ions is the LMIS, which has a high brightness and supplies non-reactive ions.

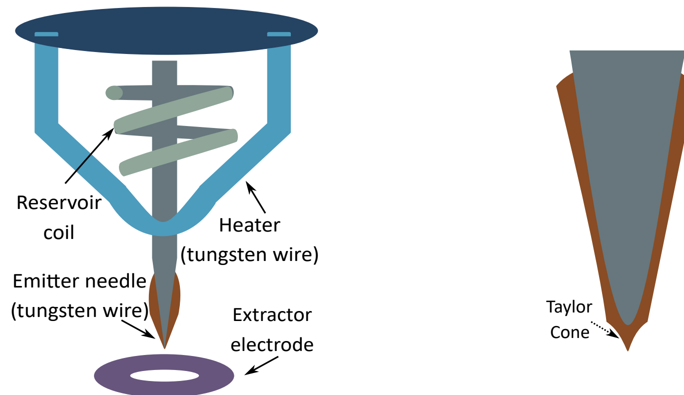

Figure 2.4: The LMIS has a reservoir surrounded by a heater loop to maintain the molten metal. A thin liquid metal film flows and forms a Taylor cone around the needle tip. The field evaporation emission current is generated by an electric field in the order of 10^{10} V/m.

As shown in Fig. 2.4 the LMIS consists of a semi-conical gallium reservoir surrounded by a heater loop, which supplies a thin liquid film flow over a sharp tungsten needle. The balance between the electrostatic force and the Ga liquid surface tension forms a Taylor cone at the needle tip. Applying a strong negative potential between the needle and the extraction electrode generates an electric

field in the order of 10^{10} V/m at the tip. Thus, the Taylor cone will be distorted and form a cusp. The ion emission occurs by field evaporation from the cusp. For instance at 2μA emission current the Taylor cone radius is about 5 nm [93].

In FIB the energetic ions are employed to locally modify the surfaces by deposition, milling (etching), chemically assisted etching and ion implantation. The distribution of deposited energy during the ion collisions with the sample surface is modeled by a collision cascade [94, 95], with a detailed review in [96]. The collisions between the focused ion beam and the sample surface are divided into two types: electronic with the electrons of the sample atoms while nuclear with the nuclei of the sample atoms. The electronic collisions lead to ionization, and emission of electrons and electromagnetic radiation from the sample. The nuclear collisions contribute the sputtering (milling) process by delivering energy and momentum required to generate lattice defects and to remove an atom from the sample.

In FIB milling two processes occur, sputtering and redeposition. The efficiency of the FIB milling is described by the sputter yield, which is defined as the number of the removed atoms per incident ion. The sputter yield depends on the incidence angle, ion energy, masses of ions and target atoms and target temperature.

Sputtering is the main process which defines the shape of the milled structures. In contrast the redeposition, where sputtered atoms are redeposited within the milling volume, is considered as a side effect process, and is more pronounced when the structure aspect ratio is higher than one [97]. It deforms the milled structure shape by creating inclined sidewalls and alters the local effective milling sputter yield.

The FIB milling of a structure is governed by the scan path, dwell time, overlap and number of loops. The scan path is the sequence of the milling points ordered to form a specific shape, and it can be in a raster, serpentine or vector mode. The FIB ion beam intensity distribution can be divided into a core which can be described by a Gaussian distribution as in eq. 2.5 and a long tail.

$$J(x,y) = \frac{I}{2\pi\sigma^2} exp(-\frac{(x^2+y^2)}{2\sigma^2}) \tag{2.5}$$

where $J\ (x,y)$ is the ion intensity distribution, I is the ion current intensity, and σ is a measure for the width of the beam.

The points on the shape are defined by pixel coordinates to which the beam will be deflected for milling, and the spacing between these points (pixel) is defined as overlap between the FIB beam Gaussians. The overlap should be assigned as in Fig. 2.5 in order to reduce the rippling between successive points maintaining the

milling rate and the ion flux uniform over all the shape points. A recommedend overlap to obtain a smooth milled surfaces is assigned as 63.7 % of the beam diameter [98].

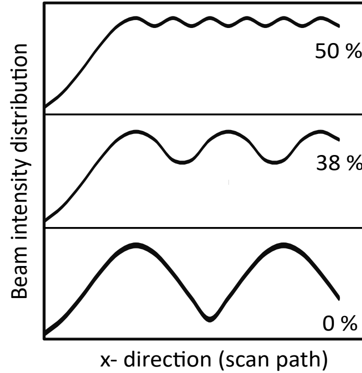

Figure 2.5: Ion beam density distribution along the milling scanning path with different overlap (%)

The FIB milling dose in nC is the product of the total milling time and the ion current. The total milling time is divided between the dwell time, which is the time the beam spends at each point, and the number of loops, which is the scan repetition of the milling at each point. The amount of sputtered material is correlated to how the total time is divided between the dwell time and the loops number (scan speed), where it is higher at longer dwell time and slower scan speed. Therefore, to mill a high resolution structure dwell time should be shorter and performed in several loops. There are different models and simulations found in [99] to calculate the ion dose to mill a fine 2D and 3D topography using FIB. The challenge in FIB milling is to obtain a high resolution machining in the micro and nano dimension with minimum sample damage or altering the sample electronic and optical properties. Hence, in this work we utilized the FIB to shape a hard mask for the Ar-milling rather than directly milling a nanocone to exclude Ga^{+} implantation in the gold nanocone, which may shift the nanocone plasmon resonance.

2.4 Focused electron beam induced deposition

Focused charged particles induced deposition is one method for direct-writing lithography. It is a flexible method to fabricate a nanostructure with high resolution without the need of a photoresist and regardless of the substrate topography. In our experiments, we use focused electron beam induced deposition (FEBID) to deposit a platinum pillar to serve as a first hard etching mask. The electron beam was used as an alternative for ion beams to perform an induced deposition process to avoid the undesirable effects of Ga-ions [100]. The FEBID deposition as in Fig. 2.6 depends on a precursor gas which dissociates under the exposure of the beam into volatile and nonvoltaile fragments. The shape of the deposited structure is primarily defined by the scan path of the e-beam.
The precursor gas is injected into the chamber and directed towards the substrate surface by the capillary tube of the gas injection system (GIS). This precursor gas carries the material atom of interest to be deposited, and commonly it is composed of organometallic molecules [101].

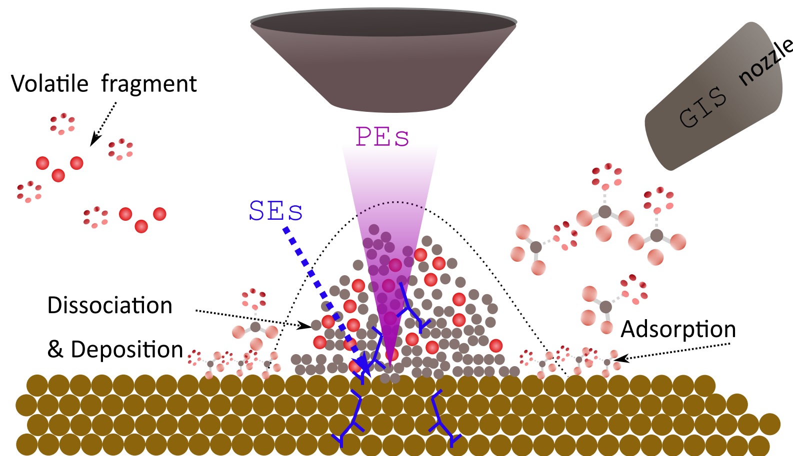

Figure 2.6: FEBID deposition of a nanostructure [102]; a focused electron beam dissociates the precursor gas molecules into a volatile fragment, and a non-volatile fragment which forms a nanostructure.

The GIS nozzle directs the precursor gas molecules towards the surface of the substrate. The precursor gas molecules are adsorbed at the substrate surface via chemisorption or physisorption. Their residence time at the substrate surface is inversely proportional to the substrate temperature. Hence, high dissociation probability of the precursor gas at the substrate surface is achieved with a lower

temperature since the residence time is longer. The interaction between the physically adsorbed layer of the precursor gas with electrons leads to its dissociation into the volatile fragment, and the non-volatile fragment which forms the deposited nanostructure.

The focused primary electron (PEs) beam will be deflected and scattered at the substrate surface and later within the deposited structure. The PEs scattering generates secondary electrons (SEs) and backscattered electrons (BEs). The volume of scattering inside the substrate depends on the substrate type and PEs energy. Once the SEs and the BEs possess an energy higher than the photoelectron workfunction they will be liberated from the surface of the substrate and can contribute in the FEBID process [103]. Hence, there are two types of electrons which interact with the precursor gas, the PEs of the focused e-beam (high energy electrons) and low energy electrons ejected from the substrate. Different types of dissociation channels may occur during the precursor gas decomposition. The channel type probability depends on the electron energy. The low energy electrons (i.e., SEs and BEs) yield the dissociative electron attachment (DEA) and the dipolar dissociation (DD) [104]. The DEA occurs when a target molecule captures an electron in a molecular orbital, and it becomes a metastable anion that can decay via dissociation [105, 106]. The DD occurs when the electrons have energy in the electronic excitation range of the target molecules and excite the molecules to the neutral dissociation state, which may dissociate into anions and cations [104, 107]. The high energy electrons (PEs) yield dissociative ionization (DI), which is the most relevant channel for the FEBID deposition [108]. The DI occurs when PEs have energy higher than the molecular dissociation ion limit, they excite the target molecules to the molecule ion resonance, which may dissociate into primary ions and/or neutral fragments [106, 108, 109].

Growth of Pillars using focused electron induced deposition

We used FEBID to deposit a Pt pillar with a circular cross section to be a first hard mask for dry etching. To deposit a Pt pillar, we used trimethyl(methylcyclopentadienyl)-platinum(IV) ($MeCpPt^{IV}Me_3$) organometallic molecules. The decomposition can be generally described as in eq. 2.6 [110]

$$\mathrm{MeCpPt^{IV}Me_3} + \mathrm{e} \rightarrow \mathrm{PtC_8} + \mathrm{H_2} + \mathrm{CH_4} \tag{2.6}$$

There are different parameters contributing to FEBID which are depending on the e-beam properties, molecular bonds of the precursor gas, the substrate, and heating due to irradiation with e-beam. The FEBID process is governed generally by the electron cross-section and current density. The PEs in contrast with SEs,

have a lower cross section but a much higher density. Thus, PEs have the main contribution in defining the deposited structure pattern. The FEBID growth rate is well described by considering only the PEs since it can be measured [111] as in eq. 2.7

$$\mathrm{R} = \mathrm{V_m} \quad \mathrm{N_0} \; \frac{\frac{gF}{\mathrm{N_0}} \quad \sigma J}{\frac{gF}{\mathrm{N_0}} \; + \; \sigma \; \cdot \; J \; + \; \frac{1}{\tau}} \tag{2.7}$$

where R is the growth rate, $\mathrm{V_m}$ is the volume of the nonvolatile part of the molecules, g is the sticking factor, F is the molecular flux density arriving at the substrate, $\mathrm{N_0}$ is the molecule density in the adsorbed monolayer, σ is the cross section for the dissociation of the adsorbed molecules under PEs bombardment, J is the current density of the PEs, and τ is the lifetime of an adsorbed molecule. A detailed review of the most important parameters and their roles in FEBID can be found in [103, 108, 112].

2.5 Ion beam milling

Ion milling is one of the dry etching methods and can be applied to a broad range of materials. Ion milling is the final step in the fabrication process. It is employed to etch with a hard mask, and shape the deposited gold thin film surface from an almost flat surface into a nanocone. It is a completely physical process where the material removal from the sample surface is achieved by ion bombardment. It is considered a micromachining method. Noble gas atoms are used in the ion milling, hence there is no chemical interaction with the samples. The ion beam is monoenergetic with the same charge and mass ions. The process starts by injecting noble gas atoms into the source chamber in a way that the chamber pressure is in the order of 10^{-3} torr. The atoms will be ionized by accelerated electrons which are generated from a heated filament. Then the noble ions are accelerated towards the target with energy in order of 1 keV to overcome the surface repulsive potential at the target surface.

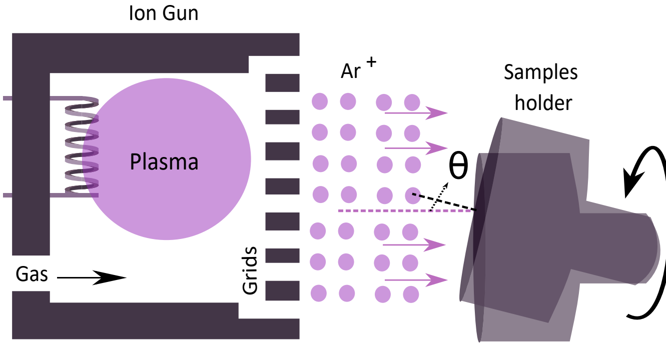

Figure 2.7: The process in the Ar^+ ion milling machine starts by inserting the Ar gas which will be ionized by the electrons. Then, the Ar^+ beam is accelerated with energy in the order of 1 keV towards the target. The sputter yield is $\propto$ (cos $\theta)^{-1}$.

The ions collide with and/or penetrate the target surface. Accordingly, the atoms or molecules can be sputtered from the surface after enough energy has been deposited from the collisions to break the bonds with the nearest neighbor atoms or molecules. The penetrating ions are deflected in successive collisions with target atoms and generate recoil atoms. The sputter yield ($Y(\theta)$) has a strong dependence on the ion incident angle (θ) as $\propto \cos^{-1}\theta$ described as in [113] by eq. 2.8;

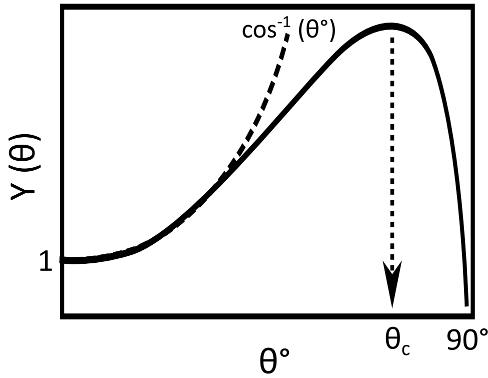

Figure 2.8: Sputter yield versus the ion angle of incidence [113].

$$Y(\theta) = (\frac{\pi^2}{4})\frac{sa^2nE_aR}{cos\ \theta}; \\ a = a_0/(Z_1Z_2)^{1/6} \tag{2.8}$$

where s is a crystal constant giving the number of removed atoms per unit energy deposited in the surface layer at the effective depth R, n the density of the atoms per unit volume, and E_a the value of ion energy which allows ion and

atom approach to a distance a, a_0 is the bohr radius, Z_1 and Z_2 are the atomic numbers of ion and target atom.

The variation of the average sputter yield of polycrystalline material with the incident angle can be generally presented as in Fig. 2.8. The Y(θ) increases with θ till a critical angle θ_c, above this angle the Y (θ) drops and approaches zero since the potential barrier of the target surface plane atoms reflects the ions and prevents them from penetration. The local erosion rate in the normal direction can be given as in [114] by eq. 2.9, if the Y(θ) depends only on θ.

$$c = \frac{J\mathrm{Y}(\theta)cos(\theta)}{N} \tag{2.9}$$

where J is the mean ion flux density, and N is the atomic density of the sample.

But, in crystalline material, the sputtering yield also depends on the crystal type and plane. To maintain a constant sputter yield and produce a smooth and symmetric surface the sample should be in a continuous rotatory motion around its axis during the ion milling [115].

Further, it was found that the presence of features such as impurities or different crystal plane orientations at the target surface lead to the appearance of structures like cones [116, 117]. The evolution of the patterned surface under ion milling can be predicted by a model based on wavefront theory [114]. Detailed reviews on ion milling can be found in [114, 118]. By elaborating the cones' formation phenomena combined with manipulating the ion milling incident angle, nanostructures with different geometries [67] were deliberately fabricated. This interesting principle will be discussed in the following chapters, where a disc-shape hard mask is employed to fabricate a gold nanocone on AFM cantilevers and tapered optical fibers.

Chapter 3

Methods and setup

The common SNOM setups employ either AFM or STM feedback mechanisms to maintain the tip-sample separation [35]. For this purpose, we fabricate a nanocone on top of an AFM cantilever and a tapered optical fiber, in order to be adjustable for both setups. Tailoring nanocones over such cantilevers and tapered fibers is a multistep process. First of all we chemically etch the optical fiber to have a sharp tapered tip. After this point fabrication of the nanocone on both the AFM-C and the tapered fiber in principle follows the same steps. The nanocone fabrication entails using the focused ion beam (FIB) machine to adapt the AFM-C and the tapered fiber sharp tip into a suitable plateau for the nanocone. Thus, the plateau will serve as a substrate, on which we fabricate the nanocone. Then, we coat the plateau with a thin film stack inside the evaporation machine, which consists of gold (Au) as the nanocone plasmonic material sandwiched between titanium (Ti) as adhesive material, and the upper top thin film made of dielectric material, either silicon dioxide (SiO_2) or aluminiumoxide Al_2O_3, as a protective layer. Then, we pattern a cylindrical hard mask on the top of the gold thin film. Finally, we apply Ar^+ ion milling, to etch the hard mask and the unprotected area. By terminating the etching process, the hard mask will be completely removed and the area underneath it transforms into a nanocone. In this chapter, we describe the nanocone fabrication process, where each section corresponds to a stage in the fabrication process. The sections are ordered in the same sequence of the nanocone fabrication process as following:

- In section 1 etching the optical fiber using the chemical etching method to obtain a sharp tapered optical fiber (T-OF).
- In section 2 milling the sharp tip apex of the AFM-C and the T-OF by using a FIB machine to have a plane plateau.

- In section 3 depositing of the thin films stack using the evaporation machine.
- In section 4 patterning the cylindrical hard mask for the Ar^+ dry etching.
- In section 5 etching the hard mask using an Ar^+ milling machine, to have the AFM-C and the T-OF with a plasmonic gold nanocone as a SNOM probe on its top.

3.1 Optical fiber chemical etching

We illustrate here the step of chemically wet etching the optical fibers using Turner's method [83,119], which has been discussed in chapter 2. Multimode optical fibers were used in this work, which are commercially available by Phoenix contact. The fiber core diameter and cladding diameter are 50 μm and 125 μm, respectively, thus the total fiber diameter is 125 μm. In spite of the material difference between the core and the cladding, we count only the total time to etch the total fiber diameter during the fiber etching. It is reported in [120] a similar notice on the etch rate of the cladding and core.

We prepared the optical fiber for chemical etching by removing the optical fiber outer protection plastic coat using sulfuric acid (H_2SO_4) solution at a temperature of 60 °C. After three minutes, we take out the fiber from the H_2SO_4, and gently wipe off the plastic coat with a clean room paper towel. Then we rinsed it with isopropanol, ethanol and deionized water respectively. We exclude using the mechanical stripper tool to remove the plastic coat to avoid any cracks in the fiber. The presence of such cracks can disturb the etching rate, and the tapered fiber profile.

Then, we started with tapering the optical fiber in hydrofluoric acid, where the wet etching was performed as in Fig. 3.1a by vertically immersing the optical fiber into a small beaker which contains HF acid using a samples holder with a micrometer screw to control the vertical movement. The beaker contains about 17.5 ± 2.5 ml HF solution with 44.5 ± 4.5% concentration, and is covered with an immiscible decane ($C_{10}H_{22}$) layer of 5 ± 1 ml. The meniscus formed as is depicted in Fig. 3.1b around the fiber walls, due to the surface tension difference between HF and decane, where its initial height depends also on the fiber radius. During the fiber etching as in Fig. 3.1b its radius is continually diminished and as well the height of the meniscus as the decance level is gradually dropping down, thus it protects more area from the fiber to be etched by HF. This dynamic of the meniscus forms a conical tapered fiber as has been discussed in detail in chapter 2. Moreover, decane acts as a lid for the etchant and thus eliminates the distortion of the etching process by avoiding the HF acid evaporation and the

interaction between etchant and air. The etching process was monitored from the side through an in-situ optical microscope. We withdraw the optical fiber from the HF when we expect it to be tapered with a very fine tip. The etching in only HF (49%) takes between 25 to 27 minutes. We obtained tapered optical fibers with a sharp tip as shown in Fig. 3.1c, and the tip apex radius ranges from about 30 to 500 nm.

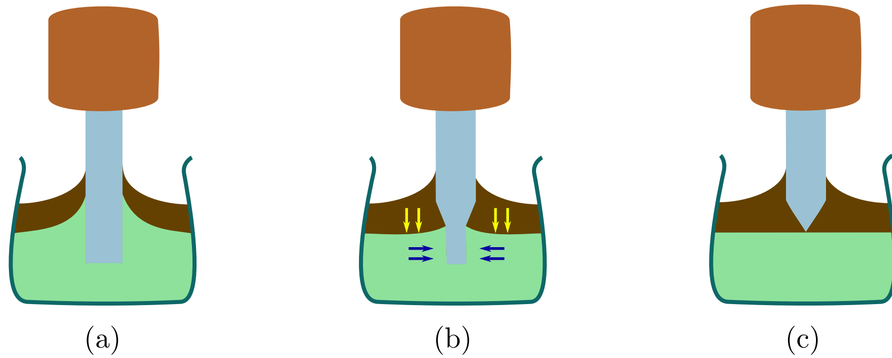

Figure 3.1: (a) The fiber immersed perpendicularly in the etching beaker, where the vertical movement is manually controlled by a micrometer screw. (b) Chemical wet etching of a multimode optical fiber in HF (49%), which is covered by a decane layer. The radius of the optical fiber gets smaller (blue lines), consequently the meniscus height drops (yellow lines). Hence, this increases the fiber area protected by decane. (c) The etching process is self terminated at an infinitesimally sharp tapered fiber, which is protected from HF by the decane layer.

It was hard to stop exactly at the finest tip apex radius, but still very often we obtained T-OF with tip apex radius below 300 nm. In principle the Turner method is a self terminating process, and once the fiber is in the organic layer (decane) it should not be etched. But, there is a high probability that the HF penetrates the organic layer, and overetches the tip very fast. Therefore, it has to be removed directly after the etching is finished otherwise if the T-OF remained in HF solution for extra one or two minutes it will get overetched. The fastest etchant to etch the optical fiber is pure hydrofluoric acid (HF) with 49% concentration, which is the highest available concentration of HF. But, to improve the smoothness of the tapered fiber other techniques have been employed as will be discussed later in chapter 5 by utilizing buffered HF with NH_4 to etch the core, and the dynamic etching method.

3.2 Plateau formation using FIB

The sharp tip of the AFM-C and T-OF is adapted in the FIB machine to obtain a plateau as an adequate platform for the nanocone fabrication. We illustrate in this section the experimental steps to obtain the plateau. First, we discuss milling the AFM-C tip, then the T-OF tip.

Milling the AFM cantilever tip

In this process, we transform the commercial non contact AFM-Cs into an adequate platform for the nanocone fabrication. The AFM-Cs used in this work are made of silicon, and available by NT-MDT. They have the shape of a sharp pointing pyramid of height about 16 μm, and their tip apex has a radius of curvature in the order of 10 nm, see full AFM-C specifications in Appendix A.1. To have an adequate platform, we mill a certain part from the AFM-C tip using a dual focused ion beam (FIB) / focused electron beam machine Strata D235 from FEI [56]. Consequently, we transform the AFM-C pyramid into a frustum geometrical shape thus an AFM-C becomes an adequate substrate for the nanocone fabrication.

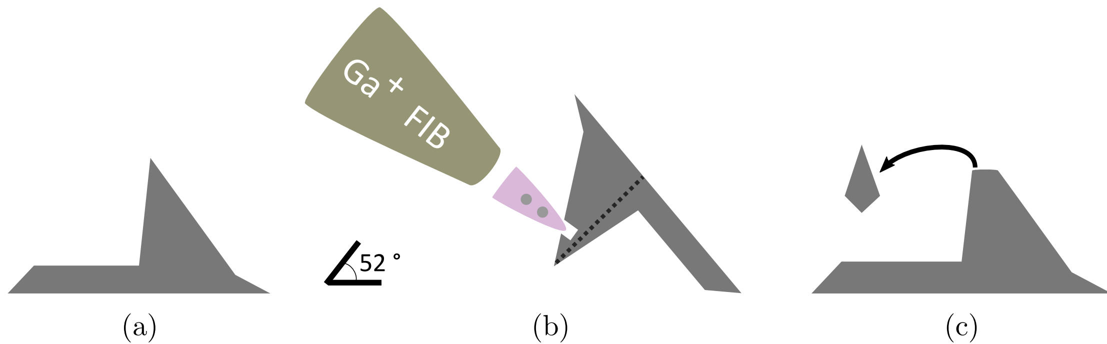

Figure 3.2: (a) AFM-C with a pyramid shape which has a sharp tip apex with a radius of 10 nm. (b) Ga^+ beam perpendicular to the AFM-C main axis (dotted line), where the AFM-C chip is tilted by 38° with respect to the FIB stage initial position. (c) After milling the tip apex using the FIB, the AFM-C has a flat plateau with a rhombus shape, ready to be used as a platform for the plasmonic nanocone fabrication

The AFM-C is placed inside the FIB machine, where the Ga^+ column is tilted by 52° with respect to the e-beam column, and 38° with the sample holder initial

position as shown in Fig. 3.2b. Assuming that the AFM-C tip long axis is perpendicular to the samples holder, thus we rotate the holder by 180° then tilt it by 38° to have the Ga^+ beam perpendicular to the AFM-C tip long axis. Then, we milled an adequate portion from the tip using a FIB aperture providing ion current of 20 pA ions at an accelerating voltage of 30 kV. The AFM-C tip sample detailed aligning and milling procedure is described in Appendix A.2.

Milling the tapered fiber tip

Before we proceed with the fabrication process, we fix the T-OFs as in Fig. 3.3a on top of a Si substrate which has straight rectangular grooves. Then, we place the T-OF in the FIB machine and tilt it as in Fig. 3.3b by 52°, thus the T-OF long axis and the Ga^+ beam become perpendicular to each other.

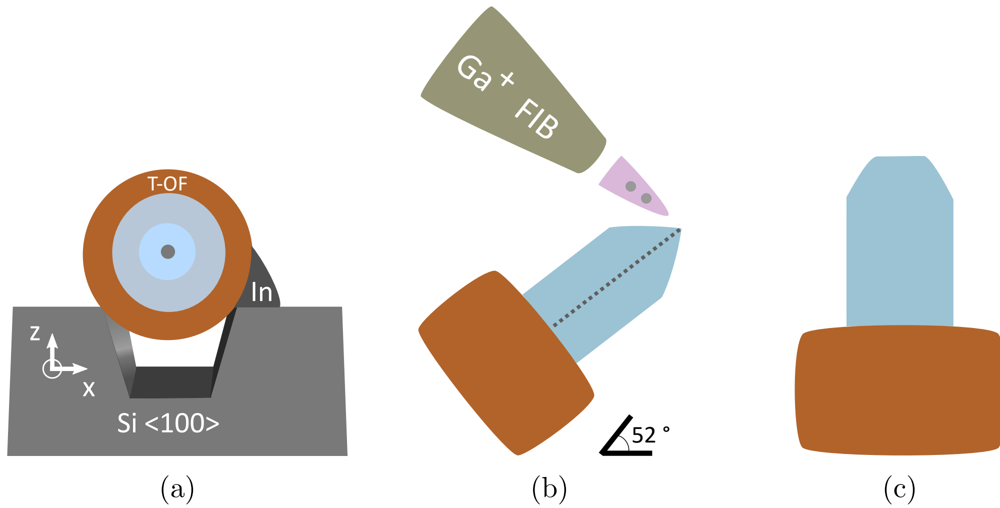

Figure 3.3: (a) The T-OF is fixed on a Si substrate with straight grooves to avoid any inclination in the x-y and the y-z plane. (b) The T-OF is positioned inside the FIB machine at 52° inclination, and the Ga^+ beam is perpendicular to its long axis. (c) The plateau is formed after milling the T-OF tip.

We assumed that the T-OF tip has a symmetric cone profile. To ensure a more centric positioning of the hard mask on the plateau of the T-OF, thus we selected under the Ga^+ FIB imaging mode the section where the diameter of the T-OF is between 300 and 500 nm. Then we started milling with a FIB current of 20 pA, and at an acceleration voltage of 30 kV. Thus, we obtained a plateau as in Fig. 3.3c which will be the substrate for the gold nanocone. The detailed

process of the T-OF tip milling is described in appendix A.3.

We used the rectangular grooves to ensure that there is no tilt in the x-y and y-z plane. During the tip apex milling, the Ga^{+} FIB will be perpendicular to the long axis of the T-OFs, thus the plateau will be flat. Furthermore, holding the T-OF on these grooves allows us to have homogenous films during the thin film deposition over the plateau, and during the Ar^{+} milling to adjust the angle between the plateau plane and the Ar^{+} beam. Therefore, we improve the symmetry of the fabricated nanocone. Additionally, it increases the process throughput where at least three T-OFs can be fabricated in parallel.

3.3 Thin film deposition

We coat the plateau with homogenous thin films using evaporation deposition. From the discussion in chapter 2 follows that, the vacuum pressure and sample position inside the chamber with respect to the evaporation source, both alter the film's morphology and thickness over the sample surface. Hence, we placed the samples in the evaporation chamber above of the evaporant source as in Fig. 3.4, where the plateau is perpendicular with the evaporant beam. Then, the evaporation chamber is pumped to achieve high vacuum condition in the order of 10^{-6} mbar. We coated the plateau with a thin films stack consisting of three different materials. In this stack, the first thin film serves as an adhesive material, and the top one is the hard mask, while in the middle is the plasmonic material of the nanocone. As a common procedure of the deposition process for the three thin films at vacuum on the order of 10^{-6} mbar, we shield the source by a shutter. Then, we keep rising the heating (e-beam) current through the evaporation source, once the source starts glowing we unshield it and start the thin film deposition. After having the intended thin film thickness, we shield the source by the shutter and start the evaporation machine switching off procedure. We start by depositing a Titanium (Ti) thin film which acts as an adhesive material. The Ti thin-film is deposited using e-beam assisted evaporation, and its thickness varies between 5 and 10 nm with a deposition rate of 0.8 Å/sec.

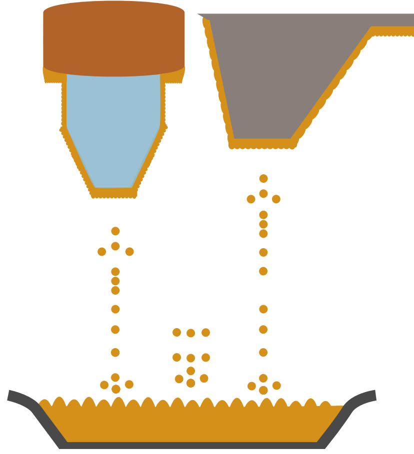

Figure 3.4: The samples are placed in the evaporation chamber above the evaporation source, and the plateau is perpendicular with the evaporant beam.

Successively on top of Ti, a gold (Au) thin film is deposited, which is the nanocone plasmonic material. The evaporation source of gold is Au nuggets placed in a boat made of tungsten. The Au is deposited using a resistive thermal evaporation method. The thickness of the Au thin film varies in the range from 100 to 150 nm, with a deposition rate of 1.8 ± 0.2 Å/sec. The upper top thin film is made of dielectric material mainly aluminum oxide (Al_2O_3) or SiO_2. It is deposited by e-beam assisted evaporation. The thickness of Al_2O_3 varies between 10 and 30 nm, with a deposition rate of 0.5 ± 0.2 Å/sec. In case of depositing SiO_2, the deposition rate is fluctuating, but we intend to deposit the same thickness as for Al_2O_3. The dielectric thin film thickness varies depending on whether it will serves as a second hard mask or as the only hard mask. In case it is the second hard mask it will be about 15 nm, while as the only hard mask it will be about 30 nm.

The dielectric thin film plays different roles in the nanocone fabrication process. It coats the gold thin film, accordingly protecting it from oxidation during transport and from carbon contamination during imaging before shaping it into a nanocone, and serves as the second hard mask. Additionally, It may show the boundary between the platinum hard mask and gold during the SEM imaging since they are both metals and separated by the dielectric layer. Thus, it may indicate when we should stop the Ar-milling to produce a sharp and high purity gold nanocone. Then, it has been used as an alternative to the Pt FEBID mask, and it replaces quite well the Pt mask.

The thin film thickness and deposition rates were measured in-situ during the

evaporation process employing a well calibrated quartz microbalance of a disc shape. We did not notice a significant deviation between the monitored values and the actual deposited thickness, by measuring the deposited films thickness using the contact profilometry (Solan dektak) on plane substrates.

3.4 Structuring the hard mask for dry etching

The next step is patterning the hard mask for the Ar^+ milling. The hard mask structure should be circular to produce a symmetric nanocone. There were two different methods to form the hard mask. Either depositing a platinum (Pt) pillar by FEBID or milling a ring through the dielectric thin film using the FIB. The hard mask base diameter defines the nanocone base diameter thus the plasmon resonance. Further, the step of patterning the hard mask influences the throughput of the fabrication process. In the case of the Pt pillar mask, the milling rate was not consistent, which can be due to the variation of its composition from Pt and hydrocarbons, also the evolution of the pillar shape during milling can slow down the etch rate. Accordingly, we split the milling process into distinct short milling steps. After each milling step, the samples were placed in the SEM to examine the progress of the pillar etching, which extends the fabrication time of the nanocone. On the other hand, a high throughput method of the nanocone fabrication is by using the dielectric disc directly patterned by the FIB since it has almost a constant milling rate, since they have almost same thickness and composition. Hence, fabricating a nanocone using a Pt pillar is a long process and has a low throughput compared to the ring milled by the FIB. We compare in detail the two methods in chapter 4. In this section, we describe the procedure of using both methods in structuring the hard mask.

3.4.1 Deposition of a Pt pillar as hardmask

The first approach to obtain a circular hard mask, is by depositing a cylindrical Pt pillar on top of the dielectric thin film (Al_2O_3 or SiO_2). The Pt pillar will serve as a first etch mask for the dry etching process. It was deposited inside the FIB by using the focused electron beam induced deposition (FEBID) technique. The samples were aligned inside the FIB machine as shown in Fig. 3.5 such that the e-beam is perpendicular to the coated plateau. The e-beam focus and aberrations should be carefully optimized since it affects the pillar shape and dimensions.

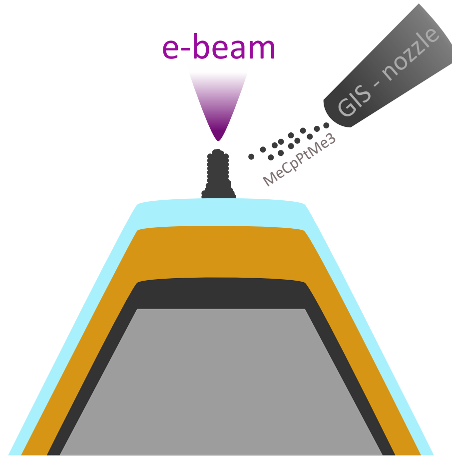

Figure 3.5: Arrangement for the FEBID of a Pt pillar where the focused e-beam is perpendicular to the coated plateau, and the GIS-nozzle supplies the MeCpPtMe3 precursor gas. The Pt pillar is deposited as a result of the dissociation of the MeCpPtMe3 into volatile and non-volatile fragments

The free working distance (FWD) between the e-beam column and the surface of the plateau was 9 ± 1 mm. This FWD is adequate to employ the GIS nozzle and protect the samples from any physical damage. Before inserting the GIS nozzle inside the FIB chamber, the precursor gas reservoir of the GIS is heated until the machine shows that it is ready. Then, we insert the GIS nozzle inside the chamber. It supplies the precursor gas for Pt which is Trimethyl (methylcyclopentadienyl) platinum(IV) (MeCpPtMe3). We deposit the Pt pillar by FEBID using the e-beam in a spot mode. In section 4.1.3 we will discuss the effects of the FEBID parameters involved such as the e-beam spot size, the accelerating voltage, and the exposure time.

3.4.2 Milling a cylindrical structure using FIB

The second method is to have a hard mask for Ar^+ milling by structuring a cylinder in the deposited dielectric thin film using Ga^+ FIB milling. Thus, the upper thin dielectric film which is made of Al_2O_3 or SiO_2 will have a disc shape, and serve as Ar^+ milling hard mask.

The FIB machine can read the pattern shape from two types of files, which are the pattern file with extension ".pat" and the stream file with extension ".str".

```
[Pattern_Summary]
Version=2.00
Patterns=1
[Pattern_1]
Name=Circle
InnerRadius=0.3
OuterRadius=1.8
CenterX=-2.9668
CenterY=1.35078
Typer=7
Beam=1
MaterialFile=None
Depth=1.00000
Dwell=0.000003
Overlap=0.0000
Time=45.0000000
GIS=0
EPD=0
Rotation=0.0000000
PixelsPerMicron=269.47364
```

(a)

S → Stream file
207 → No. of loops
24116 → No. of points

10	2125	1975
10	2124	1976
↓ Dwell time	↓ X-Coord.	↓ Y-Coord.

(b)

Figure 3.6: The FIB machine can read the pattern from two types of files; (a) The pattern file where the structure is defined as the geometry shape, the dimensions, the total time and the pixel size. (b) The stream file consists of the structure milling parameters and points coordinates.

Pattern file

The pattern file as shown in Fig. 3.6a includes the shape geometry, dimensions, the coordinate of only the pattern center, dwell time, and total time, and the number of pixels per micron which defines the pixel size in nm. Furthermore, it has different options depending on FIB machine facilities. The pattern file method is limited to the predefined geometries in the machine such as line, rectangle, circle, and ring.

Stream file

An example for the stream file is shown in Fig. 3.6b, it starts with three horizontal lines, and then three columns. The first line starts with 's' which defines the file as a stream file, the second line defines the number of loops, and the third line is the total number of points which form the structure shape. Then, the three columns as in Fig. 3.6b are from left to right for each point: dwell time, then x-coordinate and then the y coordinate, spanned over the 24116 rows which form the milling pattern.

In the milling process as shown in Fig. 3.7, the FIB reads the points coordinates from a stream file. These coordinates are in pixels. The magnification power during milling of the structure defines the pixel size in nm, for example at a magnification power of 20 kX the field of view is 11.52 μm x 11.52 μm corresponding to a pixel size of about 3 nm. Hence, we first record the magnification

power to calculate the pixel size in nm, then convert the pattern dimensions, the beam diameter, the pixel spacing from the nm unit to a pixel unit. The pixel spacing corresponds to the desired overlap (%) between the FIB Gaussians of the successive pixels.

The FIB divides the screen in x-direction into 4096 pixels ranging from 0 to 4096, while in the y-direction it is also divided into 4096 pixels, but the available coordinates values range from 280 to 3816 and other values are out of the imaging range in the y-direction.

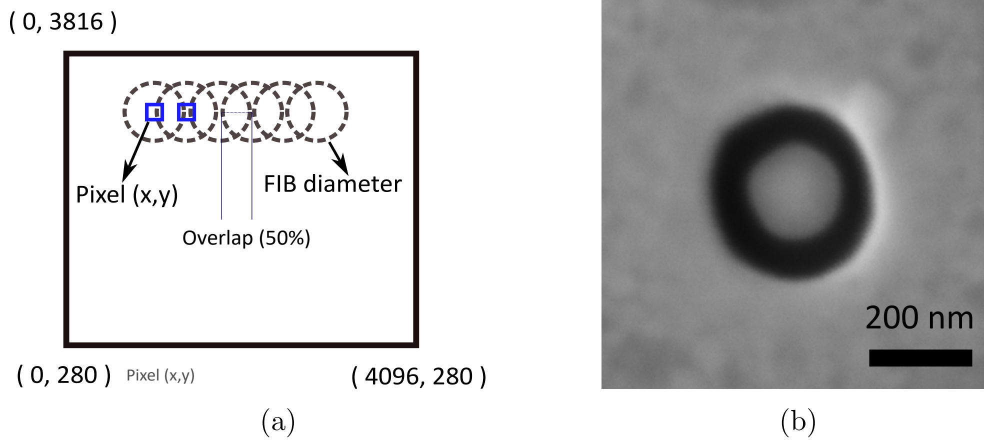

(a) (b)

Figure 3.7: (a) The FIB milling field of view is defined by the magnification power, consequently also the pixel size. The separation between two successive points should be equivalent to the overlap in % of the beam diameter. The FIB machine accepts the coordinate values in x-direction from 0 to 4096, and in y-direction from 280 to 3816. (b) Ring milled as a test with the FIB with inner core diameter 208 nm (± 5 nm) on substrate coated with a similar thin films system as the tips.

The hard mask is patterned over the plateau thin film stack by milling a 2D ring pattern as in Fig. 3.7b, which in 3 D is a cylindrical pillar. From the Fig. 3.8, the ring outer shell is the area which will be milled by the FIB, and the inner core will remain. The projection of the ring inner core on the coated plateau is a cylindrical pillar composed of the deposited thin films, and its top film acts as hard mask with a disc shape.

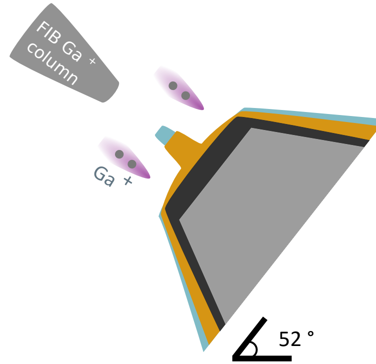

Figure 3.8: Milling a cylindrical pillar composed of the deposited thin films where the top one serves as a hard mask

The FIB pattering with a stream file is flexible to any geometrical shape, and the milling process can be optimized by considering the following three parameters;

- **Dwell time** which is the time duration of FIB milling at each point in the pattern file.
- **Number of Loops** defines the number of rewriting of the pattern rewrite, to achieve the defined structure form.
- **Points coordinates** The coordinates of two successive points are determined by the pixel spacing, which corresponds to the overlap between the FIB beam Gaussians at these points. The overlap value is assigned as a percentage of the FIB beam diameter. For example, in the case of the FIB beam diameter of 10 nm, the overlap of 50 % equals to 5 nm, and this corresponds to about 2 pixels at 20 kX magnification. The overlap value must be larger than the pixel size, thus, the FIB machine can deflect the beam to the point coordinate. The overlap is used to suppress the redeposition effect by removing the redeposited material during the FIB milling process, resulting in a high resolution milled structure.

3.5 Dry etching using Ar-ion milling machine

After having created the hard mask for the dry etching, the sample is placed in an Argon(Ar)ion-milling machine perpendicular to the Ar^+-beam. We pump the chamber till the pressure is in the order of 10^{-6} mbar. Then we open the valves

of the Ar gas, and the vacuum pressure increases to be in the order of 10^{-3} mbar.

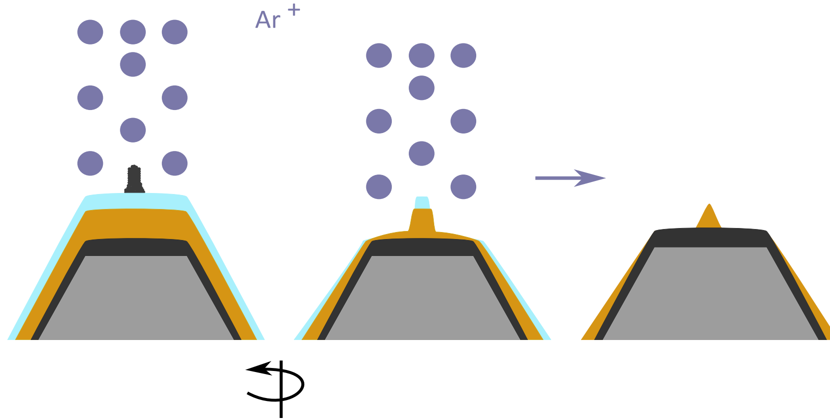

Figure 3.9: After Ar^{+} milling of the hard mask, the gold thin film is shaped into a nanocone. The fabricated nanocone can have a very sharp tip, depending on the right time to stop the milling process. Hence, we can obtain a high quality SNOM probe. The nanocone resonances can be tailored to match the measurements' spectral range, and it permits high resolution SNOM measurements.

The Ar^{+} beam with energy equal to 1 keV impinges on the samples, and the samples holder is kept rotating during the etching process. The rotation permits to have the same erosion rate at the hard mask edges, thus to fabricate a symmetric nanocone [66]. A gold nanocone is structured as shown in Fig. 3.9 after completely etching the hard masks. The thin film thickness of the gold corresponds to the nanocone height, and the hard mask base diameter approximately defines the nanocone base diameter.

Summary

In this chapter, we described the fabrication process of a nanocone on top of the AFM-C and the T-OF which are considered as promising SNOM probes. We choose to fabricate the nanocone on these two types of substrates in order to be implemented as a probe in the two most common systems of SNOM instruments. The fabrication process is a multistep process, and we mention the parameters which have been used in each step. In this work, the substrate for the nanocone fabrication is a plateau on top of AFM-C and T-OF. Since, the plateau is in

the sub-micron dimensions, e-beam lithography is not straight forward to be applied on such substrates. Hence, we prefer to elaborate two alternative methods in order to pattern a disc-shape hard mask on top of the plateau. These two methods are either an additive method by FEBID or a subtractive method by using the FIB. By milling the hard mask and the unprotected thin films in the Ar^+ milling, the deposited thin films are shaped into a nanocone. Hence, we obtain an AFM cantilever and a tapered optical fiber where their tip becomes a plasmonic nanocone. In the following chapter, we discuss more quantitatively the fabricated nanocone on the AFM cantilever samples, and the optimization of the process steps.

Chapter 4

Fabrication of gold nanocones on cantilevers

Gold nanocones were successfully fabricated on top of AFM-Cs to be used as SNOM probes. The fabrication process is described in chapter 3, where we applied as described in section 3.4 one of the two strategies to form the hard mask with a disc shape. After etching of the hard mask in the Ar^{+}-milling machine the nanocone is shaped [56, 70]. In this chapter, we discuss the optimization process for the crucial steps in the fabrication process. These crucial steps are milling the AFM-C tip to have an adequate plateau to be the nanocone substrate and patterning a dielectric circular disc to serve as a hard mask for the Ar-milling so by etching it a nanocone is shaped. There are two strategies to pattern the hard mask either by using the FEBID to deposit a Pt pillar or by milling a cylindrical shape through the thin film stack. We present the fabricated gold nanocones on top of the AFM-Cs, and compare the nanocones fabricated by each strategy. Finally, we find the LSPRs of the nanocones by 3D FDTD simulation of their scattering spectrum using Lumerical commercial software [31].

We characterize each step by SEM imaging, and from specific features that may appear in the images, we can monitor the progress of milling the hard mask and decide when the nanocone fabrication is completed. The features that may appear in the SEM images, as in Fig. 4.1, are a material contrast between the gold (metal) and the AFM-C (semiconductor), an offset between the nanocone base and the edges of the plateau, a sharp discontinuity as a kink at the side of the intermediate (e.g. platinum) cone which is probably a boundary between two different materials with different Ar-milling rate, and the cone height which should be $\leq$ the deposited gold film thickness. From the SEM image, we can evaluate the quality of the coating, and extract the dimensions and the symmetry

of the nanocone. Thus, it would be possible to calculate the plasmonic resonance of the nanocone.

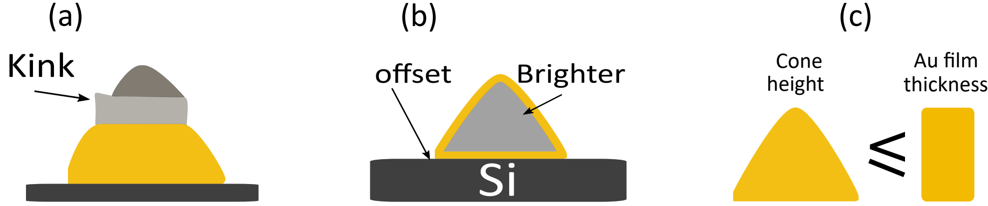

Figure 4.1: SEM image features to examine the progress of etching the hard mask. (a) A discontinuity appears as a kink at the milled structure side due to the slower etch rate of the oxide film. (b) The gold nanocone may show a brightness level higher than that of the Si AFM-C. (c) The measure of the nanocone height, which should be equal or less than the deposited gold film thickness.

Although the focus and astigmatism were well optimized, we still get a degree of image blur which is the source of the average deviation in the presented extracted dimensions in this chapter and chapter 5.

4.1 Optimization of the fabrication process

In this section we present the optimization of the crucial steps in the fabrication process. We start by optimizing the perimeter of the plateau which acts as a substrate for the nanocone. If the plateau is inadequately large with respect to the nanocone, it might shadow the nanocone and block the laser beam from exciting the LSPR during SNOM measurements. Then, we discuss the optimization of patterning the hard mask using either FIB milling or FEBID deposition. The hard mask influences the nanocone dimensions and its geometrical symmetry, consequently the quality of the SNOM probe. Furthermore, it plays a crucial role regarding reproducibility and throughput of the fabrication process.

4.1.1 Plateau optimization

The first step to fabricate a nanocone on top of the AFM-C as described in chapter 3 is to obtain an adequate plateau by milling the AFM-C tip, thus the silicon AFM-C tip is replaced by a plasmonic nanocone. We aim to find the optimal tip milling position by which the minimum distances between the nanocone and the plateau edge are achieved. In case of a large plateau, its edges may disturb the SNOM measurement by screening the laser from exciting the plasmonic nanocone.

It is important to tailor the plateau dimensions with respect to the nanocone dimensions. This has consequences for the nanocone plasmon resonance [61] and thus the SNOM measurements spectral range.

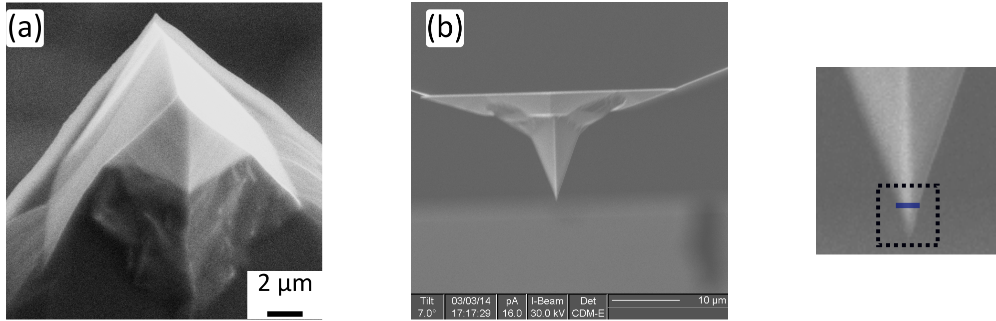

Figure 4.2: AFM-C image using Ga^+ FIB in imaging mode directly before milling its tip off. We can select only the width of the plateau (blue line) at which we will start the tip milling.

Nevertheless, it is not straightforward to visualize the full dimensions of the plateau in the milling field view as in Fig. 4.2a,b before milling the AFM-C tip. We can define only the plateau width Fig. 4.2b, which is equivalent to the short axis of the plateau. Hence, there is a probability of milling a wrong portion of the AFM-C tip.

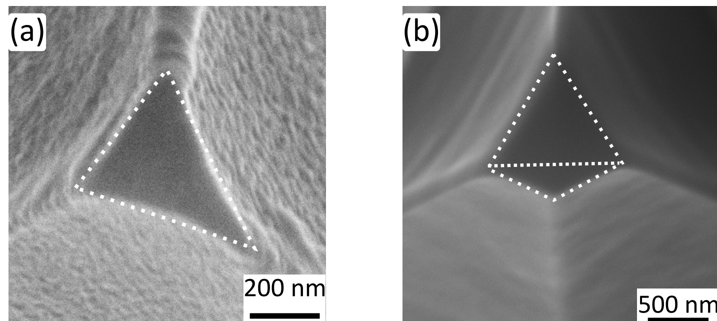

Figure 4.3: The plateau geometry obtained by cutting the AFM-C tip at width $\leq$ 330 nm is a triangle as in (a) while at $\geq$ 400 nm it is a rhombus as in (b).

The geometry of the AFM-C is a rhombic pyramid, although it may happen that two sides merge together near the tip, and the AFM-C pyramid top part

becomes triangular, while the rest is rhombic. We found that the plateau shape can vary with width, where by milling the tip at a width of $\leq$ 330 nm as in Fig. 4.3a the plateau has a triangular shape while at a width of $\geq$ 400 nm it is rhombic as in Fig. 4.3b. It is necessary to develop a model from which we can determine the appropriate point to start the tip milling process, with respect to the nanocone base diameter. Accordingly, we can adjust the plateau perimeter to the desired nanocone base diameter.

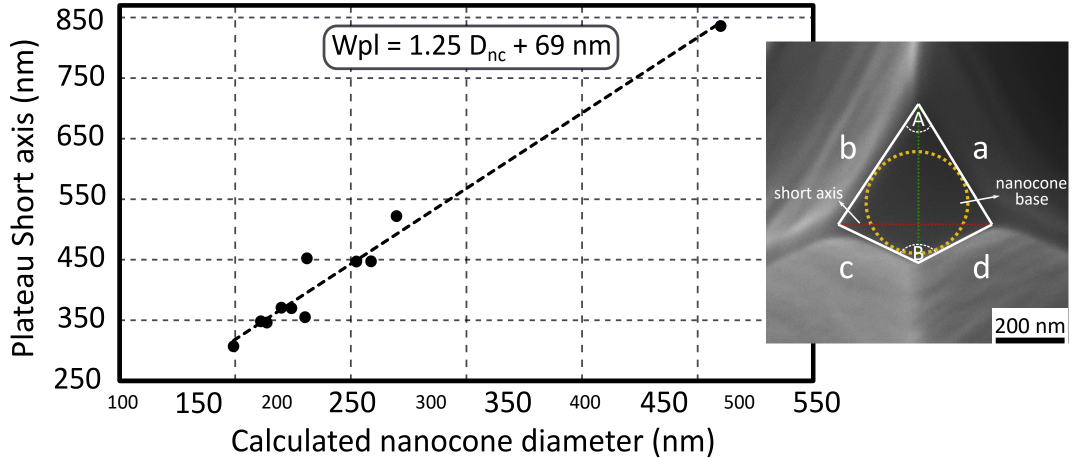

Figure 4.4: A relation between the diameter of an incircle which is tangential to all plateau sides and the plateau horizontal diagonal (experimental values). The dotted line is a linear fit to the experimental values as represented in eq. 4.2. The inset shows how the plateau fits with the calculated nanocone base diameter using eq. 4.1.

This model is based on the plateau dimensions which were extracted from the plateau SEM images after milling a set of AFM-C tips. We consider the plateau to have quadrilateral (rhombus) geometry, which is the more likely to be formed after the tip milling rather than a triangle. Then, we determine the geometrical plateau parameters, and the nanocone base diameter as an inscribed circle of a quadrilateral using eq. 4.1 from [121];

$$D_{\text{nc}} = \frac{2A_{\text{pl}}}{s_{\text{pl}}} = \frac{4\sqrt{(s-a)(s-b)(s-c)(s-d) - abcd \cdot cos^2\left[0.5(A+B)\right]}}{(a+b+c+d)} \tag{4.1}$$

where D_{nc} is the maximum possible nanocone diameter, A_{pl} and s_{pl} are the plateau area and semiperimeter, respectively, a-d are the plateau sides, A and B are the opposite angles of the plateau.

By applying eq. 4.1, the nanocone can be fitted at the center of the plateau with the minimum distances from the plateau edges and reduce the probability of the plateau disturbing the probe illumination and sample signal detection. The empirical geometric relation is the equation of the fitting line in Fig. 4.4, it is a relation between the nanocone base diameter and the minimum plateau short axis, given by,

$$W_{pl} = 1.25 \times D_{nc} + 69 \text{ nm} \tag{4.2}$$

where W_{pl} and D_{nc} are the plateau width and the nanocone base diameter, respectively.

According to the eq. 4.2, we can mill the tip more precisely depending on the required nanocone dimensions. For example, as delineated in Fig. 4.4 inset to fabricate a nanocone with a base diameter equal to 304 nm, we must start the milling process at the point where the short axis is equal to 447 nm.* Hence, during the imaging mode using the Ga^+ beam as in Fig. 4.2b, we can define the appropriate starting point for milling the tip.This provides a simple tool to design a well suited SNOM probe.

But, additional offset between the incircle and plateau sides might be demanded to have the nanocone more centric on the plateau, this depends on how precise the hard mask can be positioned on the plateau.

4.1.2 FIB milling of a cylindrical hard mask

The hard mask is patterned by using a subtractive process, where the FIB milled a cylinder pillar through the thin film stack. The pattern milled by the FIB has a ring shape as mentioned in chapter 3, where the ring core is the hard mask for dry etching. There are two processes occurring during the FIB milling: sputtering and redeposition. The sputtering effect happens when the incident ion transfers an amount of momentum to the target surface atoms via a cascade of collisions. However, a redeposition process can occur as an undesirable side effect in which the sputtered atoms are redeposited within the volume being sputtered. The redeposition depends on the milled structure areal geometry and aspect ratio between its side walls and the width. To minimize the redeposition effect we need to have an overlap (OL) between successive milling points of at least 30 %

*a = 411.2 nm, b = 422 nm, c = 254 nm, d = 236 nm, A = 65.6° and B = 132° are the used values in eq. 4.1 for the D_{nc} and the W_{pl} calculations drawn in the inset.

of the ion beam diameter [98], and perform the milling process rather in more loops than with longer dwell time. The FIB milling is elementarily governed by the sputtered yield, i.e. the number of the removed atoms per incident ion as in eq. 4.3. It can be translated into a sputter rate as in eq. 4.5 i.e. the removed volume per the incident ion dose. This allows the determination of the required ion dose i.e. sputter time at a given ion current, for any desired shape to be milled.

$$\text{Sputter yield} = \frac{\text{No. of removed atoms}}{\text{Incident ions}} \tag{4.3}$$

$$= \frac{\mathrm{N_A} \times \rho \times \text{ Sputtered volume} \times (\text{Molar mass})^{-1}}{\mathrm{I}_B \times \text{ total milling time}} \tag{4.4}$$

$$\text{Sputter rate} = \frac{\text{Sputtered volume}}{\text{Ion Dosage}} \tag{4.5}$$

where $\mathrm{N_A}$ is the Avogadro's number, ρ is the density and I_B is the number of incident ions per time.

In the milling, the FIB reads the x and y coordinates of each point in the ring shape from a stream file. These coordinates are defined in pixels. Hence, we convert the pattern dimensions, the FIB beam diameter, and the pixel spacing from the nm unit to the pixel unit. The conversion from nm to pixel is calculated from the magnification power which gives the number of pixels in micrometer consequently the pixel size in nm.

In order to find the optimal ion dose to mill the ring shape, we should find the sputter rate of SiO_2. Thus, we milled a ring with an inner and outer radius of nominally 80 and 700 nm, respectively, with two different ion doses by varying only the no. of loops. The first mill dose is 0.44 nC obtained by milling for 20.06 sec performed by 60 loops, the second dose is 0.74 nC obtained by milling 100 loops which corresponds to 33.43 sec. The beam current was 22 pA and the beam has a diameter of about 10 nm, with pixel separation of OL 50 % which is equal to 5 nm. In pixel units, the ring was milled at 20 kX magnification in which the pixel equals to about 3 nm thus the OL 50 % corresponds to about 2 pixels.

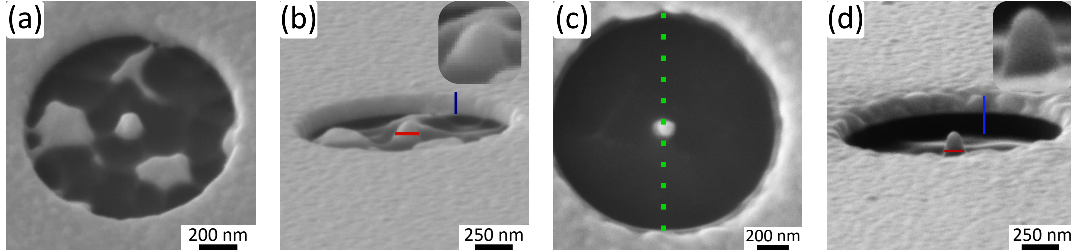

Figure 4.5: Milling a ring in SiO_2 (bright) on Si (dark) using a FIB current of 22 pA, where a cylindrical hole is produced with an outer radius (dotted green line) equal to 700 nm. (a) Top view and (b) Tilted view at 45° for 60 loops. The pillar in the center has a height (blue line) and a radius at FWHM (red line) equal to 123 nm and 79 ± 4 nm, respectively. For 100 loops (c) Top view, and (d) tilted view at 18°, with a pillar height and FWHM radius equal to 268 nm (145 nm is Si) and 66 ± 4 nm.

The milled ring with 60 loops as in Fig. 4.5b is almost only SiO_2, but from Fig. 4.5a the bottom of the cylinder is not uniform and has unmilled areas alike islands. By milling the same pattern with 100 loops, the milling goes deeper into the Si substrate as seen in Fig 4.5c. On the side of the ring core shape, the inner radius which corresponds to the hard mask radius varies significantly at the top, and has a shape of a hillock rather than a symmetric cylinder. It is overmilled at the FWHM by about 14 ± 4 nm compared to the assigned values.

To determine the sputter yield of SiO_2 and Si, we used the dimensions and milling parameters of the patterns in Fig. 4.5a,c. The sputter yields for Si and SiO_2 are calculated by eq. 4.4 using the values in Appendix A.4. They are 5.9 (at/ion) for Si and 1.8 (at/ion) for SiO_2. In contrast the value calculated by the sputter yield calculator in [122] for Si is 3 (at/ion) and reported in [123] as 4 (at/ion).

Further, the value of the outer radius defines the extension of the FIB milling on the sides/flanks of the AFM-C pyramid. Thus, a small outer radius leads to forming sharp edges close to the nanocone, which may increase the scattering and thus decrease the signal to noise ratio. The optimal way to define the outer radius is to define it in a similar way as in section 4.1.1, by considering the AFM-C as a rhombus inscribed in a circle. Thus, in the same step of patterning the ring, we can etch the residual thin films on the AFM-C walls and/or reshape part of the AFM-C pyramid near the nanocone into a cylinder to ensure a better optical access to the nanocone.

4.1.3 Platinum pillar deposition

The next step is to optimize the FEBID deposition process of the Pt pillar, which acts as the first hard mask for the Ar^+ plasma dry etching on top of the oxide layer which is the second mask. The adequate pillar height from the fabrication process throughput point of view, is the exact height that would be completely etched at the boundary of the gold thin film. Thus, as depicted in Fig. 4.6, the etching time for the pillar height should be equivalent to that of the dielectric thin film (SiO_2 or Al_2O_3) in the Ar^+ plasma dry etching. Consequently, etching the pillar should pattern the second mask with a disc shape made of the oxide layer as in Fig. 4.6c. After the disc being etched the gold nanocone will be formed as in [66].

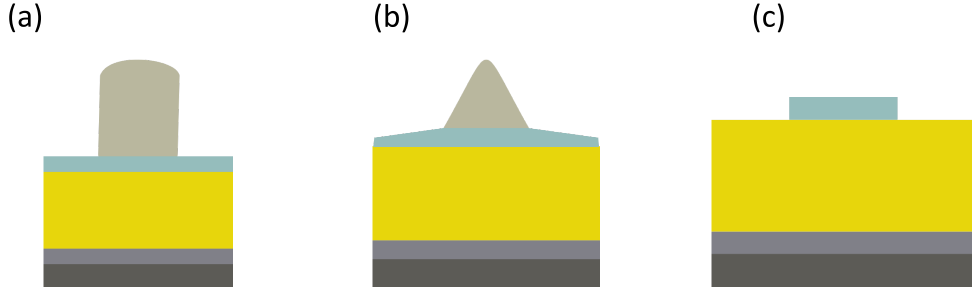

Figure 4.6: (a) The Pt pillar is deposited on top of the thin film stack. (b) The pillar surface evolution during the Ar^+ plasma dry etching turns the cylinder into a cone. (c) The adequate pillar height should have the same etching time as the dielectric thin film [66], where the pillar is totally etched, before the Ar^+ starts milling the gold thin film.

The Pt pillar dimensions influenced the final form of the SNOM probe. Primarily, the pillar base diameter will define the base diameter of the nanocone, while its geometrical asymmetry can lead to a deformed conical nanostructure. Furthermore, the pillar height affects the thickness of the residual thin films at the side walls of the AFM-C. Hence, increasing the pillar height increases the etching time, thus reducing the thin film residual at the sidewalls of the AFM-C. Consequently, it is important to optimize the FEBID deposition of the Pt pillar in order to have a good control on the dimensions of the fabricated nanocone and the overall quality of the SNOM probe.

The Pt pillars were deposited using FEBID by focusing the e-beam in a spot mode. We deposit a series of Pt pillars to find the growth rate as nm/nC. The dose is controlled mainly by the FEBID parameters, which are the accelerating

voltage, the e-beam current, and the exposure time.

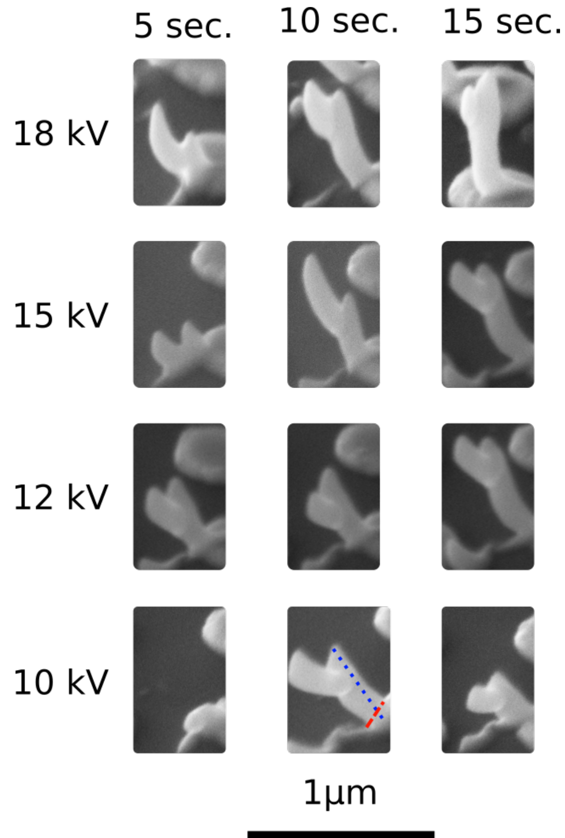

Figure 4.7: Pt pillars deposited by FEBID on top of gold discs to optimize the FEBID process parameters. They were deposited in spot mode using accelerating voltages and exposure times ranging from 10 to 18 kV and 5 to 15 sec, respectively. The blue dashed line and the red dashed line correspond to the Pt pillar height and base, respectively.

We conduct an experiment to optimize the FEBID process of the Pt pillar. In this experiment, we examine the relationship between the accelerating voltage, the e-beam dose, and the pillar dimensions and symmetry. At the same time, we examine the precision for growing the Pt pillar at the center of the AFM-C plateau. Thus, we prepare a silicon substrate with arrays of gold discs with a diameter of about 400 nm. The discs were fabricated by e-beam lithography, and they serve as an analogy to the AFM-C plateau. The Pt pillars were deposited on the gold discs as depicted in Fig. 4.7. The FEBID dose for the pillars deposition ranges from 630 to 2070 nC. This dose range was obtained by using the e-beam

current from 120 to 138 pA at four different accelerating voltages of 10, 12, 15, 18 kV and at each voltage three exposure times as 5, 10, 15 sec are used. The e-beam current increases by increasing the acceleration voltage value.

Pillar Symmetry

The deposited pillars suffer from a bend at their base and a branch grows near their tip. The bend at the base can be attributed to the fact that the pillar was grown at the edge of the gold disc and displaced from the center. The branch near the tip can be due to unexpected-beam drift.

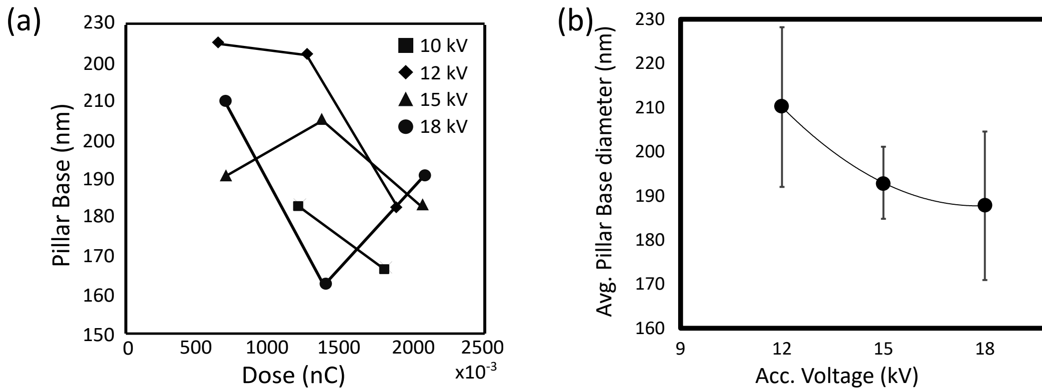

Figure 4.8: (a) The relation between the Pt pillar base and the e-beam dose at different accelerating voltages. (b) The relation between the Pt pillar average base diameter and the accelerating voltage. The base diameter decreases with increasing the accelerating voltage, due to less contribution of the secondary electrons in the FEBID process [124].

Pillar base vs Dose

Controlling the pillar base diameter is relevant to tailor the nanocone base. Fig. 4.8a shows that the variation of the pillar base has no clear dependency on the e-beam dose in spot mode. Alternatively, we check the variation of the base with the voltage, so we consider the average base diameter of the pillars deposited at the same voltage. Thus, we can see in Fig. 4.8b that the diameter tends to decrease at higher voltage. This decrease at high voltage can be due to less contribution of the secondary electrons. Since the average depth of the secondary electrons at higher voltage is larger than their escape depth, thus more secondary

electrons are going to be absorbed within the thin film [124, 125].

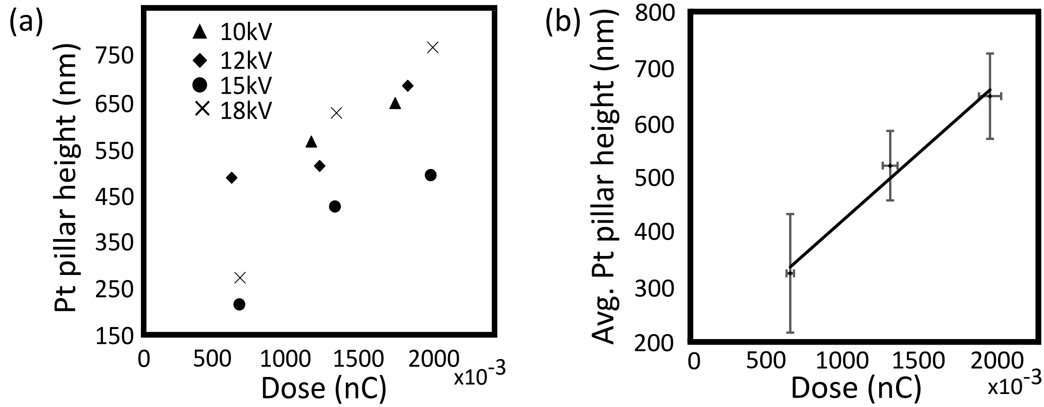

Figure 4.9: (a) The height of the deposited pillar increases by increasing the e-beam dose. (b) The average pillar height shows roughly linear dependency on the average e-beam dose.

Pillar Height vs Dose

In Fig. 4.9a the height of the pillar increases with increasing the e-beam dose, and as shown in Fig. 4.9b the average height of the deposited pillars increases roughly linearly with increasing e-beam dose. To find the pillar growth rate, we count only the pillar height as indicated by the blue line in Fig. 4.7 and exclude the branch grown near the tip. The Pt pillar growth rate deduced from the fitting line in Fig. 4.9b is 250 $\pm$ 92 nm/nC, this is based on the applied dose and the corresponding height extracted from the SEM images of all the deposited pillars. The mean deviation stems from the asymmetry of the pillars, which makes it hard to precisely find the pillar height.

4.2 Results and Discussion

In this section we will present selected samples, each sample having a single gold nanocone fabricated on top of an AFM-C. We attempt to fabricate nanocones of about 100 to 150 nm height, which can be well monitored by splitting the Ar-milling process into 30 sec duration steps since the Au milling rate is about 100 nm/min. Hence, we can terminate the fabrication process before the nanocone is destroyed. Further, nanocones with about 100 nm dimensions and aspect ratio 1

had been successfully employed as SNOM/TERS probe and can be for practical measurement effectively excited by He-Ne laser wavelength line 633 nm [56].

The first part will discuss nanocones fabricated using a Pt pillar as the first hard mask. The second part will discuss samples fabricated using a disc mask which is milled with the FIB. We had reported in [70] the fabrication method of a plasmonic nanocone on top of AFM-C by employing the FIB in patterning the Ar^+ milling hard mask.

Each step of the nanocone fabrication process was examined using SEM. Thus, we can elaborate a fabrication process to achieve reasonable reproducibility and throughput of nanocone novel SNOM probes.

4.2.1 Nanocone fabricated using Pt-Mask

We deduce from section 4.1.3 the deposition e-beam dose, which is required to deposit a Pt-pillar with a height between 80 and 300 nm. Therefore, the e-beam dose will range from about 0.3 to 1.2 nC. It is obtained by focusing the e-beam in spot mode for exposure times ranging from 3 to 6 sec, at accelerating voltages of 8 and 10 kV, and current varying between 110 pA to 120 pA. The current increases when increasing the accelerating voltage. According to the pillar growth rate of 250 $\pm$ 92 nm/nC from section 4.1.3, this will produce a pillar with a height ranging from 75 to 272 nm, which is almost the case in the presented samples. Regarding the base diameter, it will range from about 80 to 130 nm, but there was no clear way to well control the pillar diameter. We extracted from the SEM images the dimensions of the mask and the nanocone. Consequently, the values of the dimensions have an average deviation between $\pm$ 7 to 15%, due to an avoidable blur in the images arising mainly from the astigmatism.

Starting the discussion with sample **A** which has a nanocone on top of an AFM-C. The SEM images of the fabrication steps in **A** are depicted in Fig. 4.10. After milling the AFM-C tip, we obtain a plateau with a rhombus shape as in Fig. 4.10b. Then, we coat it with the thin film stack, where the intended thickness of the Ti equals 5 nm, the Au film thickness equals 100 $\pm$ 10 nm, and the upper thin film was made of SiO_2 with an intended thickness of 25 $\pm$ 5 nm. Afterward, we grow the Pt-pillar as in Fig. 4.10d by the FEBID using an e-beam exposure dose of about 0.4 nC, performed by focusing the e-beam for about 4 seconds in a spot mode at accelerating voltage and current of 8 kV and 110 pA, respectively. The deposited pillar has 60° tilt angle with respect to the plateau surface. The pillar base has a tail part, thus we consider the pillar full width at half maximum (FWHM) as the effective diameter which defines the nanocone base in Ar^+ milling. The pillar height is about 77 nm, and its FHWM and base

diameter are about 45 and 73 nm, respectively. It was etched for 2 minutes in the Ar^+ milling machine. As a result of the dry etching of the Pt pillar and the SiO_2, the gold thin film was shaped into a plasmonic nanocone as depicted in Fig. 4.10e with a tip radius in the order of 9 ± 3 nm with an opening angle of 49 $^\circ$ and a height and base diameter of 94 ± 3 nm and 49 ± 3 nm, respectively.

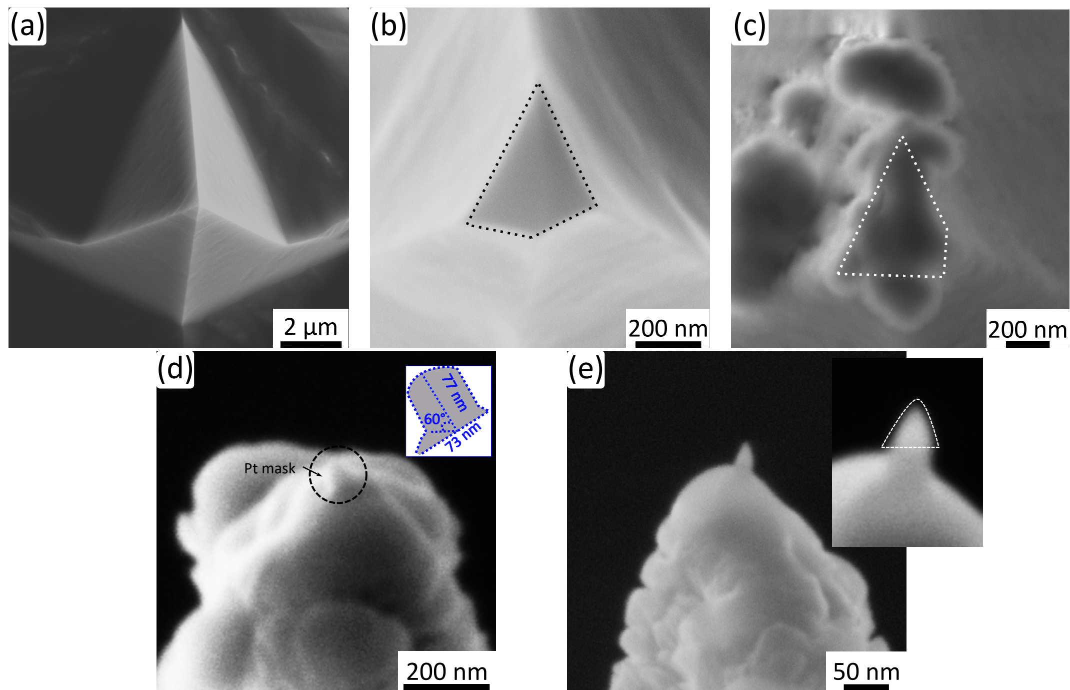

Figure 4.10: SEM images of the nanocone fabrication for sample **A**; (a) The AFM-C before cutting its tip apex (b) The formed plateau after FIB milling the tip. (c) Coated AFM-C with three thin films, where the upper one is SiO_2. (d) Pt pillar with height and base diameter of 77 nm and 73 nm, respectively. (e) Gold Nanocone formed after 2 min Ar^+ milling with a height on the order of 94 $\pm$ 3 nm and a tip apex radius of about 9 ± 3 nm, thus it overetched by 6 ± 3 nm.

We expect that the hard mask etching was completed, since the SEM image shows a difference in the material contrast, where the conical shape is brighter than its underneath layer. The etching time of 2 min is sufficient to mill the Pt pillar. Further, the pillar tilting with respect to the plateau surface will probably lead to a higher etching rate, since Ar^+ milling is a strongly angle dependent process.

On the other side, there is an uncertainty to it being a pure gold nanocone stemming from the difficulty in controlling the SiO_2 thickness during its deposition which forms unexpected accumulations as delineated in Fig. 4.10c located near to the plateau. These accumulations might have occurred, since the deposition rate of SiO_2 was strongly fluctuating and hard to control. Finally, by counting on the material contrast in the SEM image, the etching time, and the structured nanocone dimensions and its shape continuity as in Fig. 4.10e, we assume it is more likely to be a slightly overetched gold nanocone by 6 nm compared to the intended thickness of the gold thin film (100 $\pm$ 10 nm).

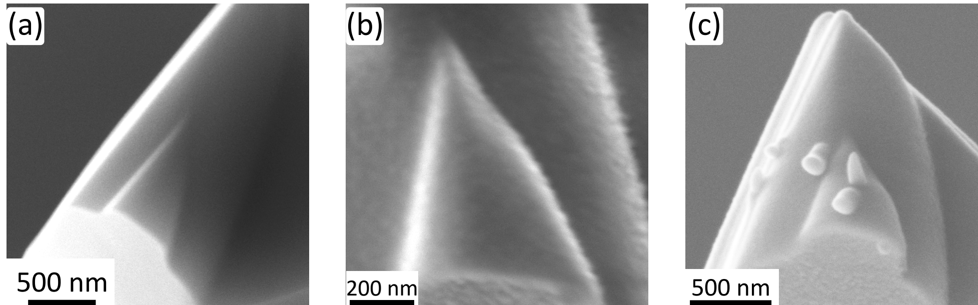

Figure 4.11: (a) Sample **B** plateau with stairs, due to the refocusing of the ion beam at different parts of AFM-C tip during the ion beam imaging mode. (b) After the thin film stack deposition for the first try. (c) The misplaced Pt pillars with a tilting angle with respect to the plateau surface.

In sample **B** as in Fig. 4.11a the plateau formed by FIB milling has a stairs shape, which may be due to refocusing of the ion beam in the imaging mode at different parts of the AFM-C tip. Additionally, in sample **B** after the thin film deposition as in Fig. 4.11b, the FEBID of the Pt pillar did not work well. Although we deposited three pillars as in Fig. 4.11c in order to get one at the center of the plateau, all of them have strongly tilted shapes. Consequently, it was not possible to fabricate a single nanocone with a symmetric geometry after etching these pillars.

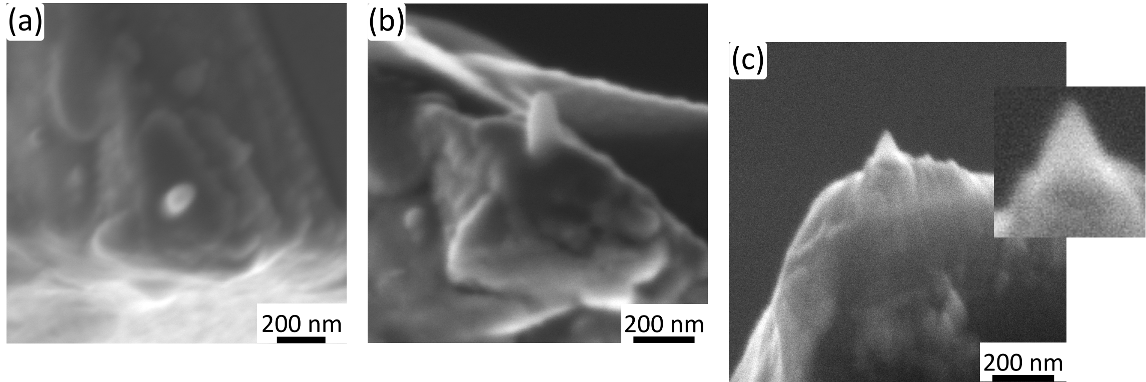

Figure 4.12: (a, b) SEM image of the top and side views of the Pt pillar deposited on the sample **B** in the second try. Its height equals to 211 nm, and it has a base diameter of 105 nm. (c) After 5 min etching, the gold nanocone with a tip radius of about 11 nm was shaped.

We etched all the pillars and the deposited thin films in the Ar^+ milling machine. Then we started a second try with sample **B**. It was coated with a thin films stack where the thickness of the gold thin film is about 100 nm and of an Al_2O_3 film about 12.5 $\pm$ 2.5 nm. As a result of the plateau shape and the reusing of the AFM-C, the deposited thin films in the second try formed some grains as in Fig. 4.12a, while the plateau was coated homogeneously. The Pt pillar FEBID process was performed by current 120 pA at accelerating voltage 10 kV and with an exposure time of about 5 sec, thus the e-beam dose was about 0.6 nC. The pillar as depicted in Fig. 4.12a,b has a uniform shape with 211 $\pm$ 8 nm in height and a base diameter of 105 $\pm$ 8 nm. The gold nanocone in **B** was fabricated after 5 min etching in the Ar^+ milling machine. The nancone has a tip radius in the order of 11 $\pm$ 4 nm, while its height of 99 $\pm$ 8 nm is very close to the applied 100 nm gold film. In sample **B**, we are almost sure that the nanocone is made of highly pure gold since all the aspects extracted from the SEM image are consistent, such as the continuity in the cone shape, image contrast between the cone and the substrate, and the cone height with respect to the deposited gold thickness.

We should point out that, after fabricating the nanocone there are remaining metal thin film residuals on the side walls of the AFM-C pyramid. They are located very close to the nanocone. These residuals can be a source of noise signals, when the nanocone is implemented in a SNOM measurement. To avoid this in sample **C**, as shown in Fig. 4.13 we try to examine the possibility to etch the thin films at the side walls as well as the hard mask at the same time. We

deposited for this purpose a long Pt pillar with a height and a base diameter equal to 509 nm and 120 nm, respectively. The FEBID exposure time was 9 ± 1 sec, accordingly the e-beam dose was 1.17 ± 0.13 nC. The dry etching of the hard mask was completed in 23 minutes. We found that a gold nanocone is shaped on top of a Si cylinder as in Fig. 4.13h. This Si cylinder is part of the AFM-C top shaped by Ar^+ milling with about 350 nm in height and 250 nm in diameter. The fabricated gold nanocone has a tip radius equal to 14 ± 3 nm and an opening angle of about 70°, and its height is 100 ± 6 nm. The pillar shape evolution after 3 min, 14 min and 23 min etching is depicted in Fig. 4.13d,e,f, and it is clear from Fig. 4.13e that the pillar tip is shaped into a cone during ion milling.

In contrast, to the pillars in sample A and sample B, the pillar in **C** shows a slower etch rate. We had experienced this with different samples which have a pillar height ≥ 500 nm. In the case of the long pillar, its tip during Ar^+ milling becomes a cone which makes it more stable and etching more slow compared to a plane surface. The etching of pointing structures such as ridges and cones shows a slower etching rate compared to the plane surface, and theoretically the cone can have an infinite stability [126]. The stability of the cone is either due to ion reflection [116] or the anisotropy of energy density deposition [126].

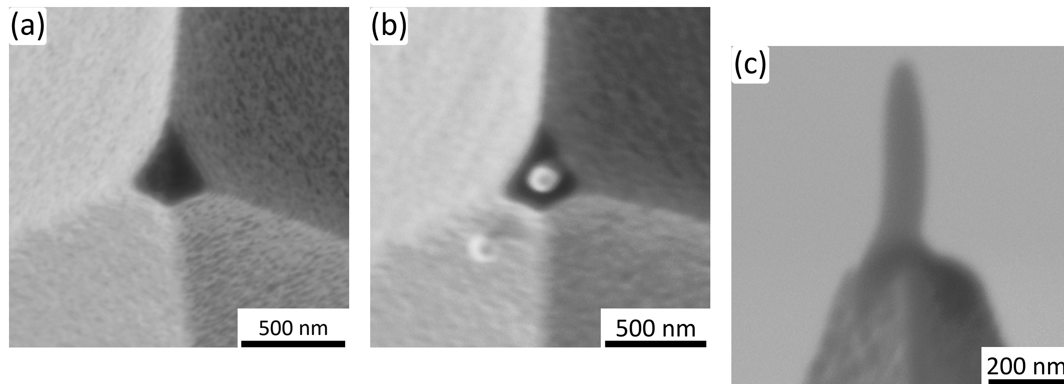

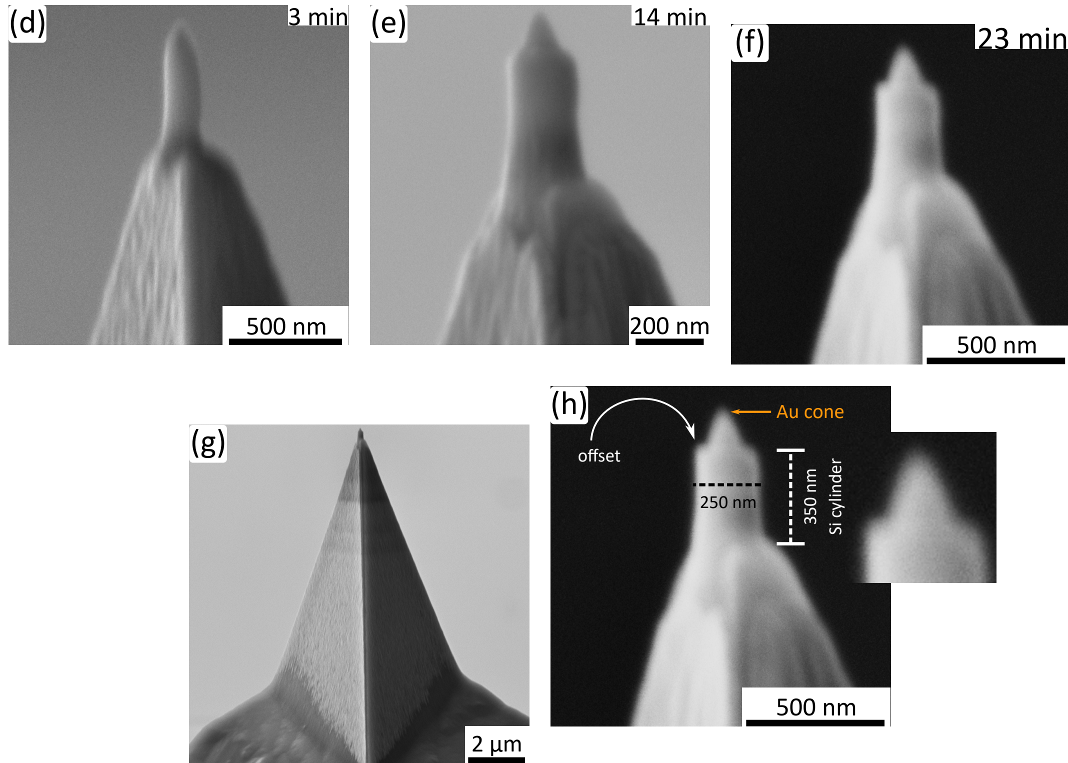

Figure 4.13: The nanocone fabrication process of sample **C**; (a) Coated plateau. (b, c) Top and side view of the Pt pillar. The progress of Pt pillar etching by the Ar^+ milling at (d) 3 min (e) 14 min (f) 23 min (g) Side view of the AFM-C after etching in the Ar^+ milling for 23 minutes, with the metal thin film still remaining on the AFM-C side walls. (h) A gold nanocone with tip radius of 14 ± 3 nm.

There are different factors that make us decide that the gold nanocone fabrication is completed. Firstly, the sharp offset between the nanocone base and the edge of the Si cylinder is probably the boundary between different materials, namely Si and Au. Then, the base diameter of the Si cylinder is more than twice that of the pillar's, which makes a clear distinction that this cylinder is the AFM-C and not the Pt pillar. Further, the dimensions of the nanocone, especially its base diameter is very close to the pillar base diameter, and its height is less than the thickness of the gold thin film which ensure that the hard masks are etched away. Hence, we conclude that more likely the gold nanocone is fabricated after the 23 min Ar^+ milling.

On the other hand, we still suspect that thin films remained on the side walls. It is difficult to completely etch the thin films at the AFM-C pyramid walls since

they are inclined in both x-z and x-y planes which complicates the angular dependency of the Ar^+ milling. But, intuitively they may be considered as a ridge, which is reported to have a significantly slower Ar^+ milling yield compared to the one of the plane surface [116, 126].

		Sample **A**	Sample **B**	Sample **C**
Pt pillar (nm)	Height	77	211	509
	Base	73	105	120
Ar -milling time (min)		2	5	23
Gold nanocone (nm)	Height	94 ± 3	99 ± 8	100 ± 6
	Base	49 ± 3	92 ± 11	159 ± 6
	Tip radius	9 ± 2	11 ± 4	14 ± 3
	Opening angle (°)	49	68	70

Table 4.1: Summary of the Pt pillar dimensions, the corresponding nanocone dimensions, and the associated etching time. The average deviation in the dimensions of Pt pillars and nanocones ranges from ± 3 to ± 8 nm due to the blur in the SEM images.

The dimensions of the hard mask and the resulting nanocones for the samples **A**, **B** and **C** are summarized in Tab. 4.1. The dry etching by the Ar^+ milling was done in time steps ranging from 30 sec to 2 min. Then the sample was examined in the SEM to evaluate whether the hard mask was completely etched or not. As a result, the nanocones have a sharp tip and almost the assigned height of the gold thin film, however the throughput of the process is low and does not permit good reproducibility and control over the dimensions of the nanocones.

FEBID Pt pillar challenges

The nanocone fabrication using a Pt pillar in this work has suffered from different limitations. The pillar height dependency on the exposure time was not very regular, and it is hard to obtain an adequate pillar height. The growth rate

can reach 120 nm/sec as reported in [127]. Accordingly, it was not possible to manually control it precisely within such a short time range ($\leq$ 5 sec). On the other hand, the pillar base diameter was not controlled by the dose, and its dependency on the e-beam dose was not clear. Hence, obtaining both the desired height and diameter with the same e-beam dose using the spot mode was not achievable. Accordingly, depositing Pt pillars with identical dimensions is not often possible. The FEBID also depends on the precursor gas reservoir (heating time) temperature, and the vacuum pressure conditions. The Pt hard mask asymmetry as in Fig. 4.14, and displacement from the center of the plateau as in Fig. 4.14b occurs very often, which can be attributed to the e-beam drift and mechanical hysteresis of the system.

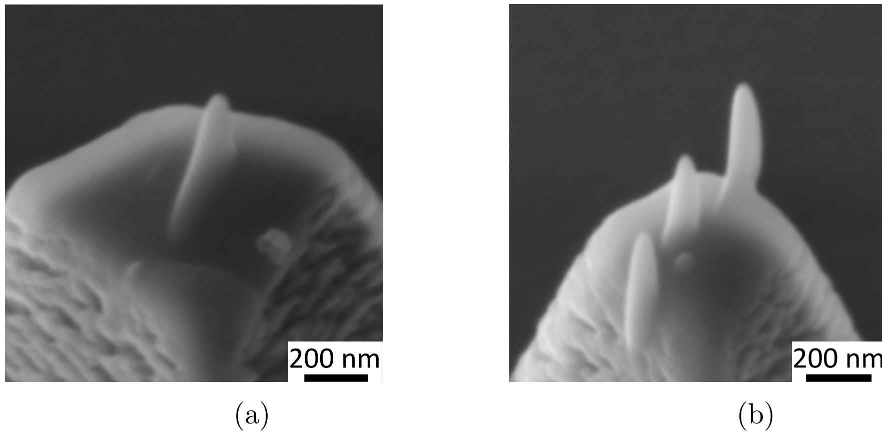

(a) (b)

Figure 4.14: (a) Pt pillar with long tail due to an instability in the FEBID machine. (b) Three Pt pillars were deposited due to incorrect positioning.

Additionally, the Pt pillar deposited by the FEBID usually has a high carbon contamination. These contaminations may release hydrogen and transform from amorphous carbon to graphite [128], which has low etching rate. This transformation can occur after the pillar deposition and during the SEM imaging. Accordingly, its etching rate was not consistent either due to the shape evolution of the pillar and/or the composition of the same pillar may change during the fabrication process. The SEM images did not show a good contrast between the Pt mask and Au, which makes it hard to terminate the Ar^+ milling process exactly after etching the hard masks, to avoid the nanocone overetching.

4.2.2 Nanocone fabricated using a disc milled by FIB

In the following samples, we elaborate the subtractive method to form a hard mask for the Ar^+-milling. This approach is more defined compared to the Pt mask in section 4.2.1, since the height of the mask is the thickness of the oxide film, and its diameter depends on the assigned diameter of the milled shape. We structure a cylinder through the deposited thin film stack as in Fig. 4.15a using the FIB to create a circular hard mask made of the oxide film (SiO_2 or Al_2O_3) on its top. To pattern the hard mask, we utilized the FIB in imaging mode to navigate to the position of the ring milling. Thus, the oxide hard mask is thinned due to the FIB milling during the scanning imaging [123]. Therefore, we deposited a thicker thin film of about 30 nm compared to 15 nm used in section 4.2.1.

The milling process is performed by loading the stream file which contains the coordinates in x,y for all the points which form the ring shape, and the dwell time at each point. Milling was performed at a magnification of 20 kX which corresponds to a pixel size of about 3 nm. The separation between two successive points at OL 50 % corresponds to 5 nm. The FIB current was 16 $\pm$ 3 pA with a beam diameter of about 10 nm and accelerating voltage of 30 kV.

In sample **D** and sample **E**, the milled ring has 180 nm as an inner diameter and 1200 nm as an outer diameter. The ring was milled from a stream file which consists of 31340 points where the dwell time at each point is 10 μsec. The ring was milled in D and E with different milling doses obtained by varying only the number of loops. The milling dose in **D** is 0.4 nC performed by 80 loops which corresponds to 25 sec, while in **E** it is 0.242 nC performed by 50 loops performed in 15.7 sec. The milling dose in **E** is reduced by 0.158 nC compared to **D** to reduce both the overmilling of the cylinder and the milling depth through the thin film stack.

The milled cylindrical pillar is composed of the three thin films (5 nm Ti, 120 nm Au, 30 nm Al_2O_3), where Al_2O_3, the upper film, serves as the hard mask with a disc shape. The milling of a ring shape with 1200 nm outer diameter was critical since the projection of the ring's outer diameter forms conical tips at the intersection between each two sides of the AFM-C pyramid. These sharp edges as in Fig. 4.15b are very close to the gold nanocone.

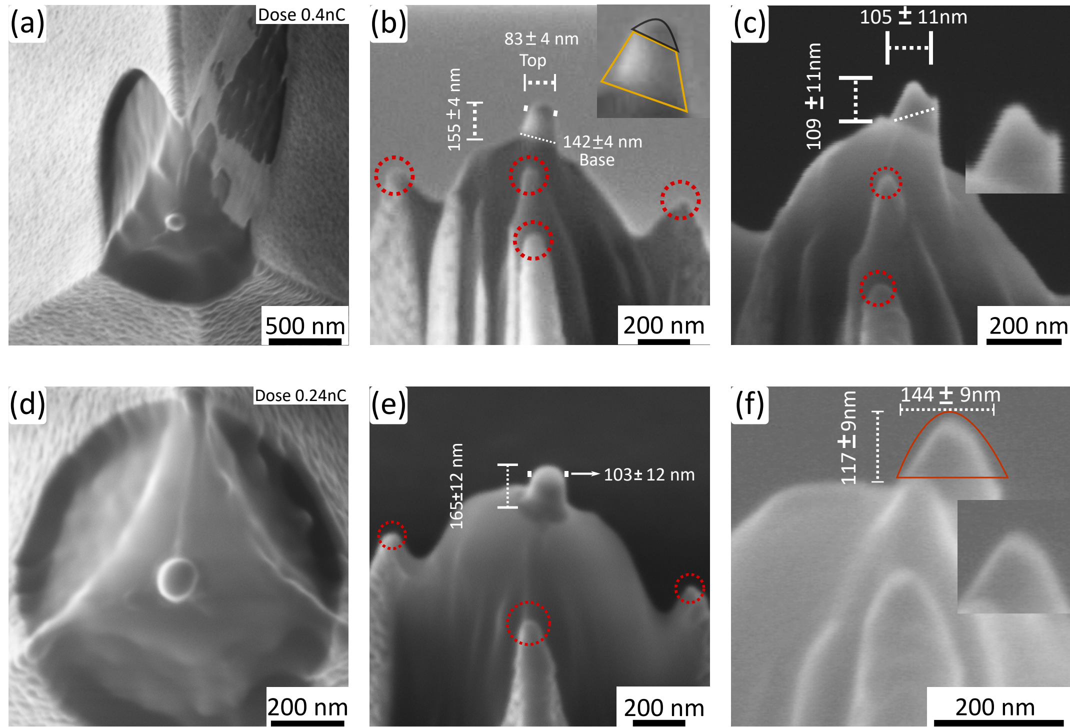

Figure 4.15: SEM images of the nanocone fabrication on samples **D** (a-c) and **E** (d-f), where the milling dose in **E** is lower than in **D**; (a,d) A cylinder formed by milling a ring with nominal inner diameter of 180 nm and outer diameter 1200 nm, and its top is an Al_2O_3 film serving as hard mask; top view to show the milled area by the FIB in the region of the ring pattern). (b,e) Side view shows the cylinder pillar corresponds to the ring inner diameter, and after the milling conical tips (red circles) close to the plateau were formed, due to the inadequately short ring outer diameter. (c,f) A gold nanocone is produced after 2 min 40 sec in the Ar-milling machine

The cylinder in **D** is overmilled more than in **E**. Thus, the cylinder in **D** has almost a trapezoidal profile as in Fig. 4.15b, while in **E** it has almost a rectangular profile as in Fig. 4.15e. Further, the mask diameter in **D** is about 83 ± 4nm and this is smaller than the mask in **E**, which has a diameter of 103 ± 12 nm.

The gold nanocone is produced after etching for 2 min 40 sec in the Ar-milling machine. The nanocone of **D** shown in Fig. 4.15c has a height of 109 ± 11 nm and base diameter of 105 ± 11 nm. Since the deposited gold has 120 nm thickness, the nanocone is overetched by about 11 nm while its base diameter is larger than

the hard mask diameter.

We assume that the optimal ring milling will pattern only a disc from the dielectric film. The milling dose in both samples was higher than the optimal dose. A reduced dose employed in E, produced a pillar with more defined cylindrical profile, and the oxide disc at the top is less overmilled than in D.

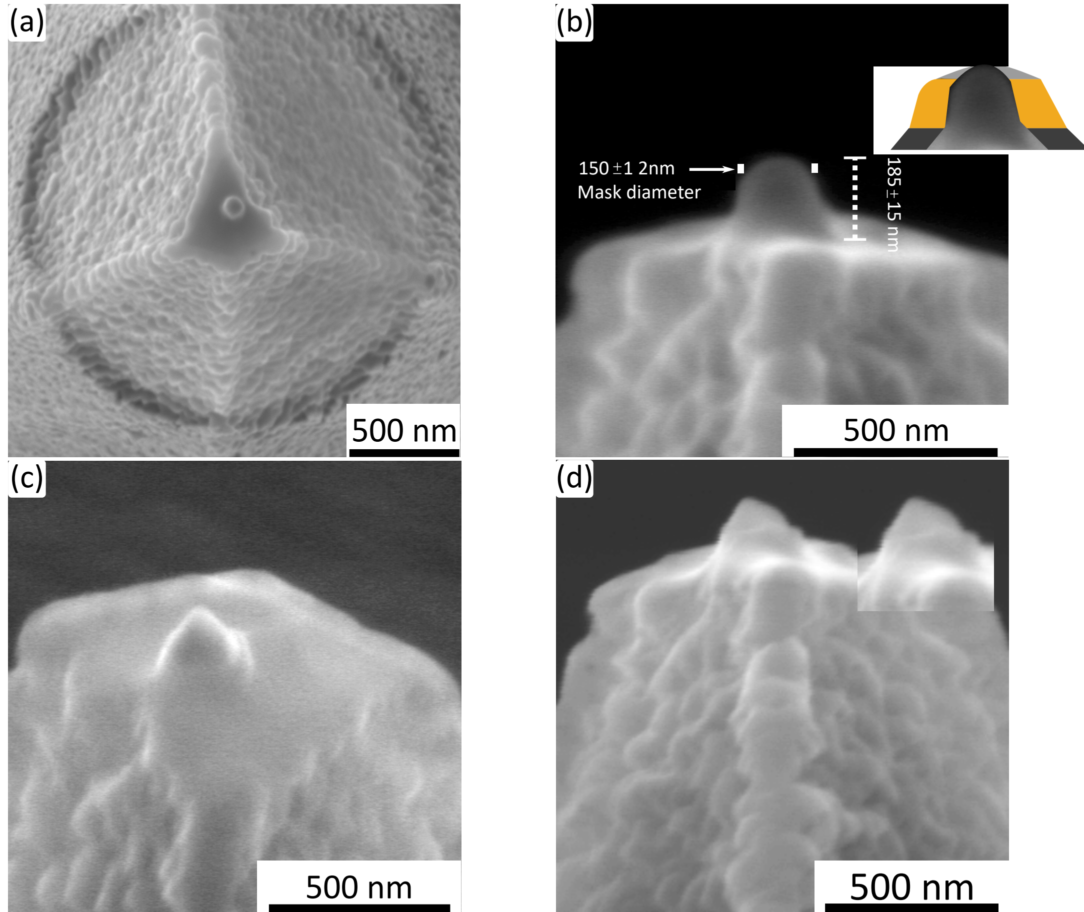

Figure 4.16: SEM images of the nanocone fabrication on sample **F**; (a, b) Cylindrical pillar composed of three thin films. It was milled by Ga^+ FIB. The upper top thin film is the hard mask and it is made of Al_2O_3, where the inset shows each layer material and thickness. (c) After 3 min etching in the Ar-milling machine, the gold nanocone is formed with a tip radius in the order of 33 nm.

With sample **F** we mill, as in Fig. 4.16a, a ring shape using the Ga^+ FIB. It was milled from a pattern file where the outer shell radius and inner core radius were equal to 2 μm and 300 nm, respectively. The milling dose in **F** is about 0.32

nC by having a total milling time of about 20 sec, where the dwell time was 30 μsec and overlap is 0 %. After dry etching with Ar^+ for 3 min, the pillar in Fig. 4.16b is shaped into a gold nanocone. This nanocone has a tip radius equal to 33 nm. Accordingly, the nanocone is overetched.

		Sample **D**	Sample **E**	Sample **F**
Milled Cylinder (nm)	Height	155 ± 4	165 ± 12	185 ± 15
	Top	83 ± 4	103 ± 12	150 ± 12
Ar -milling time (min)		2.6	2.6	3
Gold nanocone (nm)	Height	109 ± 11	117 ± 9	103± 5
	Base	105 ± 11	144 ± 9	119 ± 5
	Tip radius	20 ± 2	27 ± 5	33± 2
	Opening angle (°)	55	85	70

Table 4.2: The dimensions of the hard mask milled by FIB, and the fabricated nanocones.

To calculate the adequate ion dose for milling a cylinder in SiO_2 with 30 nm in height and the same circular cross section area as in **E**-**F**, we consider the sputter yield of SiO_2 in section 4.1.2. Accordingly, the adequate ion dose is 0.12 nC which is significantly lower than the doses used in **E**-**F**, and is consistent with the overmilling of the ring.

Another important parameter in the milling dose calculation is that the plateau and the AFM-C sidewalls have different milling angles. The plateau one is about 0°, while the AFM-C sidewalls one is about 60°, and thus they have different sputter rates. Milling the ring pattern with the same dose will produce unexpected deformations in the mask geometry and dimensions. One way to circumvent this is to divide the ring shell into two parts: the inner shell is milled on the plateau with the dose calculated using the sputter yield of milling in the plane surface, and the outer shell is milled on the AFM-C pyramid side walls by the corrected dose for the sidewalls inclination angle. The nanocones fabricated

by only patterning a disc shape from the deposited thin film stack shows a good reproducibility and throughput. On the other hand, their tip radius is larger than the nanocones radius in section 4.2.1. According to [67] the nanocone tip radius and the opening angle can be tuned by the hard mask thickness and material.

4.3 Simulations of the nanocones scattering

We performed 3D FDTD-simulations using the Lumerical commercial software package to calculate the scattering spectrum of nanocones with the same dimensions as the fabricated ones but embedded in air. Hence, we can obtain a closer insight to the LSPR tip mode of the fabricated nanocones in this chapter, which is the relevant mode for the SNOM/TERS measurements. We used a plane wave source with an electric field parallel to the cone long axis, and mesh size of 3 nm, where the perfect matching layers are the boundary conditions.

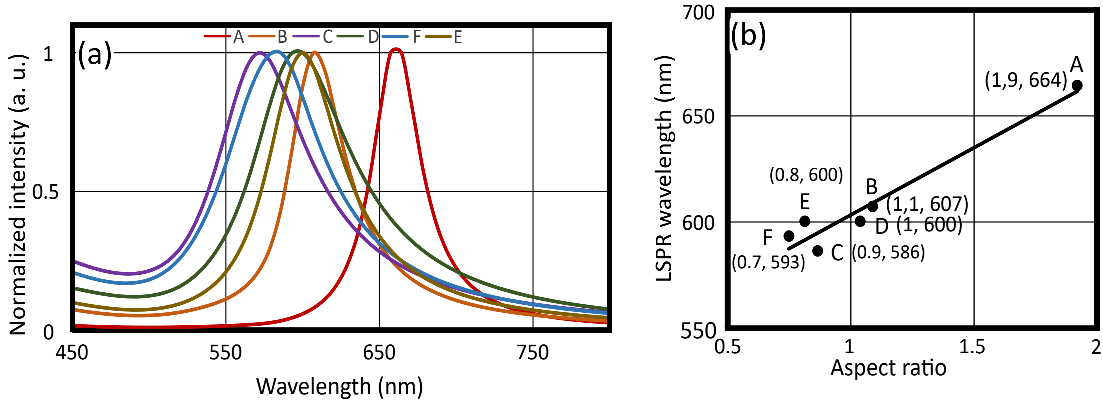

Figure 4.17: (a) The scattering of the nanocones of samples **A**-**E** calculated by 3D FDTD simulations using the Lumerical commercial software. (b) The LSPR wavelengths of the nanocones dependence on the nanocone aspect ratio which is similar to the results in [61].

The calculated scattering in Fig. 4.17a, shows that the LSPR of nanocones in air ranges from 586 nm to 664 nm, which will be red shifted by the higher refractive indices of the substrates [61, 129]. The LSPR tip mode shows a strong dependency on aspect ratio which is the ratio of the height to the base diameter, and this shows good agreement with the results reported in [61]. By finding the LSPR, it is possible to define the light source wavelength to excite cone LSPR, and the wavelength range of the higher near field enhancement for the measurement.

Further, the LSPR dependency on the aspect ratio shows the tunability of the LSPR as well as the importance of well controlling the cone dimension during the fabrication process to well define the LSPR wavelength.

4.4 Conclusion

We introduced the fabrication process of gold nanocones on top of AFM-Cs, where two methods have been optimized to form the hard mask. From the optimization experiments, we find an empirical relation that defines the milling section of the AFM-C in a way to match the plateau width with the nanocone base diameter and thus to avoid having an excess vacant area in the plateau, which may shield the plasmonic nanocone during the SNOM measurements.

Then, we deposit different pillars using e-beam dose ranges from 630 to 2070 nC to find the Pt pillar growth rate and the possibility to control its base diameter. The growth rate was 252 $\pm$ 92 nm/nC, but controlling the base diameter with e-beam dose was not possible.

As the final part in the optimization, we find the sputter yield of SiO_2 from which the optimal milling dose should be calculated to control the ring FIB milling.

The first method to fabricate the nanocone is by employing a hard mask composed of a Pt pillar and an underneath dielectric film. Then, during the dry etching of the pillar, a circular disc made of the dielectric film is formed. Finally, the gold nanocone is produced after etching both masks in the Ar-milling machine. Further, the dielectric film protects the gold ones during sample transport and processing, and it may show a contrast between the Pt and Au in the SEM images to deduce the progress of dry etching. Nanocones were produced successfully by using the Pt pillar. However, this method suffers from different limitations.

Pt pillar dimensions vs Dose

By employing the spot mode in the FEBID deposition, it is hard to define a single dose for the e-beam to control both the pillar height and diameter. The dependency of the pillar base diameter on the dose is not clear, and it more depends on the voltage.

Pt pillar positioning

The pillar was very often misplaced, which required to deposit more than one pillar to obtain a more centric one. Thus, the plateau may have more than one

nanocone on its top and it is not any more a SNOM probe with a single tip.

Pt pillar symmetry

The asymmetric pillar can be deposited due to vibrations or may result from the mechanical hysteresis of the machine and/or unexpected e-beam drift during the deposition. Consequently, this will lead to a deformed nanocone shifting its plasmon resonance from the assigned one.

Pt pillar milling rate

From a theoretical point of view, the contaminations are not the same in the deposited pillars and the hydrocarbon may dissociate into graphite during the SEM imaging. Further, the pillar shape evolves as in sample **C**. Thus, theoretically it is hard to know the rate of the FEBID deposited Pt pillar.

Since the milling rate is not constant, the dry etching step was split into short intervals and in between the sample was examined in the SEM to define if the nanocone is fabricated or not. Therefore, the total fabrication time is much longer than the one of the method based on the hard mask patterned by the subtractive method.

The second method is FIB milling through the deposited thin films to obtain a cylindrical pillar, which shows a higher throughput and a better reproducibility of the gold nanocone as a SNOM probe.

Milling a circular disc made from only oxide film demands a very well optimized dose, which should be calculated from the sputter yield of the mask material. The different milling angles of the plateau and sidewalls should be considered in calculating the dose, which results in two ring patterns with at least two different doses depending on the angle.

The outer radius of the ring should be adequately large to avoid the formation of sharp tips located close to the nanocone, which may disturb the SNOM measurement. Further, in the same step of milling the ring the residual films on the sidewalls can be etched in a depth defined by the ring outer radius. The AFM-C pyramid can be reshaped to ensure an optical access to the nanocone in order to have a better SNOM performance. Further, this method permits to fabricate more advanced geometric shapes such as interlaced rings, ellipses, crescents and stars.

By intuitively comparing the tip radius and the opening angle of the nanocone produced by the Pt pillar method, we found that they are smaller than the ones of the nanocones produced by only the oxide disc. Hence, using a hybrid mask

made of two materials with different milling rates such as Pt pillar and oxide film may permit to tune the tip radius and the opening angle of the nanocone. The sharpness of the tip has a crucial role in the spatial resolution of the SNOM measurement, while the opening angle plays a role in the field enhancement [130]. The technique of patterning a hard mask with FIB can be applied to fabricate nanostructures with a variety of geometries on a non-planar substrate. Further, the fabricated nanostructure probably has little Ga^+ contamination, since the Ar^+ will etch away most of the layers, which may have Ga^+ within it.

Outlook

The deposition of a Pt pillar using a scanned beam controlled by a stream file may show better results than the deposition in a spot mode.

Enhancing the quality of the gold nanocone SNOM probe by etching the residual thin films at the side walls, either by tilting it with an angle which ensures selective etching in Ar^+ milling of the side wall and shielding the nanocone, or by optimizing the FIB ring milling where the side walls are cleaned and the hard mask pattering is achieved simultaneously.

The AFM-C pyramid can be modified by micro-machining a few microns close to the nanocone into a cylindrical pillar in order to obtain a good optical access for illumination and signal detection during SNOM measurements. The durability of the nanocone can be improved by coating it with a few nanometers of Al_2O_3 [40].

Chapter 5

Nanocone fabrication on top of optical fiber

The next proposed design of the SNOM probe is constructed from a tapered multimode and/or single mode optical fiber with a plasmonic nanocone as its probe. It is interesting to fabricate a nanocone on top of an optical fiber to be suitable for SNOM instruments which employ the STM feedback mechanism. Further, it permits to perform the SNOM measurements in different illumination and detection configurations either in free space or by coupling signals in and out of the optical fiber.

Besides fabricating a single nanocone on top of the fiber, it is important to boost the overall quality of this probe by suppressing the imperfections of the fabrication process. Some of these imperfections arise from the rough surface of the tapered fibers which is created often after chemically etching the fibers. After the nanocone fabrication is completed these rough walls will still be coated with the residual metal thin films. Hence, they can be sources of background noise signals for the SNOM measurements stemming from unwanted light reflections and scattering signals from these metal coated rough walls. Accordingly, it is necessary to reduce both the roughness of the tapered fiber and the thickness of the residual metal thin films to obtain high-quality SNOM probes.

In this chapter, we discuss the optimization of the fiber chemical etching to improve the fiber morphology and to control the tapered cone geometry in terms of its tip radius and opening angle, followed by presenting the successful plasmonic nanocone fabrication on top of T-OFs.

In the last section, we discuss the fabrication of the nanocone on top of an optical fiber with a length of a few meters, in order to couple the laser through the fiber to excite the nanocone plasmonic resonance. These fibers are single mode

fibers, and were tapered by David Auwärter * using the heat and pull method. Finally, we demonstrate the possibility to apply the shadow method to fabricate the nanocone on top of the optical fiber.

Further, we show the 3D FDTD simulation of the scattering spectrum of the nanocones to get more theoretical perception of their optical properties.

5.1 Fabrication process

In our work, the main purpose is to use the multimode optical fiber in the free propagating mode for the probe illumination, and the sample signal detection. The diameter of the multimode fiber is 125 μm which is about a thousand times greater than the nanocone base diameter. Hence, it is necessary to transform it into a sharp pointed tapered fiber with a diameter in the sub-micron scale in order to grant optical access to the nanocone during optical measurements. The T-OF cone angle is relevant to the mode of the SNOM and/or TERS measurements. In the free propagating mode the T-OF cone angle addresses the slope of the tapered tip walls, thus the smaller angle allows for a better illuminating of the nanocone probe and detection of the signals from the sample. In contrast, with the coupling light mode, the cone angle addresses the cutoff wavelength, where at a wider tapered cone angle the distance between the cutoff fiber core diameter and the aperture is shorter [131]. Thus, the wide tapered angle (i.e. optimum angle ranges between 30° to 50°) permits higher transmission [132] and more signal coupled in and out the T-OF, which is preferable in the measurement setup equipped with illumination and/or collection through the T-OF setting.

In the fabrication aspect, the fiber tapering is essential in order to easily map the site of the nanocone on top of the fiber to monitor the progress of the fabrication process along its successive separate steps. The optical fibers were tapered by chemical etching, where we endeavor to have T-OFs with a small cone angle and tip radius. The T-OF small cone angle permits to adequately match the plateau diameter with the nanocone base diameter. Additionally, during the evaporation step, the thickness of the thin films at the T-OFs side walls with a very acute angle will be thinner compared to the wide cone angle. Since the thickness of the evaporated thin films is proportional to the cosine of the angle (θ; $\theta = 90° - 0.5 \times$ cone angle) in eq. 2.4 which lies between the norm of the fiber walls and the evaporated material beam, e.g. at infinitesimally small cone angle the θ approaches 90°, thus almost no film will be deposited on the fiber walls.

* Physikalisches Institut and Center for Collective Quantum Phenomena in LISA+

The main obstacle with the fiber chemical etching is the roughness, which can produce a strong background signal by reflecting and scattering the light in the interaction vicinity between the gold nanocone probe and the surface of the sample. In this section, we discuss the different techniques in fiber chemical etching to improve the quality of the tapered fiber and control its tip radius and cone angle.

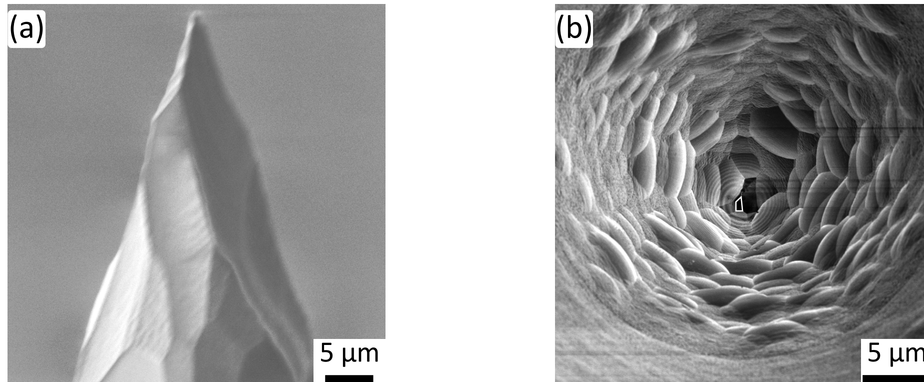

Figure 5.1: A tapered fiber with cone angle of about 42° and a rough surface tip after being etched only in HF (49%), which can be a source of unwanted light reflections and scattering during the SNOM measurements. (a) side view without coating, (b) top view after coating with thin films stack.

The morphology smoothness can be improved by different methods such as using a buffered etchant solution with NH_4F (BHF), or the tube etching method where the fiber is kept inside a coating made of material resistive to HF such as polymer or acrylate, thus the HF can etch the fiber only through the coat front opening [119, 133]. The etch rate for the tube method and BHF is very slow. Further, in the tube method it is very critical after etching the fiber is completed to remove the plastic coat without breaking the tapered tip. The geometry of the T-OF such as the taper length and taper cone opening angle, can be controlled either by choosing the organic solvent material or the dynamic etching method where the fiber is kept in a vertical motion during the etching, see the detailed discussion in section 2.1. Tuning the opening angle by choosing an organic solvent is not a clear method and we must consider the viscosity and melting point of some organic solvents to avoid the organic solvents to stick to the wall of the fiber, or formation of small crystals at room temperature which may damage the T-OF fine tip.

Accordingly to obtain T-OFs with acceptable smoothness and tune their tip opening angle, we choose an intuitive approach by combining the buffered etchant

and dynamic etching method in the same step. Thus, the fibers are immersed as it is mentioned in Tab. 5.1 firstly in solution that contains only HF (40%) (Sol.1) for a time range from 14 to 19 minutes, in which most of the fiber cladding was etched. Then, the fibers are immersed in the buffered etching solution consisting of HF (40%) : NH_4F : H_2O (Sol.2) with a ratio 1:2:2 for a time range between 38 to 62.7 minutes. The fibers were pulled up in 2 discrete steps within the solution during the etching in Sol.2 which leads as in Fig. 5.2c to two discrete tapered regions. The semi dynamic etching in Sol.2 is as follows; in sample **S** the fiber was etched statically for 31 min, then moved up and etched statically for 12 min to form the tip, while in sample **T** the fiber was etched statically for 12 min, then moved up and etched statically for 26 min to form the tip. The etch rate in Sol.1 and Sol.2 is 3.44 $\pm$0.31 μm/min and 1.53 $\pm$ 0.11 μm/min, respectively. The tapered tip was formed in Sol.2 at a meniscus average vertical speed equal to 4.8 $\pm$ 0.34 μm/min for sample **S** and equal to 3.74 $\pm$ 0.26 μm/min for sample **T**.

Samples	Etching Time (min)		Tip radius (nm)	Cone angle (°)
	Sol.1	Sol.2		
Sample **R**	14	63	164	26
Sample **S**	18	43	121	28
Sample **T**	19	38	64	21

Table 5.1: The optical fibers were etched in two different solutions; Sol.1 contains HF (40%) and Sol.2 is BHF where HF (40%) : NH_4F : H_2O are with the ratio 1:2:2. The etching method combined the static mode and manually controlled upward motion of the fiber. As a result the morphology of the tapered fibers is improved and the radius and the opening angle can be tuned according to the favorable values.

In the dynamic etching, a section of the fiber is tapered for a specific time, then the fiber is drawn up where another section gets tapered, where these steps' frequency and the termination of the etching are defined by the required sharpness of the tip radius and opening angle. The etched fibers are depicted in Fig. 5.2, we see in the same fiber two separated tapered regions due to the manually controlled dynamic etching for two different sections in two distinct steps. The three fibers morphologies have similar smoothness. Further, it allows to tune the opening angle and produce a smaller angle compared to the cone angle formed

by statically etching in HF (49%) which is consistent with [85].

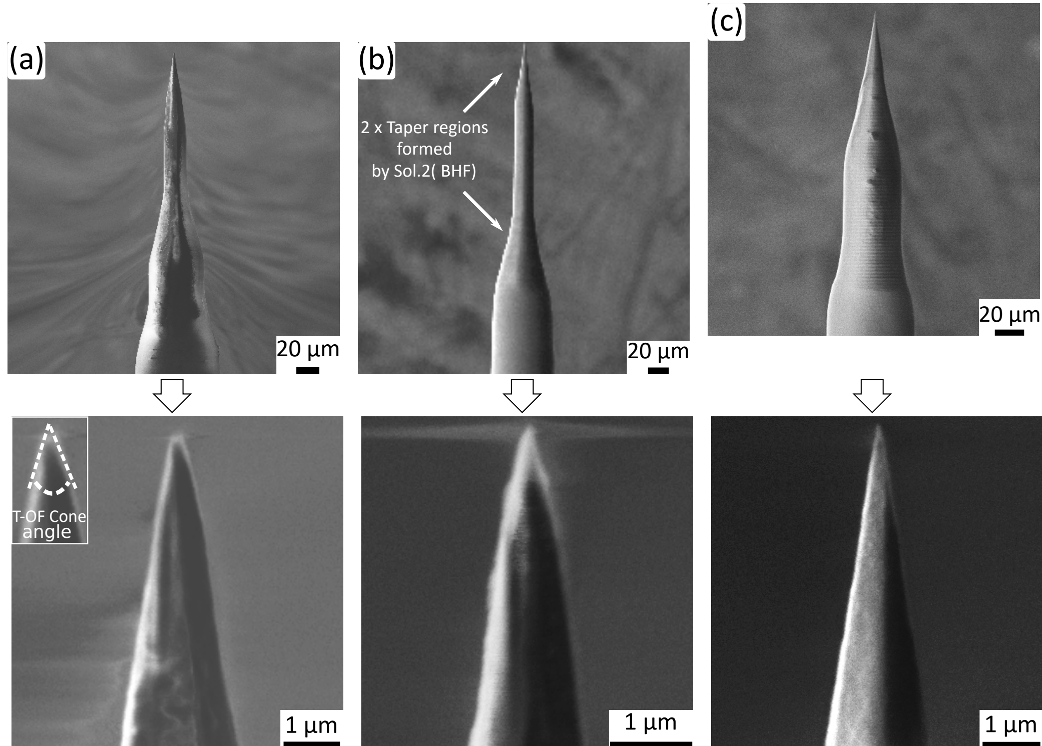

Figure 5.2: We etched the fiber using a semi dynamic method firstly in only HF (40%), and then in buffered solution containing HF (40%) : NH_4F : H_2O with the ratio 1:2:2. The fibers are etched in (a) Sample **R** for 14 min in Sol.1, and then 63 min in Sol.2. (b) Sample **S** for 18 min in Sol.1, and then 43 min in Sol.2. The two tapered regions are etched by Sol.2. (c) Sample **T** for 19 min in Sol.1, and then 38 min in Sol.2.

In the next section, we apply a manually frequent withdrawing motion in sample **N**, which produces an opening angle as ultimately small as less than 10°. The etching rate in the buffered solution is very slow, thus the throughput can be enhanced by etching more fibers in parallel.

5.2 Results and Discussion

The fabrication process of a nanocone on top of a tapered optical fiber (T-OF) as it was delineated in chapter 3 follows this sequence: we start by chemical wet

etching of an optical fiber, then adapt it to be the substrate by milling its tip apex using the focused ion beam (FIB), then coat it with the thin films stack, followed by depositing the hard mask and finally apply the Ar-ion milling to transform the hard mask and the gold film underneath into a plasmonic nanocone to be a SNOM probe.

The results will be divided into two parts, one for the multimode fibers which were etched chemically, and the second for the single mode fibers which have a length of few meters and were tapered by David Auwärter* using the pull and heat method. It was difficult to characterize the samples using the dark field microscopy, since the scattering signals from the residual thin films and rough fiber walls were stronger than the scattering signals from a single nanocone. Accordingly, the progress of the probes fabrication process is characterized at each stage by scanning electron microscopy, as explained in chapter 4, where the SEM image shows when the nanocone is fabricated, and gives the nanocone dimensions and symmetry, further it shows the overall geometric quality of the SNOM probe such as potential residual thin films and the roughness of the walls.

5.2.1 Nanocone on top of multimode optical fiber

The samples in this section are multimode fibers with a total length of about 6 cm, where 3 cm are bared from the plastic coat as in Appendix A.3 using the H_2SO_4. They are proposed for the SNOM measurements in the free space probe illumination and signal detection mode.

*Physikalisches Institut and Center for Collective Quantum Phenomena in LISA$^+$

Sample	Tip radius (nm)	Opening angle (°)	Thin film thickness (nm)		
			Ti	Au	Al_2O_3
Sample **K**	207 ± 20	54	5	120	15
Sample **L**	328 ± 27	44	5	120	15
Sample **M**	89 ± 6	29	5	150	15
Sample **N**	95	< 10	5	130	30

Table 5.2: The samples **K-N** T-OF tip radius, opening angle and the thickness of the deposited thin films. They are multimode fibers and were tapered chemically in HF containing solutions.

For the following samples (**K** - **N**), we summarized in Tab. 5.2 their etched fiber tip radius and opening angle, and the thickness of the deposited thin films.

The nanocone fabrication for sample **K** is delineated by the SEM micrographs in Fig. 5.3, where the T-OF was etched in only HF (49%) statically for 27 minutes. It has a tip radius of about 207 ± 20 nm, which is not sharp. Consequently, after cutting its apex the formed plateau has a radius approximately equal to 440 nm. Then, the deposited thin films on top of the plateau as shown in Fig. 5.3b have an adequately homogeneous and smooth morphology. The hard mask was a Pt pillar and was deposited using the FEBID. The Pt pillar has an asymmetric shape with two tips, and a height and base diameter of about 170 nm and 155, respectively as listed in Tab. 5.3. Hence, after etching the mask in the Ar-milling machine we obtained a gold nanocone as in Fig. 5.3e with two very sharp tips. The etching time was 4 min and the fabricated nanocone dimensions are listed in Tab. 5.3. The plasmonic gold nanocone's two very sharp tips each have an apex radius equal to 8 ± 3 nm and are formed after 4 min dry etching in the Ar^+ milling machine. In order to find whether the nanocone is overetched or not, we compare the nanocone height and the deposited gold thin film thickness.

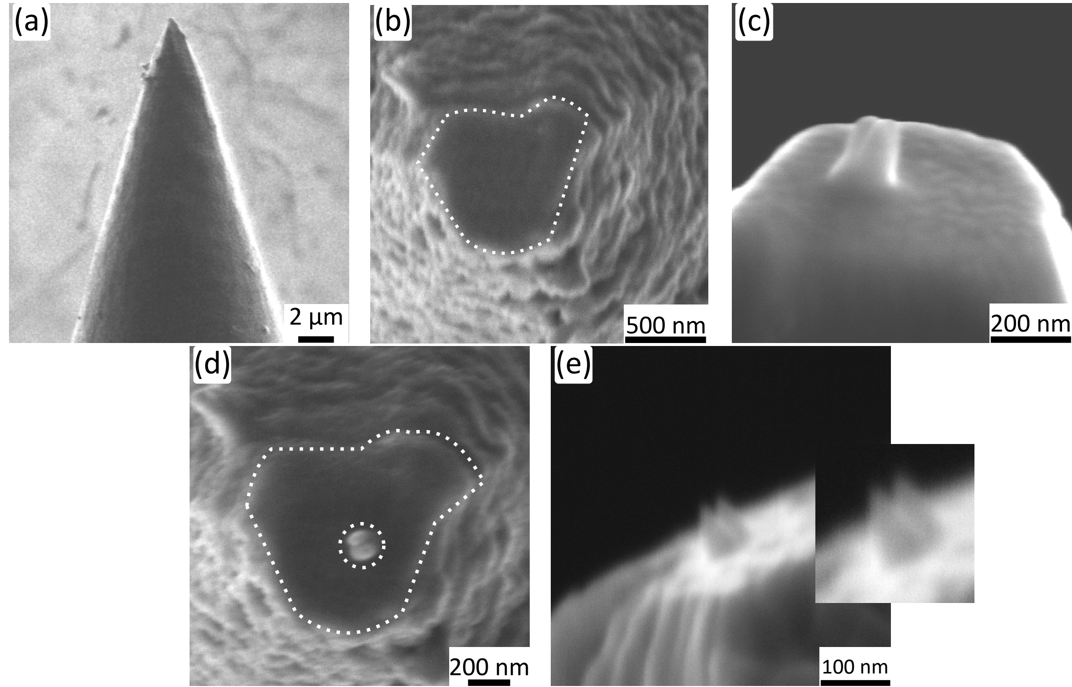

Figure 5.3: Sample **K** SEM image of each step; (a) Sample **K** with a tapered tip with apex radius 207 ± 20 nm. (b) The plateau with radius of 440 nm is coated homogeneously, after the evaporation deposition step. (c, d) Pt pillar with two heads, and a height of 170 nm was deposited by FEBID. (e) After 4 min dry etching in Ar-milling, a gold nanocone is shaped with two heads and each sharp tip has a radius of 8 ± 3 nm.

The nanocone height is 76 ± 3 nm as in Fig. 5.3, while the deposited gold thickness was about 120 nm from Tab. 5.2. Although the nanocone is overetched by about 44 ± 3 nm, it owns very sharp tips.

The optical fibers in the next two samples **L** and **M** were etched in a semi-dynamic way in only HF solution with 49%. Thus during the chemical etching, the fibers were withdrawn upwards forming more than one taper region, in order to enhance their morphology and tune their opening angle. Hence, they are as shown in Fig. 5.4a and Fig. 5.5a adequately smooth, and their opening angle is smaller than the one produced by static etching in HF.

In sample **L** the total etching time of the fiber is about 27 min, and the T-OF tip as in Fig. 5.4 has a radius of 328 ± 27 nm. The T-OF is noticeably overetched, but still sufficient for the nanocone fabrication. After milling its apex, we obtained a plateau with a trapezoid geometry. It was coated by a thin films

stack with the thickness as listed in Tab. 5.2. The thin films stack from Fig. 5.4b is homogeneously covering the plateau and the T-OF walls. The hard mask is deposited using a voltage of 9 ± 1 kV, where the e-beam is 110 ± 10 pA focused in spot mode for an exposure time 4 ± 1 sec. During the FEBID step two hard masks were deposited as in Fig. 5.4d to obtain a more centered pillar, since the first pillar was misplaced at the edge of the plateau. Finally, a single plasmonic nanocone is structured as depicted in Fig. 5.4e after etching for 2 min inside the Ar-milling. The plasmonic cone has a tip radius of 18 ± 5 nm and height 59 ± 5 nm, it is overetched by 61 ± 5 nm.

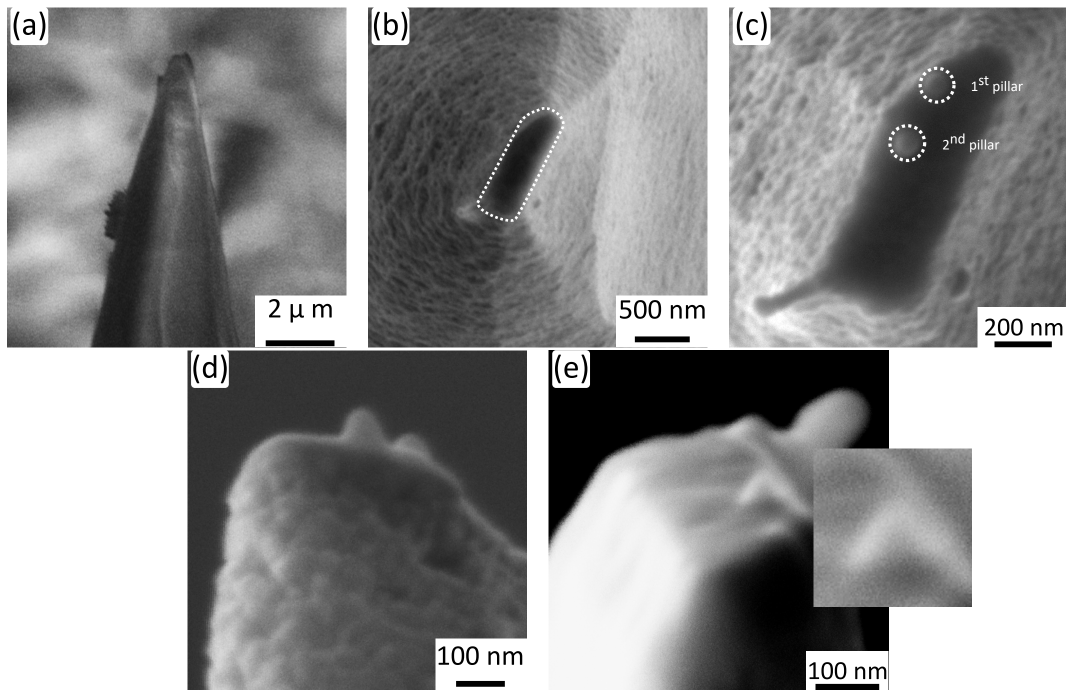

Figure 5.4: The nanocone fabrication on top of the T-OF in sample **L**. (a) T-OF etched in HF (49 %) for about 27 min, it shows an overetched tip. (b) A plateau formed by using the FIB to mill the T-OF tip. Two Pt pillars were deposited by FEBID, since the first pillar was misplaced near the edge of the plateau ; (c) Top view, (d) Side view. (e) The gold nanocone fabricated after 2 min dry etching, it has a tip radius of about 18 ± 5 nm.

The T-OF in sample **M** has a tapered tip with a radius of 89 ± 6 nm as shown in Fig. 5.5a, after etching the fiber for about 25 minutes. The plateau formed after milling the T-OF apex has a rectangular shape with a long and short side equal to about 560 nm and 240 nm respectively. It was coated as in Fig. 5.5b

with the thin films with the thickness as listed in Tab. 5.2. The deposited Pt hard mask has a conical shape with a height and base diameter equal to 29 and 114 nm, respectively. It was deposited using FEBID with the electron beam focused in a spot mode. The e-beam exposure time was about 4 ± 1 seconds, and the e-beam current and the accelerating voltage are 30 pA and 8 kV respectively.

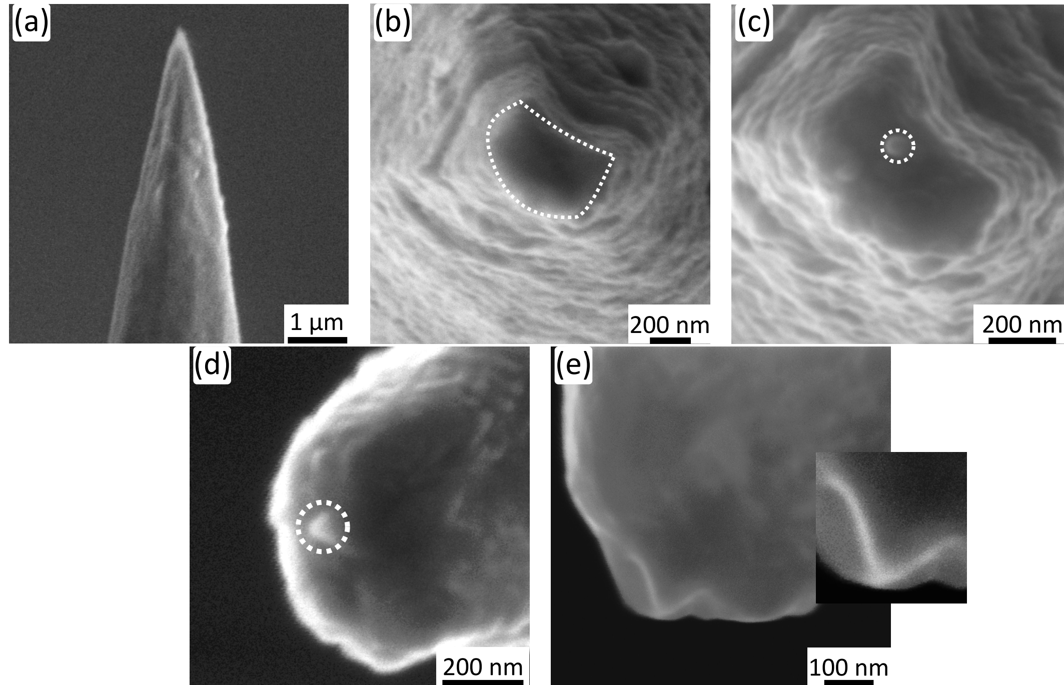

Figure 5.5: Sample **M** SEM images of each step; (a) A sharp T-OF with a tip apex radius of 80 nm. (b) The plateau has a rectangular geometry, and it is homogeneously coated with three thin films. (c, d) The deposited Pt hard mask has a conical shape, and its height is 29 nm. (e) Gold nanocone was shaped after 3.5 min dry etching in Ar-milling.

A nanocone with a tip radius equal to 24 ± 4 nm was shaped after 3.5 min total etching time in the Ar-milling. The nanocone height and base diameter are about 113 ± 4 nm and 159 ± 4 nm, respectively. By comparing the deposited thickness with the fabricated nanocone height as is listed in Tab. 5.2, the nanocone is overetched by 37 ± 4 nm but still its tip radius is sharper than 25 nm.

Sample **N** is the last sample in the multimode fiber section. In sample **N**, the fiber was etched using the method described in section 5.1 where the fiber was firstly etched in HF (49%) for about 20 minutes, then dipped in buffered solution that contains HF : NH_4F : H_2O with a ratio of 1:2:2 for about 36 minutes. During

the etching in the second solution which has a very slow etch rate the fiber was frequently manually withdrawn upwards.

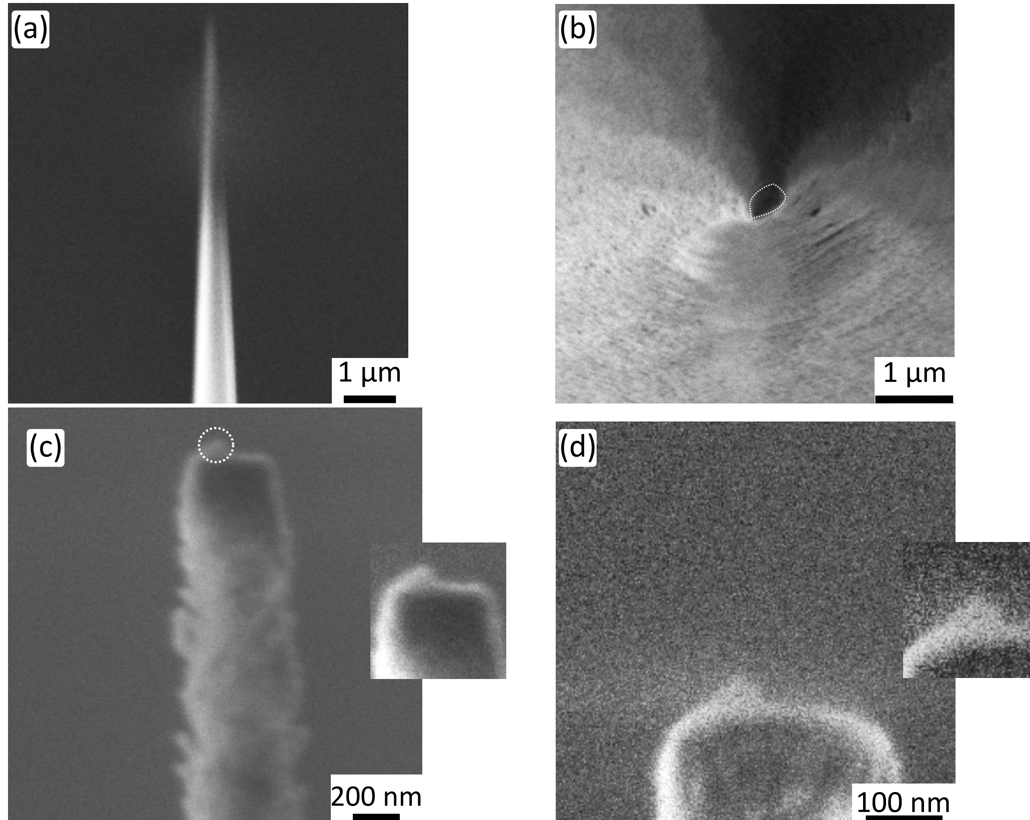

Figure 5.6: The SEM images of the nanocone fabrication in sample **N**, (a) A sharp T-OF with opening angle less than 10°, it was tapered by combining the dynamic method and the buffered HF solution. (b) T-OF with a homogeneously coated plateau. (c) The FEBID deposited Pt as a hard mask on top of the thin film stack. (d) Plasmonic cone with tip radius 14 nm, shaped after applying Ar-milling for 4 min total milling time.

Consequently, we obtained a smooth tapered fiber with a very small opening angle $< 10°$ as shown in Fig. 5.6a, and its tapered tip walls are continuous and have almost the same slope. In Fig. 5.6b, we see a homogeneously coated plateau with almost an elliptical shape obtained after milling the T-OF apex in the FIB and followed by the thin film deposition. Finally, a gold nanocone as shown in Fig. 5.6d was fabricated after milling the Pt pillar in Fig. 5.6c. Here, the gold nanocone is obviously overetched by at least 75 nm, which is consistent with its

wide opening angle and a blunt tip compared to the nanocones in the samples **K** and **L**. On the other side, the thin films deposited at the tapered tip side walls were very thin owing to the T-OF tip very small opening angle. Hence, the strong charging effect in Fig. 5.6d indicates that in sample **N** the thin films at the tapered tip walls were noticeably etched away.

		K	**L**	**M**	**N**
Pt pillar (nm)	Height	170	68	29	78
	Base	155	78	114	116
Ar -milling time (min)		4	2	3.5	4
Gold nanocone (nm)	Height	76	59	113	50
	Base	59	92	159	106
	Tip radius	8	18	24	14
Error (nm)		± 3	± 5	± 4	± 2
	Opening angle (°)	55	75	70	95

Table 5.3: Summary of the multimode fiber samples (**K**-**N**) Pt hard mask height and base diameter, the Ar-milling time and the fabricated gold nanocone dimensions. The average deviation in the nanocone dimensions are due to the SEM image blur.

5.2.2 Nanocone on top of single mode optical fiber

We fabricated nanocones on top of single mode fibers, which were tapered using the heat and pull method. They have a length of a few meters such that the nanocone plasmonic resonance can be excited by the coupled light in the fibers. Further, they have a smooth morphology and small opening angle compared to the ones of the chemically tapered fibers. We listed in Tab. 5.4 their tip radius, opening angle, and the thickness of the afterward deposited film on the plateau. We will discuss the nanocone fabrication using the Pt pillar in samples **O** and **P**, and using the circular disc milled by FIB in samples **Q** and **U**. Then, we discuss the possibility to have a nanocone on top of the T-OF using a shadow mask method in sample **V**, which is different from the hard mask etching method.

There are two main challenges with heat and pull fibers. Firstly, they are mechanically unstable, and often during the fabrication the fiber tip bent. Hence, it can be difficult to align precisely the fiber during the fabrication steps. Secondly, after starting the Ar^+ milling step they possess strong electrostatic charges, since the residual thin films etched away similar to the case of sample **N**.

Sample	Tip radius	Opening angle	Thin film thickness (nm)		
	(nm)	(°)	Ti	Au	Al_2O_3
O	170 ± 10	18	5	120	15
P	68 ± 4	22	5	120	15
					SiO_2
Q	-	-	5	160	60
U	-	-	5	160	60

Table 5.4: Table of samples **O**-**U** tip radius, opening angle, and the deposited thin films thickness. These fibers are single mode and were tapered by David Auwärter using the pull and heat method.

Hence, it turns hard to monitor the progress of etching the hard mask using the SEM. Further, these electrostatic charges attract particles that are attached to the fibers, which are hard to remove, and they can destroy the probe. These new challenges demand additional efforts to fabricate a nanocone on such heat and pull tapered fibers with high quality and in a good reproducibility and throughput approach, which are suggested in the outlook section.

For sample **O**, the nanocone fabrication process is delineated in Fig. 5.7. The T-OF in Fig. 5.7a was tapered by heat and pull method, and has a smooth morphology. The plateau has a circular cross-section formed after milling the tip by the FIB. Then, the plateau is homogeneously coated as in Fig. 5.7b with 5 nm Ti, and on its top gold and Al_2O_3 with a thickness of about 120 nm and 15 nm, respectively. In the Pt pillar deposition by FEBID, the pillar was misplaced as in Fig. 5.7c,d at the edge of the plateau. The pillar has a height and base

diameter of 265 ± 15 nm and 144 ± 15 nm, respectively.

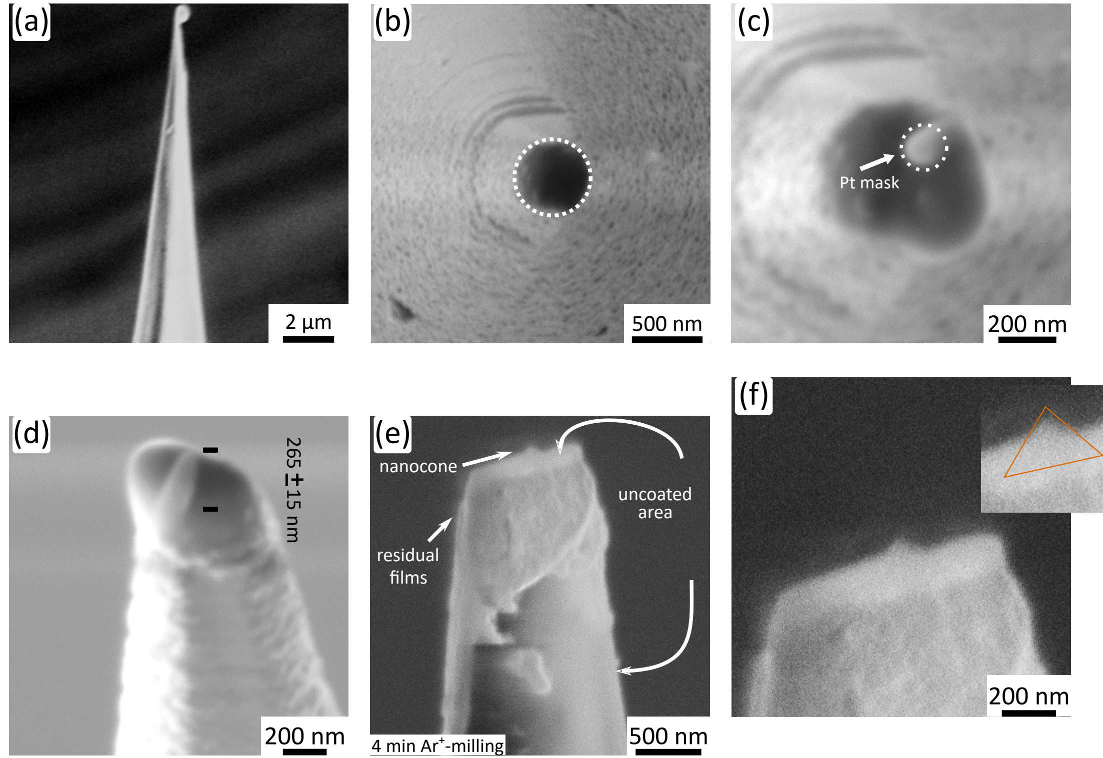

Figure 5.7: Sample **O** (a) T-OF tapered by the pull and heat method. (b) A plateau with symmetric circular geometry. The Pt pillar deposited by FEBID was misplaced at the edge of the plateau; (c) Top view, (d) Side view. (e) After Ar-milling for 4 min the gold nanocone is shaped and the films are etched away from the plateau surface and a large area underneath. (f) A zoom view of the gold nanocone which has a tip radius of 30 ± 2 nm and opening angle of 65 °.

After 4 min dry etching, the shaped nanocone is overetched, which is a clear evidence that the hard masks as the Pt pillar and the Al_2O_3 film were completely etched. From Fig. 5.7e,f, it is hard to precisely extract the nanocone dimensions due to the strong charging effect in the SEM image, since as in Fig. 5.7e the films at the plateau surface and a large area underneath were etched. The fabricated nanocone in Fig. 5.7f has a blunt tip with a radius of 30 nm ± 2 nm and an opening angle of about 65 °, which is consistent with the fact that the nanocone is overetched.

In sample **P**, we encounter two issues: firstly the Pt hard mask was strongly tilted, and secondly particles with different sizes were attached to the fiber during

the transport after the Ar-milling steps. As shown in Fig. 5.8a the T-OF has a tip radius of 68 ± 4 nm and an opening angle of 22°. In the same fabrication sequence as in section 5.2.1 the apex was milled by the FIB, followed by depositing thin films of 120 nm of gold and on the top 15 nm of Al_2O_3. The Pt mask deposited by the FEBID as in Fig. 5.8c was strongly tilted, due to unexpected drift of the e-beam. In spite of the asymmetric Pt pillar we continued working with this sample.

Hence, we start the Ar-milling process and expect that the Ar^+ beam may gradually turn it into a symmetric pillar. After 5 min Ar^+ milling, the tilted mask part was almost milled as in Fig. 5.8d. Then after additional milling for 1.5 min, we get a nanocone which has an opening angle of 82°, and with a height of 121 ± 12 nm and tip radius 20 ± 12 nm. In Fig. 5.8d, e, some accumulations start to appear in contrast with the SEM images taken before the Ar^+ step. They are likely particles attached due to the electrostatic charges at the fiber walls surface. Hence, we need to test the possibility to clean or reduce the size of the particles located around the nanocone site by applying side cleaning using Ar^+. Accordingly, we mount the fiber with an angle of 45° with respect to the Ar^+, assuming that at 45° the plateau will shield the nanocone, while the beam will hit only the fiber sidewalls. Unfortunately, this was not the case, and the nanocone dimensions changed after the side cleaning. In Fig. 5.8g, the SEM image of **P** after side cleaning, the size of the particles was reduced, and fiber walls were more clean from the residual thin films. In terms of the nanocone shape, the tip radius gets broadened and becomes 23 ± 10 nm, and the opening angle gets smaller and becomes about 69 °. The nanocone height in Fig. 5.8g after the side cleaning is about 125 ± 10 nm, since the gold film was 120 nm thick so intuitively this nanocone tip may still have an about 5 nm cap made of the hard masks.

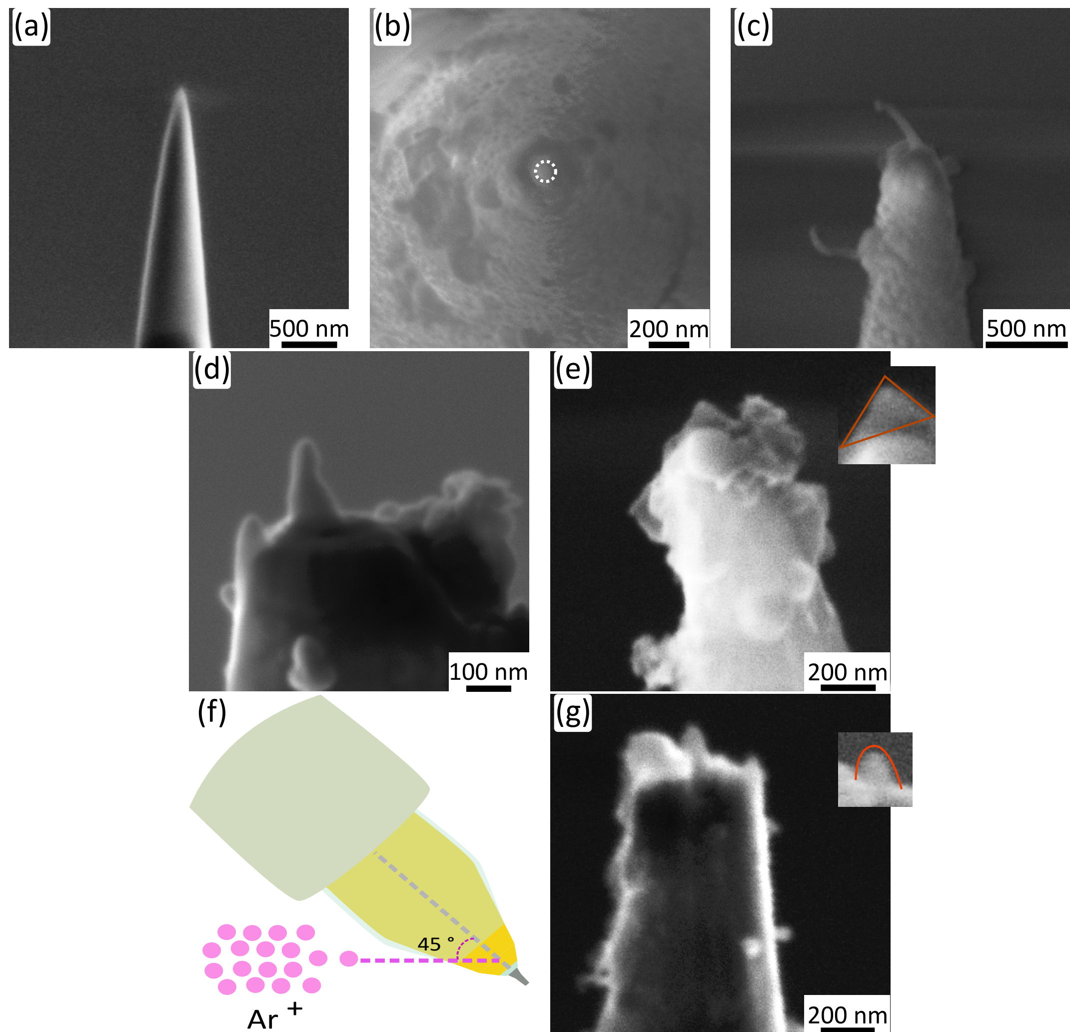

Figure 5.8: In sample **P** fabrication, we were confronted with two complications, a tilted Pt mask and particles near the nanocone site. (b) A circular plateau formed after FIB milling of the T-OF tip, then it was coated with a thin film stack. (c) Pt mask deposited by FEBID, which suffered from a long and tilted upper part. (d) After 5 min Ar $^+$ milling the Pt mask became a symmetric pillar. (e) A nanocone formed after 6.5 min Ar $^+$ milling, and it is surrounded with large particles. (f) Schematic drawing of the side clean step in Ar $^+$ milling. (g) After 4 min side clean, the particle size is reduced and the fiber gets more clean but the nanocone tip radius is broadened and its opening angle gets smaller.

Sample		**O**	**P**	**Q**	**U**
Mask type		Pt pillar by FEBID		SiO_2 disc by FIB	
Hard Mask	Height	265	-	≈ 120	≈ 60
	Base	144	91	114	154
(nm)	Error $\pm$ (nm)	15	-		-
Ar -milling time (min)		4	6.5	3.5	3.5
Gold	Height	84	125	144	70
	Base diameter	110	171	234	225
nanocone	Tip radius	30	23	22	26
(nm)	Error $\pm$ (nm)	2	10		17
	Opening angle (°)	65	69	83	120

Table 5.5: Summary of the single mode fiber samples (**O**-**U**): Pt hard mask height and base diameter, the Ar-milling time and the fabricated gold nanocone dimension. Samples **Q** and **U** have a SiO_2 hard mask, and they were patterned using FIB. The base diameter in **O** and **P** was calculated from the height and opening angle, since the SEM images were not clear enough.

The alternative method for depositing a hard mask as described in chapter 3 is to mill a ring shape using the FIB. In chapter 4 it has been fully applied on the AFM cantilevers. In the next samples **Q** and **U**, we used single mode fibers which were tapered by the pull and heat method to demonstrate the method of hard masks patterned by FIB to produce nanocones on fibers. The plateau in **Q** (Fig. 5.9a) and **U** (Fig. 5.9d) was obtained after milling the T-OF apex, then coated by the thin films stack of gold and SiO_2 with the thicknesses listed in Tab. 5.4. It is noticeable from Fig. 5.9b, that in **Q** the deposition rate of the SiO_2 was not stable and formed spike like shapes. The next step is to mill a ring shape through the deposited thin films using the FIB.

In **Q** as in Fig. 5.9b, the cylinder is overmilled due to the high milling dose, and it becomes more conical (or frustum) rather than being cylindrical. After the Ar^+ milling of the SiO_2 film, the shaped nanocone has a tip radius of about

22 nm and an opening angle of 83 °.

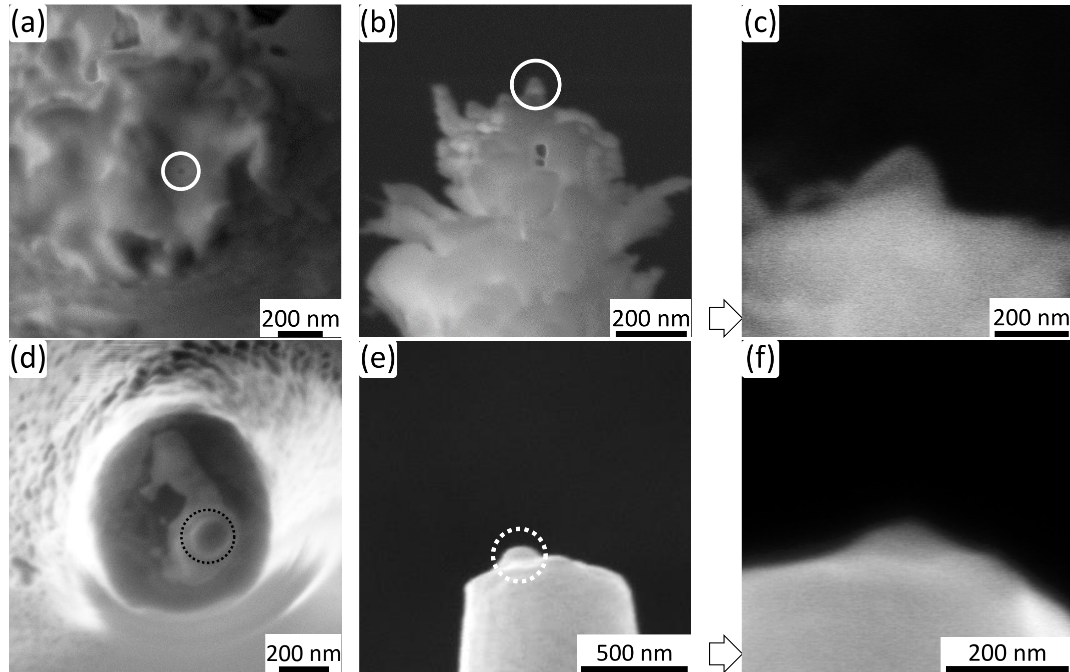

Figure 5.9: Samples **Q** (a-c), **U** (d-f), the nanocone was fabricated by only a SiO_2 disc patterned by FIB. The mask in both samples; (a, d) is the top view of the milled cylinder and (b, e) the side view. (c, f) After Ar^+-milling, the nanocone is shaped.

In **U**, the FIB milling produced a cylindrical pillar as in Fig. 5.9d,e with more flat top compared to the one in **Q**. But, the nanocone is strongly overetched as in Fig. 5.9f after the Ar^+ milling step.

We see in **Q** and **U** that a disc mask patterned by FIB milling is efficient to fabricate the SNOM probe made of a plasmonic nanocone on top of a tapered fiber.

Nanocone formed by shadow evaporation

In this section we demonstrate the possibility to fabricate a single nanocone using the shadow hole mask method [69] on top of a non planar substrate such as a tapered optical fiber. The shadow mask is a well established method to produce a large scale area of nanostructures, the main parameters that define the process are the aspect ratio of the hole, evaporation rate and angle. In Fig. 5.10 a-d,

we show how it was applied on T-OF starting with coating the substrate with an Al thin film as a sacrificial layer, then we drill a hole using FIB. Afterward, we deposit the adhesive material, then the gold thin film. Finally, we immersed the fiber in hydrochloric acid to lift off the Al thin film and expect the Al film will dissolve and take away the residual thin films. Hence, we can obtain a single plasmonic nanocone on top of a bare tapered fiber.

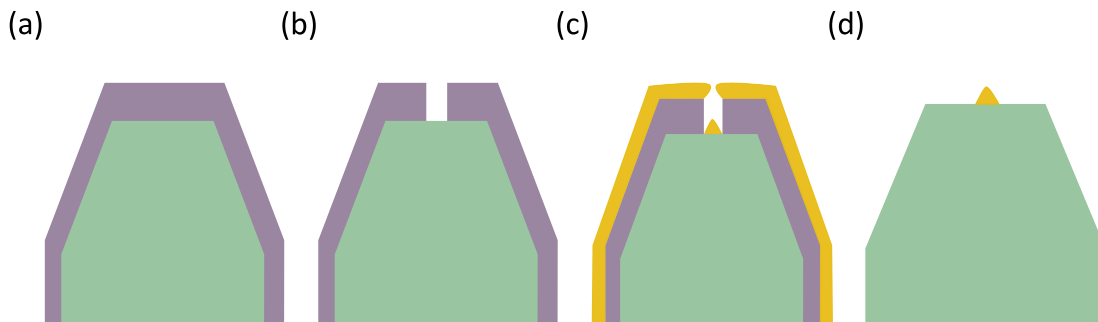

Figure 5.10: Schematic drawing of the shadow evaporation method to fabricate a nanocone. (a) A thick thin film of a sacrificial material (Cr or Al) is deposited. (b) A cylindrical hole is milled using the FIB through sacrificial material. (c) Deposit adhesive material followed by the gold thin film. The opening of the hole diameter gets gradually smaller and smaller which finally leads to a gold nanocone. (e) After performing lift off of the sacrificial material, we obtain a single nanocone on top of a tapered fiber

Sample **V** is one of the few samples in which we were able as in Fig. 5.11 to have a gold nanocone using the shadow mask.

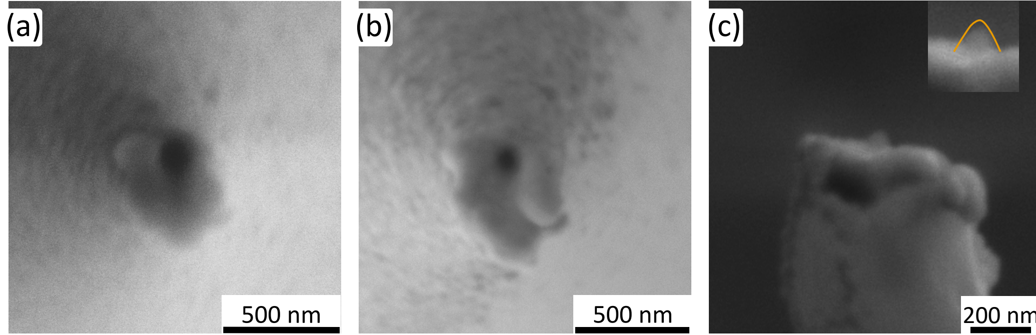

Figure 5.11: The nanocone fabrication in sample **V** achieved by shadow mask. (a) Top view of a T-OF coated with Al thin film of 300 nm thickness as a sacrificial layer, and the hole with a 134 nm diameter was milled by FIB. (b) Top view after depositing 100 nm of gold through the shadow mask. (c) A single nanocone remained on top of the T-OF after lift off of the Al sacrificial layer.

The sacrificial layer was Al with 300 nm thickness, then we milled using the FIB a circular hole with a diameter of 134 nm. Then, we deposited the Ti as adhesive material and 100 nm plasmonic gold thin film. The nanocone was obtained after immersing the sample **V** in HCl to liftoff the Al sacrificial layer. We tried to apply this method in several samples but we found different challenges. The main one was that using a metal thin film (Al or Cr) coated with another metal thin film (Au) makes the lift off step very difficult, since it is very likely for passivation to occur and the Al would not be affected by the chemical etching acid. Hence, the sacrificial layer should be a polymer, which is not straight forward to be deposited on a non-planar substrate. Further, a window must be opened either by Ar^+ or FIB side milling through the gold thin film. Thus, etching acid can leak through the gold thin film to attack and dissolve the sacrificial layer.

5.3 Simulation of the scattering of the nanocones

To determine the LSPR of the nanocones fabricated on fibers, we performed 3D FDTD simulations using the same conditions mentioned in section 4.3. In Fig. 5.12a, the LSPR of the cones with the same geometry embedded in air ranges from 543 nm to 607 nm, and it shows almost a linear dependency on the cone height as in Fig. 5.12b. But, the LSPR can be shifted by the aspect ratio and the substrate refractive index as in [61], or might be affected by another geometric parameter such as the cone tip diameter and/or opening angle. The

LSPR in Fig. 5.12a shows the best matching laser to excite the nanocone probe in the SNOM/TERS measurements, which is probably to be the 633 nm He-Ne line similar to the nanocones SNOM/TERS measurement for carbon nanotubes and polymer reported in [56] and/or 532 nm wavelength light used in TERS measurement for DNA as in [134].

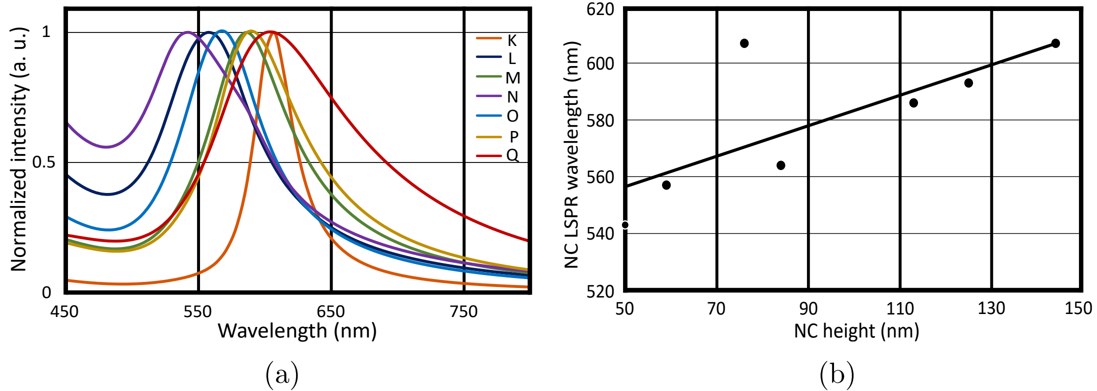

(a) (b)

Figure 5.12: (a) Scattering spectrum of the cones with the same geometry as the fabricated ones on T-OF calculated by 3D FDTD simulation using Lumerical commerical software. (b) The LSPR shows almost a linear dependency on the height of the cones in agreement with the model in [61].

5.4 Conclusion

We fabricate SNOM probes as a tapered optical fiber with a plasmonic nanocone. The fabrication process was described in chapter 3. The proposed design makes them accessible to be implemented in SNOM instruments with STM feedback mechanism. We attempted to find the protocol to fabricate a high quality SNOM probe with good reproducibility and throughput.

The quality of this SNOM design is challenged by the morphology of the chemically tapered fiber and the metal thin film residuals. In principle, we improve the morphology significantly when we etch the fibers in semi dynamic mode, and etch the fiber core in buffered HF solution. Then, by tuning the opening angle of the tapered tip we reduce the thickness of the residual metal thin film as in the case of Sample **N**.

The nanocone has been fabricated using a Pt pillar and it can be ultimately sharp with a tip radius as small as 7 nm. As shown in chapter 4 the Pt pillar hard mask was not reproducible in its shape, dimensions and etch rate. Hence,

the nanocones in most of the samples were overetched.

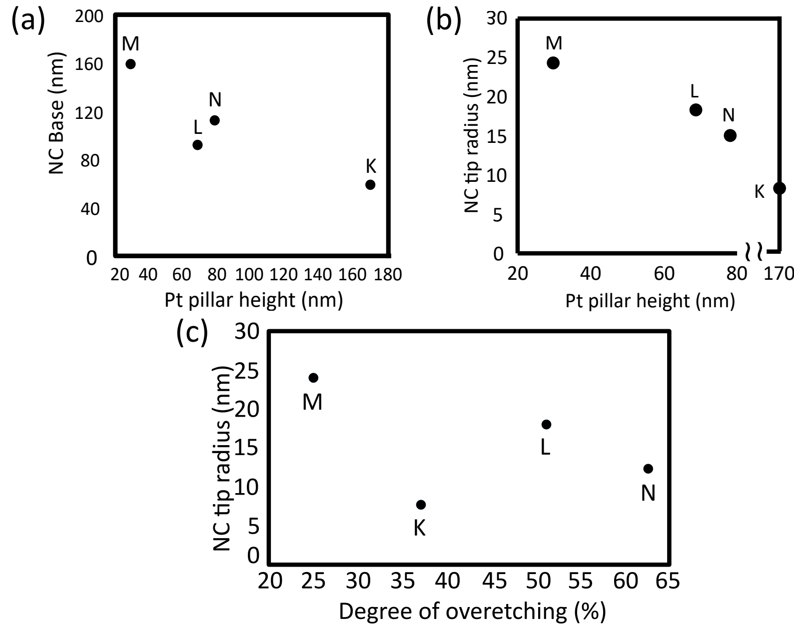

Figure 5.13: The dependency of the nanocone dimensions on Pt mask height; (a) The nanocone base diameter gets smaller with increasing Pt mask height, (b) The tip radius gets sharper in the samples with longer Pt mask. (c) The overetch did not show a significant influence on the sharpness of the nanocone tip.

Base diameter vs Pillar height

The nanocone base diameter in the samples **K**-**N** as in Fig. 5.13a is decreasing with increasing the height of the Pt pillar.

To clarify this relation, we must consider the lateral erosion of the Al_2O_3 film. The longer Pt masks appear to tune the lateral eroding rate of the Al_2O_3 film edges with respect to the one in the center. Thus, it can be a method to produce a nanocone with higher aspect ratio and sharper tip.

Nanocone tip radius vs Pt pillar height

We can intuitively correlate as in Fig. 5.13b the nanocone tip radius with the Pt mask height. It is clear that the sharpest nanocone was obtained with the highest pillar. Consequently, the longer Ar^+ milling time will lead to lateral sharpening

of the nanocone, and as long as the mask is not etched the nanocone tip and height are protected.

Hence, the nanocone base diameter, sharpness and opening angle can be tailored by employing a hybrid etch mask, which is made of materials with different milling rate and/or different dimensions (i.e. pillar width and oxide film).

Nanocone tip radius vs degree of overetching

Further, we need to consider the tip radius dependency on the degree of overetching of the deposited gold film. We found in Fig. 5.13c that the tip radius is broadened by the overetching in **N** and **L**. By considering **K** and **M** in Fig. 5.13c, we see that the pillar in **K** is much higher than in **M** while **K** is more overetched than **M**. In spite of this, **K** has the sharper nanocone than **M**.

Hence, the height of the pillar is more effective in sharpening the nanocone than the detrimental effect of the overetching.

The challenge in the nanocone fabrication on a non-planar substrate was to have a reproducible hard mask with a constant Ar^+-milling rate and which can be patterned in different dimensions to fabricate nanocones with different aspect ratios to cover a broad wavelength spectrum. In principle, the FIB ring milling method can provide the optimal hard mask to fabricate a nanocone also in the case of planar substrates in [65]. Hence by applying the FIB ring milling, we can have a high throughput since the milling rate of the mask is constant compared to the Pt pillar, and there is no need to split the milling step into distinct steps to check the mask milling progress by SEM imaging. Further, a reproducible hard mask can be obtained by only well optimizing the FIB sputter rate while the Pt pillar deposition depends on several parameters that were hard to control, such as the pillar symmetry and the carbon contamination.
There are three main precautions to enhance the quality of the nanocone based SNOM probe; firstly having a smooth morphology either by optimizing the fiber chemical etching e.g. as in section 5.1 or by using the heat and pull fiber, secondly reducing or etching away the residual thin film by minimizing the T-OF opening angle as in **N** or by carefully applying side cleaning as in **P**, and the last one is optimizing the FIB ring milling to get a more defined hard mask diameter as in **U**, not overmilled as in Q.

The FDTD simulations of the scattering spectrum of the nanocones show that the LSPR depends on both height and the aspect ratio of the nanocone. Thus, a well controlled engineering of the nanocone dimensions is demanded to define the LSPR wavelength and FWHM. The fabrication method of the SNOM probe-

based nanocone offers versatile ways to tailor the nanocone dimensions to match its plasmonic resonance with the spectral range of interest. From a series test on FIB milling of a ring shape, we found that patterning a well defined cylinder with sub-100 nm diameter is achievable on a planar substrate and should be as well on non-planar ones. Hence, good definition of the nanocone base diameter and aspect ratio is more likely to be achieved by FIB milling of the mask rather than FEBID deposition of the mask. This can pave the way towards fabricating a well controlled SNOM probe with high quality, and the method has good reproducibility and throughput.

Outlook

The residual thin films could be removed from the walls of the T-OF using the liftoff method. Thus, adding a sacrificial layer of polymer before milling the tip and then etching it away. This polymer layer can be applied using dip coating or spray coating and/or polymer thin film evaporation.

Optimization of the milling dose of the ring using FIB should be further pursued, since it shows a high reproducibility and fabrication throughput.

The particles attached to the fiber walls very often occur with single mode fibers in contrast to multimode fibers, this might be excluded by depositing a thick layer of transparent adhesive material such as TiO_2 as in [65].

Finally, this SNOM probe may be used in other applications such as nanolithography and quantum atom manipulations.

Chapter 6

Summary

There are many sophisticated methods to fabricate apertureless SNOM probes [40,60]. They include the fabrication of a tapered metal tip, a metal coated dielectric tip, a metal coated nanotip deposited by FEBID, and attaching a nanoparticle at the apex of a sharp dielectric tip.
These methods did not offer an access to well control the dimensions of the nanostructure, and can not freely tune the plasmonic resonance. In the tapered metal tip, they have a low coupling efficiency entailing the need to structure a coupler such as a grating to launch the SPPs [135]. The field enhancement on metal tips mainly stems from the lightning rod effect [14], and they exhibit a non radiative loss [14, 136]. In case of attaching a nanoparticle, it is hard to obtain a single nanoparticle at the apex, and if they have a spherical shape there will be a trade off between the spatial resolution relying on their radius and their field enhancement.

On the other side, direct fabrication methods such as FEBID deposition of a nanotip suffer from carbon impurities from the uncompleted dissociation of the organometallic molecules, and thus they will be very lossy and field localization will not be efficient. Then, direct milling of a nanogap using FIB will implant Ga^+ in the nanostructure, which can alter their dielectric function [137] and reduce their field enhancement [138].

A counterpart of the FIB method can be the direct milling of the nanocone using He^+ ions, in a way that a gradient milling dose can be applied to control the lateral erosion [139], thus tailoring the nanocone dimensions and symmetry. The He^+ milling avoids the ion implantation compared to Ga^+ FIB, but it has a slow milling speed compared to Ga^+ FIB [140].
The fabrication of the nanocone using a hard mask deposited by FEBID on top of an AFM-C has solved many of these issues, by fabricating a high purity gold

nanocone with good control over its dimensions, hence the ability to tune its plasmon resonance. [56] The plasmonic nanocone has unique properties by having a fine pointing tip, and theoretically its field enhancement is higher than the one of the tapered metal tip. It is achieved by lightning rod effect and localized plasmon resonance. The nanocones can be engineered to tune their plasmon resonance to cover a broad electromagnetic spectrum [61].

In this work, we propose additionally modifying the process to fabricate the nanocone with good reproducibility using a disc mask directly patterned by the FIB [70]. We extend the types of substrates by applying the nanocone fabrication techniques on different classes of tapered optical fibers. Thus, it becomes flexible to be implemented in different SNOM/TERS setups. Further, it can be implemented in a variety of applications which demand high field localization in a sub-10 nm region such as quantum atom manipulations and nanolithography. We pay attention to enhance the overall quality of the probe by reducing the residual films on the sides.

Further, the method of patterning the hard mask with FIB can be employed to fabricate a single nanostructure with a complicated geometry on top of a submicron non planar substrate, where e-beam lithography is hard to be applied.

Appendix A

Appendix

A.1 Cantilever specifications

	Min.	Average	Max.
Pyramid Height (μm)	14	-	16
Beam Length (μm) Width (μm) Thickness (μm)	 85 25 1.5	 95 30 2	 105 35 2.5
Force constant (N/m) Resonant frequency (kHz)	3.1 140	11.8 240	37.6 390

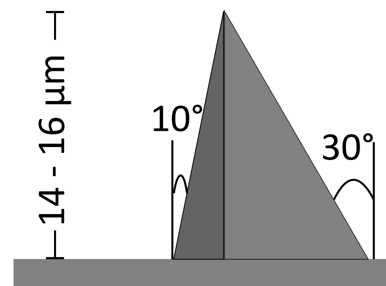

Table A.1: The specifications provided by NT-MDT of the non contact AFM-C, were used in this work.

A.2 Process of FIB milling the AFM-C tip

- Fix the AFM-C on a 45° inclined stainless steel samples holder which using a double face carbon poly pad.
- Place the sample holder inside a load lock, to transport the samples into the FIB main chamber.
- Pump the FIB chamber to vacuum in the order of 10^{-6} mbar.
- Start to adjust the extractor and suppressor voltages to achieve a stable Ga^+ FIB emission current equal to 2.2 μA, then switching on the FIB.
- Adjust the tip long axis to be perpendicular to the Ga^+ beam, thus we rotate the sample holder by 180°, and then tilt it by additional 7°.
- Finally, select the start point to mill the tip, and obtain a plateau.

A.3 Preparation of the fiber for the FIB milling

- Oxidize the Si substrate in an oven, to obtain SiO_2 with thickness between 800 and 1100 nm.
- Coat with photoresist and pattern it with optical lithography to form a grating with a pitch of about 5 mm and width of about 1.5 mm.
- Etch the unprotected SiO_2 area with reactive ion etching.
- Dissolve the photoresist, thus the SiO_2 will be a mask to protect from the potassium hydroxide (KOH).
- Etch rectangular grooves in a Si substrate with (100) orientation formed by anisotropic etching in KOH.
- Fix the T-OF by bonding it on top of the Si substrate using a small amount of indium (In).
- Fix the Si substrate with T-OF on its top, on a stainless steel sample holder.
- Insert the samples in the FIB machine, then adjust the vacuum and beam condition as in appendix A.2
- Tilt the samples holder with an angle of 52 °, to have the T-OF long axis perpendicular with the Ga $^+$ beam.

A.4 Sputter Yield Calculations

In the Strata D235 machine from FEI, we milled the ring shape in Fig. 4.5d in section 4.1.2 using Ga^+ FIB with a current of 22 pA at 30 kV, and milling angle 0°. The cylinder in SiO_2 has an outer radius of 700 nm and an average inner radius of 79 ± 4 nm, with a height of 123 nm. The one milled in Si has a height of about 145 nm, and its outer radius and inner radius are 700 nm and 66 ± 4 nm, respectively. We used the sputtered volume of the cylindrical shell to calculate intuitively the sputter yield for Si and SiO_2 which is 5.9 (at/ion) and 1.8 (at/ion) respectively. The values used in the calculation are listed in Tab.(A.2).

Material	Sputtered Volume (μm^3) ($\times 10^{-10}$)	Density (g/cm^3)	Molar mass (g/Mol)	No. of sputtered atoms ($\times 10^{10}$)	No. of ions at 22 pA ($\times 10^9$)
SiO_2	1.85	2.65	60.08	0.494	2.76 (20.06 sec.)
Si	2.18	2.32	28.08	1.0854	1.84 (13.75 sec.)

Table A.2: Table of the parameters used to calculate the sputter yield of SiO_2 and Si. The sputtered volume is the volume of a cylindrical shell.

Bibliography

[1] D.W. Pohl, W. Denk and M. Lanz, "Optical stethoscopy: Image recording with resolution $\lambda/2$", Appl. Phys. Lett. **44** (1984) 651.

[2] A. Lewis, M. Isaacson, A. Harootunian and A. Muray, "Development of a 500 Å spatial resolution light microscope: I. light is efficiently transmitted through $\lambda/16$ diameter apertures", Ultramicroscopy **13** (1984) 227.

[3] S. Kalinin and and A. Gruverman, Scanning Probe Microscopy: Electrical and Electromechanical Phenomena at the Nanoscale, Springer New York, 2007.

[4] E.H. Synge, "A suggested method for extending microscopic resolution into the ultramicroscopic region", Phil. Mag. **6** (1928) 356.

[5] Lukas Novotny, Progress in Optics **50** (2007) 137.

[6] J.M. Gerton, L.A. Wade, G.A. Lessard, Z. Ma and S.R. Quake, "Tip-Enhanced Fluorescence Microscopy at 10 Nanometer Resolution", Phys. Rev. Lett. **93** (2004) 180801.

[7] T.S. van Zanten, J. Gòmez, C. Manzo, A. Cambi, J. Buceta, R. Reigada and M.F. Garcia-Parajo, "Direct mapping of nanoscale compositional connectivity on intact cell membranes", Proc. Natl. Acad. Sci. U.S.A. **107** (2010) 15437.

[8] H. Kim, K.M. Kosuda, R.P. Van Duyne and P.C. Stair, "Resonance Raman and surface- and tip-enhanced Raman spectroscopy methods to study solid catalysts and heterogeneous catalytic reactions", Chem. Soc. Rev. **39** (2010) 4820.

[9] K.F. Domke and B. Pettinger, "Studying Surface Chemistry beyond the Diffraction Limit: 10 Years of TERS", ChemPhysChem **11** (2010) 1365.

[10] P. Bazylewski, S. Ezugwu and G. Fanchini, "A Review of Three-Dimensional Scanning Near-Field Optical Microscopy (3D-SNOM) and Its Applications in Nanoscale Light Management", Appl. Sci. **7** (2017) 973.

[11] A. Martinez-Marrades, L. Greusard, Y. De Wilde, N. Bardou, S. Collin, M. Guillon, G. Tessier, "Characterization of plasmonic nanoantennas by Holographic Microscopy and Scanning Near-field Microscopy", Opt. Commun. **359** (2016) 455.

[12] S. Ezugwu, H. Yea, and G. Fanchini, "Three-dimensional scanning near-field optical microscopy (3D-SNOM) imaging of random arrays of copper nanoparticles: Implications for plasmonic solar cell enhancement", Nanoscale **7** (2015) 252.

[13] H. Wang, L. Wang, D.S. Jakob, and X.G. Xu, "Mapping three-dimensional near-field responses with reconstruction scattering-type scanning near-field optical microscopy", AIP Advances **7** (2017) 055118.

[14] L. Novotny and B. Hecht, Principles of Nano-Optics. 2nd Ed, Cambridge University Press, 2012.

[15] S.A. Maier. Plasmonics: Fundamentals and Applications. Springer US, 2007.

[16] J. Greffet and R. Carminati, "Image formation in near-field optics", Prog. Surf. Sci. **56** (1997) 133.

[17] N. Yao and Z.L. Wang. Handbook of Microscopy for Nanotechnology. Springer US, 2005.

[18] M. Fox. Optical Properties of Solids. 2nd Ed, Oxford University Press, 2010.

[19] K.A. Willets and R.P. Van Duyne, "Localized Surface Plasmon Resonance Spectroscopy and Sensing", Annu. Rev. Phys. Chem. **58** (2007) 267.

[20] U. Kreibig and M. Vollmer. Optical Properties of Metal Clusters. Springer Berlin Heidelberg, 1995.

[21] A. Vial, A.S. Grimault, D. Macías, D. Barchiesi, and M.L. de la Chapelle, "Improved analytical fit of gold dispersion: Application to the modeling of extinction spectra with a finite-difference time-domain method", Phys. Rev. B **71** (2005) 085416.

[22] S. Enoch and N. Bonod. Plasmonics from Basics to Advanced topics. Springer Berlin Heidelberg, 2012.

[23] P.B. Johnson and R.W. Christy, "Optical Constants of the Noble Metals", Phys. Rev. B **6** (1972) 4370.

[24] C.F. Bohren and D.R. Huffman. Absorption and Scattering of Light by Small Particles. Wiley 1998.

[25] V. Giannini, A.I. Fernández-Domínguez, S.C. Heck, and S.A. Maier, "Plasmonic Nanoantennas: Fundamentals and Their Use in Controlling the Radiative Properties of Nanoemitters", Chem. Rev. (2011) **111** 3888.

[26] X. Shi, N. Coca-López, J. Janik, and A. Hartschuh, "Advances in Tip-Enhanced Near-Field Raman Microscopy Using Nanoantennas", Chem. Rev. **117** (2017) 4945.

[27] P. Bharadwaj, B. Deutsch, and L. Novotny, "Optical Antennas", Adv. Opt. Photon. **1** (2009) 438.

[28] L. Novotny, "Effective Wavelength Scaling for Optical Antennas", Phys. Rev. Lett. **98** (2007) 266802.

[29] N. Engheta, A. Salandrino, and A. Alù, "Circuit Elements at Optical Frequencies: Nanoinductors, Nanocapacitors, and Nanoresistors", Phys. Rev. Lett. **95** (2005) 095504.

[30] N. Engheta, “Circuits with Light at Nanoscales: Optical Nanocircuits Inspired by Metamaterials”, Science **317** (2007) 1698.

[31] Lumerical Inc. (FDTD 3D Electromagnetic Simulator)

[32] COMSOL Multiphysics®(COMSOL AB, Stockholm, Sweden).

[33] F.J. García de Abajo and A. Howie, “Retarded field calculation of electron energy loss in inhomogeneous dielectrics”, Phys. Rev. B **65** (2002) 115418.

[34] R.J. Hermann and M.J. Gordon, “Nanoscale Optical Microscopy and Spectroscopy Using Near-Field Probes”, Annu. Rev. Chem. Biomol. Eng. **9** (2018) 365.

[35] M.A. Paesler and P.J. Moyer. Near-Field Optics: Theory, Instrumentation, and Applications. Wiley New York, 1996.

[36] A. Syed and E.A. Smith, “Raman Imaging in Cell Membranes, Lipid-Rich Organelles, and Lipid Bilayers”, Annu. Rev. Anal. Chem. **10** (2017) 271.

[37] A. Jorio and A.G.S. Filho, “Raman Studies of Carbon Nanostructures”, Annu. Rev. Mater. Res. **46** (2016) 357.

[38] S. Kawata, T. Ichimura, A. Taguchi, and Y. Kumamoto, “Nano-Raman Scattering Microscopy: Resolution and Enhancement”, Chem. Rev. **117** (2017) 4983.

[39] A.B. Zrimsek, N. Chiang, M. Mattei, S. Zaleski, M.O. McAnally, C.T. Chapman, A. Henry, G.C. Schatz, and R.P. Van Duyne, “Single Molecule Chemistry with Surface- and Tip-Enhanced Raman Spectroscopy”, Chem Rev. **117** (2017) 7583.

[40] M. Fleischer, “Near-field scanning optical microscopy nanoprobes”, Nanotechnol. Rev. **1** (2012) 313.

[41] F. Zenhausern, M.P. O’Boyle and H.K. Wickramasinghe, “Apertureless near-field optical microscope”, Appl. Phys. Lett. **65** (1994) 1623.

[42] B. Hecht, B. Sick, U.P. Wild, V. Deckert, R. Zenobi, O.J.F. Martin, and D.W. Pohl, “Scanning near-field optical microscopy with aperture probes: Fundamentals and applications”, J. Chem. Phys. **112** (2000) 7761.

[43] L. Novotny and S.J. Stranick, “Near-field optical microscopy and spectroscopy with pointed probes”, Ann. Rev. Phys. Chem. **57** (2006) 303.

[44] U.C. Fischer, J. Koglin and H. Fuchs, “The tetrahedral tip as a probe for scanning near-field optical microscopy at 30 nm resolution”, J. Microsc. **176** (1994) 231.

[45] E.G. Bortchagovsky and U.C. Fischer, “A tetrahedral tip as a probe for tip-enhanced Raman scattering and as a near-field Raman probe”, J. Raman Spectrosc. **40** (2009) 1386.

[46] R.D. Grober, T.D. Harris, J.K. Trautman, and E. Betzig, “Design and implementation of a low temperature near-field scanning optical microscope”, Rev. Sci. Instrum. **65** (1994) 626.

[47] A. Patane and N. Balkan. Semiconductor Research Experimental Techniques. Springer, 2012.

[48] D. Richards,"Near-field microscopy: throwing light on the nanoworld", Phil. Trans. R. Soc. Lond. A **361** (2003) 2843.

[49] L. Novotny and D.W. Pohl, "Light propagation in scanning near-field optical microscopy" in Photons and Local Probes, ed. O. Marti and R. Möller. Springer, 1995.

[50] J. Weiner, "The physics of light transmission through subwavelength apertures and aperture arrays", Rep. Prog. Phys. **72** (2009) 06440.

[51] N. Hayazawa, A. Tarun, A. Taguchi, and S. Kawata, "Development of Tip-Enhanced Near-Field Optical Spectroscopy and Microscopy", Japn. J. Appl. Phys. **48** (2009) 08JA02.

[52] S.S. Kharintsev, A.M. Rogov, and S.G. Kazarian, "Nanopatterning and tuning of optical taper antenna apex for tip-enhanced Raman scattering performance", Rev. Sci. Instrum. **84** (2013) 093106.

[53] L. Wang and X. Xu, "High transmission nanoscale bowtie-shaped aperture probe for near-field optical imaging", Appl. Phys. Lett. **90** (2007) 261105.

[54] G. Calafiore, A. Koshelev, T.P. Darlington, N.J. Borys, M. Melli, A. Polyakov, G. Cantarella, F.I. Allen, P. Lum, E. Wong, S. Sassolini, A. Weber-Bargioni, P.J. Schuck, S. Cabrini and K. Munechika, "Campanile Near-Field Probes Fabricated by Nanoimprint Lithography on the Facet of an Optical Fiber", Sci. Rep. **7** (2017) 1651.

[55] M. Martina, M. Fleischer, J. Burkhardt, "Template stripping and bonding of smooth probes with nanoscale features for tip-enhanced Raman spectroscopy", Microelectron. Eng. **171** (2017) 31.

[56] M. Fleischer, A. Weber-Bargioni, S. Cabrini, D.P. Kern, "Fabrication of metallic nanocones by induced deposition of etch masks and ion milling", Microelectron. Eng. **88** (2011) 2247.

[57] A.J. Babadjanyan, N.L. Margaryan, and Kh.V. Nerkararyan, "Superfocusing of surface polaritons in the conical structure ", J. Appl. Phys. **87** (2000) 3785.

[58] P.W. Barber, R.K. Chang, and H. Massoudi, "Surface-Enhanced Electric Intensities on Large Silver Spheroids", Phys. Rev. Lett. **50** (1983) 997.

[59] P.W. Barber, R.K. Chang, and H. Massoudi, "Electrodynamic calculations of the surface-enhanced electric intensities on large Ag spheroids", Phys. Rev. Lett. **27** (1983) 7251.

[60] S. Kawata, T. Ichimura, A. Taguchi, and Y. Kumamoto, "Nano Raman Scattering Microscopy: Resolution and Enhancement", Chem. Rev. **117** (2017) 4983.

[61] C. Schäfer, D.A. Gollmer, A. Horrer, J. Fulmes, A. Weber-Bargioni, S. Cabrini, P.J. Schuck, D.P. Kern, and M. Fleischer, "A single particle plasmon resonance study of 3D conical nanoantennas", Nanoscale **5** (2013) 7861.

[62] C. Dreser, D.A. Gollmer, G. Bautista, X. Zang, D.P. Kern, M. Kauranen and M. Fleischer, “Plasmonic mode conversion in individual tilted 3D nanostructures”, Nanoscale **11** (2019) 5429.

[63] M. Fleischer, A. Weber-Bargioni, M.V.P. Altoe, A.M. Schwartzberg, P.J. Schuck, S. Cabrini, and D.P. Kern, “Gold Nanocone Near-Field Scanning Optical Microscopy Probes”, ACS Nano **5** (2011) 2570.

[64] M. Fleischer, C. Stanciu, F. Stade, J. Stadler, K. Braun, A. Heeren, M. Häffner, D.P. Kern, and A.J. Meixner, “Three-dimensional optical antennas: Nanocones in an apertureless scanning nearfield microscope”, Appl. Phys. Lett. **93** (2008) 111114.

[65] M. Fleischer, F. Stade, A. Heeren, M. Häffner, K. Braun, C. Stanciu, R. Ehlich, J.K.H. Hörber, A.J. Meixner, D.P. Kern, “Nanocones on transparent substrates for investigations in scanning probe microscopes”, Microelectron. Eng. **86** (2009) 1219.

[66] F. Stade, A. Heeren, M. Fleischer, D.P. Kern, “Fabrication of metallic nanostructures for investigating plasmon-induced field enhancement”, Microelectron. Eng. **84** (2007) 1589.

[67] M. Fleischer, D. Zhang, K. Braun, S. Jäger, R. Ehlich, M.Häffner, C. Stanciu, J.K.H. Hörber, A.J. Meixner and D.P. Kern, “ Tailoring gold nanostructures for near-field optical applications”, Nanotechnology **21** (2010) 065301.

[68] A. Horrer, C. Schäfer, K. Broch, D.A. Gollmer, J. Rogalski, J. Fulmes, D. Zhang, A.J. Meixner, F. Schreiber, D.P. Kern, and M. Fleischer, “Parallel Fabrication of Plasmonic Nanocone Sensing Arrays”, Small **9** (2013) 3987.

[69] H. Fredriksson, Y. Alaverdyan, A. Dmitriev, C. Langhammer, D.S. Sutherland, M. Zäch and B. Kasemo, “Hole-Mask Colloidal Lithography”, Adv. Mater. **19** (2007) 4297.

[70] O. Tanirah, D.P. Kern, M. Fleischer, “Fabrication of a plasmonic nanocone on top of an AFM cantilever”, Microelectron. Eng. **141** (2015) 215.

[71] J.M. Kontio, H. Husu, J. Simonen, M.J. Huttunen, J. Tommila, M. Pessa, and M. Kauranen, “Nanoimprint fabrication of gold nanocones with ∼10 nm tips for enhanced optical interactions”, Opt. Lett. **34** (2009) 1979.

[72] J. Fulmes, R. Jäger, A. Bräuer, C. Schäfer, S. Jäger, D.A. Gollmer, A. Horrer, E. Nadler, T. Chassé, D. Zhang, A.J. Meixner, D.P. Kerna and M. Fleischer, “Self-aligned placement and detection of quantum dots on the tips of individual conical plasmonic nanostructures”, Nanoscale **7** (2015) 14691.

[73] M.J. Levene, J. Korlach, S.W. Turner, M. Foquet, H.G. Craighead, and W.W. Webb, “Zero-mode waveguides for singlemolecule analysis at high concentrations”, Science **299** (2003) 682.

[74] G.A.C.M. Spierings, “Review wet chemical etching of silicate glasses in hydrofluoric acid based solutions”, J. Mat. Sci. **28** 6261 (1993).

[75] R.P. Bell, K.N. Bascombe and J.C. McCoubrey, “Kinetics of the depolymerisation of trioxan in aqueous acids, and the acidic properties of aqueous hydrogen fluoride”, J. Chem. Soc. (1956) 1286.

[76] W. Readey and D. Liang, “Dissolution Kinetics of Crystalline and Amorphous Silica in Hydrofluoric-Hydrochloric Acid Mixtures”, J. Am. Ceram. Soc., **70** (1987) 570

[77] W.E. Kline and H.S Fogler, “Dissolution kinetics: Catalysis by strong acids”, J. Colloid Interface Sci. **82** (1981) 93.

[78] G.A.C.M. Spierings, “Compositional effects in the dissolution of multicomponent silicate glasses in aqueous HF solutions”, J. Mater. Sci. **26** (1991) 3329.

[79] H. Kikyuama, N. Miki, K. Saka, J. Takano, I. Kawanabe, M. Miyashita, and T. Ohmi, “Principles of wet chemical processing in ULSI microfabrication”, IEEE Trans. Semi. Manuf. **4** (1991) 26.

[80] H. Kikuyama, M. Waki, I. Kawanabe, M. Miyashita, T. Yabune, N. Miki, J. Takano and T. Ohmi, “Etching Rate and Mechanism of Doped Oxide in Buffered Hydrogen Fluoride Solution”, J. Electrochem. Soc. **139** (1992) 2239.

[81] J.M. Ward, D.G. O’Shea, B.J. Shortt, M.J. Morrissey, K. Deasy, and S.G. Nic Chormaic, “Heat-and-pull rig for fiber taper fabrication”, Rev. Sci. Inst. **77** (2006) 083105.

[82] J.M. Ward, A. Maimaiti, Vu H. Le, and S. Nic Chormaic, “Contributed Review: Optical micro- and nanofiber pulling rig”, Rev. Sci. Inst. **85** (2014) 111501.

[83] D.R. Turner, **U.S. Patent No.** *4,469,554* (1984).

[84] P. Hoffmann , B. Dutoit, RP. Salathé, “Comparison of mechanically drawn and protection layer chemically etched optical fiber tips”, Utramicroscopy **61** (1995) 165.

[85] A. Lazarev, N. Fang, Q. Luo, and X. Zhang, “Formation of fine near-field scanning optical microscopy tips. Part I. By static and dynamic chemical etching”, Rev. Sci. Instrum. **74** (2003) 3679.

[86] M. Ohring. Materials Science of Thin Films: Deposition and Structure. 2nd Ed, Academic Press, 2002.

[87] D. Smith. Thin-film deposition : principles and practice. McGraw-Hill, 1995.

[88] R. Pretorius, J.M. Harris, M-A. Nicolet, ”Reaction of thin metal films with SiO_2 substrates”, Solid State Electron. **21** (1978) 667.

[89] M. Todeschini, A. Bastos da Silva Fanta, F. Jensen, J. B. Wagner, and A. Han, “Influence of Ti and Cr Adhesion Layers on Ultrathin Au Films”, ACS Appl. Mater. Interfaces **9** (2017) 42.

[90] H. Nagata, “Improvement of bonding strength between Au/Ti and SiO2 films by Si layer insertion”, J. Vac. Sci. Technol. A **17** (1999) 1018.

[91] K.M. McPeak, S.V. Jayanti, S.J.P. Kress, S. Meyer, S. Iotti, A. Rossinelli, and D.J. Norris, "Plasmonic Films Can Easily Be Better: Rules and Recipes", ACS Photonics **2** (2015) 326.

[92] R.M. Langford, P.M. Nellen, J. Gierak and Y. Fu, "Focused Ion Beam Micro- and Nanoengineering", MRS Bulletin **32** (2007) 417.

[93] C.A. Volkert and A.M. Minor, "Focused Ion Beam Microscopy and Micromachining", MRS Bulletin **32** (2007) 389.

[94] P. Sigmund, "Theory of Sputtering. I. Sputtering Yield of Amorphous and Polycrystalline Targets", Phys. Rev. **184** (1969) 383.

[95] R.M. Bradley and H. Hofsäss, "A modification to the Sigmund model of ion sputtering", J. Appl. Phys. **116** (2014) 234304.

[96] M. Nastasi, J.W. Mayer, J.K. Hirvonen. Ion-Solid Interactions: Fundamentals and Applications. Cambridge University Press, 1996.

[97] S. Lipp, L. Frey, C. Lehrer, B. Frank, E. Demm, H. Ryssel, "Investigations on the topology of structures milled and etched by focused ion beams", J. Vac. Sci. Technol. B **14** (1996) 3996.

[98] A.A. Tseng, "Recent developments in micromilling using focused ion beam technology", J. Micromech. Microeng. **14** (2004) R15.

[99] H-B. Kim, G. Hobler, A. Steiger, A. Lugstein and E. Bertagnolli, "Full three-dimensional simulation of focused ion beam micro/nanofabrication", Nanotechnology **18** (2007) 245303.

[100] T. Lianga, E. Frendberg, B. Lieberman, and A. Stivers, "Advanced photolithographic mask repair using electron beams", J. Vac. Sci. Technol. B **23** (2005) 3101.

[101] V. Friedli and I. Utke, "Optimized molecule supply from nozzle-based gas injection systems for focused electron- and ion-beam induced deposition and etching: simulation and experiment", J. Phys. D: Appl. Phys. **42** (2009) 125305.

[102] R.M. Thorman, R. Kumar T.P., D.H. Fairbrother, and O. Ingólfsson, "The role of low-energy electrons in focused electron beam induced deposition: four case studies of representative precursors", Beilstein J. Nanotechnol. **6** (2015) 1904.

[103] W.F. van Dorp, and C.W. Hagen, "A critical literature review of focused electron beam induced deposition", J. App. Phys. **104** (2008) 081301.

[104] P. Rowntree, L. Parenteau and L. Sanche,"Anion yields produced by low-energy electron impact on condensed hydrocarbon films", J. Phys. Chem. **95** (1991) 4902.

[105] T. Oster, A. Kühn, and E. Illenberger, "Gas phase negative ion chemistry", E. Int. J. Mass Spectrom. Ion Processes **89** (1989) 1.

[106] E. Böhler, J. Warneke, and P. Swiderek, "Control of chemical reactions and synthesis by low-energy electrons", Chem. Soc. Rev. **42** (2013) 9219.

[107] S. Massey, A.D. Bass, and L. Sanche, "Role of Low-Energy Electrons (¡35 eV) in the Degradation of $Fe(CO)_5$ for Focused Electron Beam Induced Deposition Applications: Study by Electron Stimulated Desorption of Negative and Positive Ions", J. Phys. Chem. C **119** (2015) 12708.

[108] P. Russell, S. Moshkalev, and I. Utke. Nanofabrication Using Focused Ion and Electron Beams : Principles and Applications, Oxford University Press, 2012.

[109] C. Tian and C.R. Vidal, "Cross sections of the electron impact dissociative ionization of CO, CH_4 and C_2 H_2" , J. Phys. B **31** (1998) 895.

[110] J.D. Wnuk, J.M. Gorham, S.G. Rosenberg, W.F. van Dorp, T.E. Madey, C.W. Hagen, and D.H. Fairbrother, "Electron Induced Surface Reactions of the Organometallic Precursor Trimethyl(methylcyclopentadienyl)platinum(IV)", J. Phys. Chem. C **113** (2009) 2487.

[111] H.W.P. Koops, R. Weiel, and D.P. Kern, "High-resolution electron-beam induced deposition", J. Vac. Sci. Technol. B **6** (1988) 477.

[112] I. Utke, P. Hoffmann and J. Melngailis, "Gas-assisted focused electron beam and ion beam processing and fabrication", J. Vac. Sci. Technol. B **26** (2008) 1197.

[113] A.D.G. Stewart and M.W. Thompson, " Microtopography of Surfaces Eroded by Ion-Bombardment", J. Mat. Sci. **4** (1969) 56

[114] G. Carter, "The physics and applications of ion beam erosion", J. Phys. D: Appl. Phys. **34** (2001) R1.

[115] R.M. Bradley, "Dynamic scaling of ion-sputtered rotating surfaces", Phys. Rev. E **54** (1996) 6149.

[116] L.T. Chadderton, "On a relationship between the geometry of cones on sputtered surfaces and the angular dependence of sputtered yields", Radiat. Eff. **33** (1977) 129.

[117] J.L. Whitton, G. Carter, M.J. Nobes and J.S. Williams, "The development of cones and associated features on ion bombarded copper", Radiat. Eff. **32** (1977) 129.

[118] J.B. Malherbe, "Sputtering of compound semiconductor surfaces. I. Ion-solid interactions and sputtering yields", Crit. Rev. Solid State Mater. Sci. **19** (1994) 55.

[119] P. Lambelet, A. Sayah, M. Pfeffer, C. Philipona, and F. Marquis-Weible, "Chemically etched fiber tips for near-field optical microscopy: a process for smoother tips", Appl. Opt. **37** (1998) 7289.

[120] B.A.F. Puygranier, P. Dawson, "Chemical etching of optical fibre tips - experiment and model", Ultramicroscopy **85** (2000) 235.

[121] E.W. Weisstein, "Brahmagupta's Formula" and "Tangential Quadrilateral" From MathWorld–A Wolfram Web Resource.

[122] A Simple Sputter Yield Calculator, `https://www.iap.tuwien.ac.at/www/surface/sputteryield` (2019-01-23).

[123] J. Orloff, L. Swanson, and M. Utlaut. High Resolution Focused Ion Beams: FIB and its Applications. Kluwer Academic, 2003.

[124] J.D. Fowlkes, S.J. Randolph, and P.D. Rack, “Growth and simulation of high-aspect ratio nanopillars by primary and secondary electron-induced deposition”, J. Vac. Sci. Technol. B **23** (2005) 2825.

[125] R.W. Nosker, “Scattering of Highly Focused Kilovolt Electron Beams by Solids”, J. Appl. Phys. **40** (1969) 1872.

[126] P. Sigmund, “A mechanism of surface micro-roughening by ion bombardment”, J. Mater. Sci. **8** (1973) 1545.

[127] D.J. Comstock, J.W. Elam, M.J. Pellin, and M.C. Hersam, “High aspect ratio nanoneedle probes with an integrated electrode at the tip apex”, Rev. Scient. Inst. **83** (2012) 113704.

[128] D.J. Burbridge and S.N. Gordeev, “Proximity effects in free-standing EBID structures”, Nanotechnology **20** (2009) 285308.

[129] H. Aouani, J. Wenger, D. Gérard, H. Rigneault, E. Devaux, T.W. Ebbesen, F. Mahdavi, T. Xu, and S. Blair, “Crucial Role of the Adhesion Layer on the Plasmonic Fluorescence Enhancement”, ACS Nano**3** (2009) 2043.

[130] A.M. Angulo, C. Noguez, G.C. Schatz, “Electromagnetic Field Enhancement for Wedge-Shaped Metal Nanostructures”, J. Phys. Chem. Lett. **2** (2011) 1978.

[131] T. Saiki, S. Mononobe, M. Ohtsu, N. Saito, and J. Kusano, “Tailoring a high-transmission fiber probe for photon scanning tunneling microscope”, Appl. Phys. Lett. **68** (1996) 2612.

[132] L. Novotny, D.W. Pohl and B. Hecht “Scanning near-field optical probe with ultrasmall spot size”, Opt. Lett. **20** (1995) 970.

[133] R. Stöckle, C. Fokas, V. Deckert, and R. Zenobi, “High-quality near-field optical probes by tube etching”, Appl. Phys. Lett. **75** (1999) 160.

[134] Z. He, Z. Han, M. Kizer, R.J. Linhardt, X. Wang, A.M. Sinyukov, J. Wang, V. Deckert, A.V. Sokolov, J. Hu, and M.O. Scully, “Tip-Enhanced Raman Imaging of Single-Stranded DNA with Single Base Resolution”, J. Am. Chem. Soc.**141** (2019) 753.

[135] S. Berweger, J.M. Atkin, R.L. Olmon, and M.B. Raschke, “Light on the Tip of a Needle: Plasmonic Nanofocusing for Spectroscopy on the Nanoscale”, J. Phys. Chem. Lett. **3** (2012) 945.

[136] R.X. Bian, R.C. Dunn, X.S. Xie, and P.T. Leung, “Single molecule emission characteristics in near-field microscopy”, Phys. Rev. Lett. **75** (195) 4772.

[137] N. Ocelic and R. Hillenbrand, “Subwavelength-scale tailoring of surface phonon polaritons by focused ion-beam implantation”, Nat. Mat. **3** (2004) 0606.

[138] H. Kollmann, X. Piao, M. Esmann, S.F. Becker, D. Hou, C. Huynh, L.-O. Kautschor, G. Bösker, H. Vieker, A. Beyer, A. Gölzhäuser, N. Park, R. Vogelgesang, M. Silies, and C. Lienau, “Toward Plasmonics with Nanometer Precision: Nonlinear Optics of Helium-Ion Milled Gold Nanoantennas”, Nano Lett. **14** (2014) 4778.

[139] L. Seitl, F. Laible, S. Dickreuter, D.A. Gollmer, D.P. Kern, and M. Fleischer, “Miniaturized fractal optical nanoantennas defined by focused helium ion beam milling”, Nanotechnology **31** (2020) 075301.

[140] L. Zhang, N.F. Heinig, S. Bazargan, M. Abd-Ellah, N. Moghimi, K.T. Leung, “Direct-write three-dimensional nanofabrication of nanopyramids and nanocones on Si by nanotumefaction using a helium ion microscope”, Nanotechnology **26** (2015) 255303.

Acknowledgment

I would like to express my deep gratefulness for Prof. Dieter P.Kern and Prof. Monika Fleischer for grant me the opportunity to carry out the project as a PhD thesis. They have support me generously; to a achieve better results, managing the project, and comprehensive proofread of the thesis. During pursing my studies, I received many help and support, and shared fruitful discussions with friends and colleagues.
I wish to say thank you for;

- Former colleagues and A.G. Fleischer/Kern members for sharing their laboratory time and experience (alphabetically ordered); A. Brauer, A. Horrer, C. Dreser, C. Schäffer, D.A. Gollmer, E. Gürdal, F. Laible, J. Fulmes and S. Dickreuter.
- J. Kemmler, M. Turad and R. Löffler for their support with FIB machine and LISA$^+$ laboratories.
- R. Stiefel, B. Herzog and E. Lohmann for their help with the laboratory instruments.
- D. Auwärter for providing the tapered single mode fibers, and sharing his lab time and experience.
- M. Martina for conducting different experiments to test the probes, and other experiments.
- My family for supporting me along the whole time.
- My cousin H. Al-Abadleh for her generous support and time.
- My friends in Uni. Tübingen and my former colleagues for sharing fruitful discussions and creative solutions, and making the time enjoyable.

.